Micron-scale characterization of laser processed silicon via low temperature micro-photoluminescence spectroscopy

Young-Joon Han

November 2018

A thesis submitted for the degree of

Doctor of Philosophy of

The Australian National University

© Copyright by Young-Joon Han 2018

Declaration

I certify that this thesis does not incorporate, without acknowledgement, any material previously submitted for a degree or diploma in any university, and that to the best of my knowledge, it does not contain any material previously published or written by another person except where due reference is made in the text. The work in this thesis is my own, except for the contributions made by others as described in the Acknowledgements.

Young-Joon Han

Acknowledgements

I might not be able to finish this thesis without so much great support and guidance from many people. I would like to take an opportunity to express my deepest appreciation of all those people have done for me.

Firstly, I would like to express enormous gratitude to my supervisor, Dr. Evan Franklin. His unfailing support and encouragement helped me to overcome many challenges (personal and technical) during my research journey, from honours degree to PhD. I am really grateful for his invaluable advice, guidance, inspiration, and in particular dedicated and meticulous feedback for the writing of papers. I wish the best luck and happiness in his new life in Tasmania.

I would also like to express my deepest thanks to Professor Daniel Macdonald for his advice, generous support and 'adoption'. In particular, his financial support covering the unexpectedly extended my PhD period helped me finalize the writing of this thesis in the last couple of months. I am also indebted to Dr. Hieu Nguyen for sharing his expertise in PL spectra analysis, which is the main topic of this thesis, and for his collaborative work.

I wish to acknowledge all the people helped my experiments. Dr. Marco Ernst has helped me in making numerous laser-samples, and in characterization. His brilliant application programs provided me the convenience and enable to save much time in making laser stage macro and analysing local recombination. I would like to thank Dr. Er-Chien Wang for the diffusion and dielectric deposition for the locally diffused samples, and Dr. Di Yan for the diffusion recipes and the provision of valuable diffused samples and their data. Thanks to Dr. Xinyu Zhang and Dr. Andrew Thomson for their advice about a-Si sputter coating, Dr. Yimao Wan for PECVD a-Si deposition, and Dr. Pheng Phang for helping me ALD Al_2O_3 deposition. Special thanks to Dr. Sachin Surve for his provision of maintenance and other technical aspects of the laser systems. I also want to thank to Dr. Kaushal Vora of ANFF ANU node for sputter coating, and Professor. Hoe Tan of EME ANU for allowing access to μ-PLS system in EME before our lab has a new μ-PLS system.

I am grateful to all the technical and support staffs, Nina de Caritat, Maureen Brauers, Bruce Condon, James Cotsell and Mark Saunders, for maintaining the lab

safe and running. Thank you to all fellows, Dr. Ryan Sun, Dr. Azul Osorio Mayon, Dr. Anyao Liu, Jessica Wu, Rabin Basnet, Ingrid Haedrich, and many others, who have spent many hours together in the office and lab.

Great thanks to my dearest friends, Jin-soo Yoon and In-seok Yang, for many dinners and conversations of sharing PhD study troubles and knowledge of other disciplines. I am really indebted to Chi's family, Chang-kyoung bro, Kerry, Hannah and Jayden, for their heart-warming hospitality and support. You are another my family in Canberra.

It is of course impossible to finish this thesis without my family's unconditional love and support. Dad, I am really proud of you and thank you for everything. Mom, your son has grown up and finalizing one chapter of the life. I am really miss you and wish you were here. Rest in peace. Young-eun, Jimin, Roy and Ria, I really thank you for being with me. Last, but not least, I would like to thank my girlfriend, Do-yeon, for her encouragement, and for embracing and understanding such a man sometimes tempered or in a bad mood during PhD study period.

I acknowledge that this thesis has been copyedited - focusing on grammar, spelling, capitalisation, punctuation, hyphenation (Standard D of Australian standards for editing practice) and overall completeness and consistency (Standard E) - by Dr. Nicola van Dijk of A+ Academic Editing Canberra in accordance with Australian National University Guidelines.

Abstract

Laser processing is now regarded as a promising tool to reduce the cost and complexity of fabricating the formation of localized contacts between heavily doped silicon and metal, features which have become an important element in high efficiency silicon solar cells, such as a passivated emitter and rear cell (PERC) and an interdigitated back contact cell (IBC). However, characterization of localized features with conventional PV characterization tools is challenging, mainly due to the limitations of spatial resolution. This thesis develops and applies novel characterization methods to these localized features using low temperature micro-photoluminescence spectroscopy (μ-PLS). This technique demonstrates that localized features, even single laser pulse processed regions typically tens of micrometres in scale, can be investigated directly without the need for specific sample structures and their electronic properties can be mapped spatially in the sub-micrometre regime.

Utilizing the sub-micron precision of these measurements, the laser-induced crystallographic damages were investigated at various positions within the laser-processed region, particularly at specific points such as the boundary/edge of processed and unprocessed regions. It was found that the edge, or pulse overlapped regions, were significantly more defective than the centre region. The impact of laser parameters, such as laser pulse fluence and number of repeat pulses, on laser-induced damage was also analysed. Significantly different levels of defect-related PL signals were observed after laser processing of the two different substrate surface conditions. This suggests that wafer surface preparation can be an important factor impacting on the quality of laser-processed silicon.

The doping profiles of thermally boron-diffused silicon samples, which have Gaussian function type doping profiles, can be estimated from the measured PL spectra alone. The wavelength of the doping-related PL peak (doping peak) has a reliable and simple linear relationship with the surface dopant density on a semi-log plot. The PL intensity of the doping peak also shows a linear relationship with the doping depth metric (depth factor), but only after considering the reduction of PL intensity due to enhanced incomplete dopant ionization at low temperature. Doping profiles can be easily reconstructed based on these two linear relationships and their

accuracy was verified by comparisons with existing doping profiles (via ECV profiling). Mapping of the surface dopant density and the depth factor of micron-scale locally diffused features was undertaken using 2-D mapping with μ-PLS measurements at 2 μm spatial resolution.

This method was also applied to 532 nm laser-doped silicon to show its effectiveness on locally laser-doped features. The doping profiles of laser-doped silicon were also successfully estimated from PL spectra measurements alone, along with 2-D maps of the surface dopant density and the depth factor of the laser-doped silicon. In addition, the impact of temporal pulse parameters, such as pulse duration and temporal pulse shapes, on the doping profiles and recombination properties of laser-doped silicon were investigated. By correlating defect-related PL band counts with the quantified recombination parameters determined by the luminescence-coupled numerical device simulations, it was shown that μ-PLS measurements are able to perform quantitative measurements of recombination properties.

The last chapter of this thesis demonstrates an application of an advanced laser doping process using a stack of intrinsic amorphous silicon (Si:H(i)) and boron-doped amorphous silicon (a-Si:B). The results showed that this stack is able to provide excellent surface passivation as well as a sufficient amount of dopant source for laser doping.

The method presented in this thesis is a very effective, simple and rapid characterization for analysing localized features, in particular spatially inhomogeneous laser-processed features on the micron-scale. This method enables the observation of the variation in properties within localized features which is not possible using conventional methods. It allows for a more in-depth study of laser processing and promotes further development of laser technologies for high efficiency cell fabrication.

Table of Contents

Declaration i
Acknowledgements iii
Abstract v
Table of Contents vii
List of Figures ix
List of Tables xv
List of Abbreviations xvi
List of Symbols xviii

Chapter 1. Introduction 1

1.1 Background 1
1.2 Localized features of high efficiency solar cells 3
1.3 Thesis aim and scope 6
1.4 Thesis outline 7

Chapter 2. Review of the current characterization methods for doped Si 11

2.1 Overview 11
2.2 Silicon properties in laser processing 12
2.3 Laser doping for silicon solar cells 23
2.4 Limitations of the current characterization techniques 29
2.5 Summary and Implications 42

Chapter 3. Methodology for µ-PLS characterization of localized features 46

3.1 Overview 46
3.2 Working principles of low temperature micro-PLS 46
3.3 Phonon-assisted radiative recombination of intrinsic silicon 47
3.4 Impact of dopant impurities on PL spectra 50
3.5 Impact of crystalographic defects on PL spectra 53
3.6 Characteristics of the PL spectra of heavily doped layers 55
3.7 Micro-PLS system configuration and setup 57
3.8 Laser systems at ANU 59
3.9 Summary and implications 61

Chapter 4. Spatial characterization of laser induced doping/damage in Si with different surface conditions 63

4.1 Introduction 63
4.2 Experimental details 64
4.3 PL spectra of excimer laser-damaged Si 65

4.4 PL spectra of excimer laser-doped Si 69
4.5 Impact of substrate surface conditions on laser doping 75
4.6 Chapter summary 78

Chapter 5. Determination of dopant density profiles of thermally boron-diffused Si 81

5.1 Introduction 81
5.2 Experimental details 81
5.3 Estimating key parameters of doping profiles 84
5.4 Application to locally diffused samples 90
5.5 Chapter summary 97

Chapter 6. Characterization of laser doped Si formed by different temporal pulse profiles 99

6.1 Introduction 99
6.2 Impact of laser temporal parameters on the doping profiles of laser-doped silicon .. 101
6.3 Reconstructing doping profiles of laser-doped silicon 105
6.4 2-D mapping of N_{surf} and z_f for the full area and locally laser doped silicon 111
6.5 Recombination properties of laser doped silicon 114
6.6 Impact of high defect-related PL spectra 122
6.7 Chapter summary 124

Chapter 7. Advanced laser processing using a stack of a-Si:H(i) and a-Si:B 127

7.1 Introduction 127
7.2 Sample preparation 128
7.3 Surface Passivation of the amorphous silicon stack 129
7.4 laser-induced doping and damage through various compositions of the a-Si stack... 131
7.5 Chapter summary 135

Chapter 8. Conclusion 137

8.1 Key findings and contributions 137
8.2 Suggestions for future work 140

List of publications 142

Bibliography 143

List of Figures

Figure 1-1 Schematic of the PERL structure. Note heavy n+/p+ doping and restricted contact area underneath metal contacts. The figure is taken from Ref. [29]. 4

Figure 1-2 Geometry of point contacts IBC cells. All n+ and p+ heavily doped regions form micron-scale point contacts with metal. The figure is take from Ref. [19]........ 5

Figure 2-1 The absorption coefficient α of silicon as a function of wavelength at 79 K and 300 K. The figure has been reproduced from Ref. [59]. 14

Figure 2-2 Simplified schematic of recombination processes in an energy band diagram: a) radiative BB b) SRH and c) Auger recombination. 17

Figure 2-3 (a) The band-gap shrinkage ΔE_g and (b) the band-gap E_g as a function of dopant density and temperature, at the steady-state with the excess carrier $\Delta n/p = 5 \times 10^{18}$ cm^{-3} 20

Figure 2-4 (a) The band-gap shrinkage ΔE_g and (b) the band-gap E_g as a function of dopant density and excess carriers $\Delta n/p$, at T = 79 K 21

Figure 2-5 Ionization ratio as a function of boron density and temperature 23

Figure 2-6 Configuration of four-point probes on a rectangular sample. The figure is taken from Ref. [98]. 30

Figure 2-7 Schematic diagram of the electrochemical cell in an ECV profiler. The figure is taken from Ref. [101] 32

Figure 2-8 Power transmission ratios of different levels of boron concentration. The figure is taken from Ref. [110]. 34

Figure 2-9 Two-dimensional boron concentration map of laser doped samples processed with a Q-Switched DPSS laser with: (a) pulse energy of 15 μJ and pulse distance of 125 nm; (b) pulse energy of 17.5 μJ and pulse distance of 500 nm. (c) A thermally boron-diffused sample is given as the reference. The figure is taken from Ref. [95]. 35

Figure 2-10 3-D domain of a unit cell used in local recombination analysis in Chapter 6. Red is a circular laser-doped p+ region. Blue is a virtual contact for simulation. Green represents the no-conductive boundaries. Width and height of a unit cell is a half of actual pitch size. 40

Figure 2-11 An example of simulated PL intensity for a constant pitch of 60 μm, 120 μm and 180 μm as a function of local recombination parameter $J_{0,d}$. 41

Figure 2-12 A calibration curve established by correlating measured τ_{eff} and PL counts in the reference region (green dot circle) is used to extrapolate the $J_{0,d}$ values of the locally laser-doped sample from the uncalibrated measured PL image. 41

Figure 3-1 Band diagram illustration for the photoluminescence process in silicon. The momentum conserving phonons are associated in the radiative recombination........ 47

Figure 3-2 PL spectra of intrinsic silicon (lightly phosphorus-doped 2×10^{14} cm^{-3}), measured at 26 K. All spectral peaks represent the radiative recombination of e-h pairs with the assistance of the indicated phonons. Detailed information on all peaks is listed in Table 3-1. The figure is taken from Ref. [133]........ 48

Figure 3-3 Temperature dependence of intrinsic silicon PL spectra in the temperature range of 78 K ~ 363 K. Peaks merge into a single broad and low peak as temperature increases. The figure is taken from Ref. [134]........ 49

Figure 3-4 PL spectra of intrinsic silicon measured at liquid-nitrogen temperature (~ 80 K) in linear (blue) and semi-log (red) scales, using a 532 nm DPSS CW laser with an excitation power of 11 mW (~ 130 kW/cm^2). Except for a laser harmonics peak at around 1064 nm, two peaks related to radiative recombination in silicon are observed. 49

Figure 3-5 Schematic illustration of the band structure of (a) lightly-doped and (b) heavily-doped p-type silicon. Simplified band-band luminescence channels are given for each band structure. E_c, E_v, E_A, and E_F are the conduction band, the valence band, the acceptor dopant energy level, and the Fermi level, respectively. 52

Figure 3-6 (Left) Dislocation-related D-lines of PL spectra, measured at 4.2 K from plastically deformed silicon [144]. (Right) Band structure illustration for the recombination of D1~D4 lines, proposed by Suezawa *et al* [131]........ 55

Figure 3-7 Superposition of PL emissions from the heavily doped layer and the intrinsic silicon substrate result in two distinctive peaks, the Si BB radiative and doping peaks. The spectrum from an undoped silicon sample (Intrinsic Si) is given for comparison. The spectrum was measured from a heavily laser-doped silicon sample (LD Si)........ 56

Figure 3-8 Decoupling the PL emissions of the heavily laser-doped layer from the PL spectrum shown in Figure 3-7 by subtracting the PL component of intrinsic silicon........ 57

Figure 3-9 Schematic of the µ-PLS system........ 58

Figure 3-10 (Left) Schematic of the excimer laser system, and (Right) the temporal pulse profile measured at 25 kV discharge........ 59

Figure 3-11 (Left) Schematic of the green laser system, and (Right) the demonstration of arbitrary waveform generation in 1 ns resolution........ 60

Figure 4-1 Microscopic images of laser doped regions (4 J/cm2) on (a) CMP and (b) TMAH-etched substrates, indicating PLS measurement locations; the centre, the edge and the overlapped regions........ 65

Figure 4-2 Normalized PL spectra measured on excimer laser-irradiated samples without a the inclusion of dopants at (a) the centre, (b) the edge, and (c) pulse overlapped regions, on both TMAH-etched and

CMP substrates. Excitation is achieved with a 532 nm laser, and substrate temperature is 79 K. 66

Figure 4-3 Normalized micro-PL spectra measured on excimer laser doped samples with (a, b) 1.5J/cm2 or (c, d) 4J/cm2 at the centre regions on (a, c) TMAH-etched and (b, d) CMP substrates. Excitation is achieved with a 532nm laser, and substrate temperature is 79K. 70

Figure 4-4 The wavelengths of the doping peaks and sheet resistances from laser-doped silicon substrates with (a, c) CMP surface and (b, d) TMAH-etched surface finish, as a function of number of repeat laser pulses and for a range of laser fluences, observed via µ-PLS measured at the centre of the laser-doped regions. 71

Figure 4-5 Normalized PL spectra measured on excimer laser-doped samples with (a, b) the edge and (c, d) the overlapped regions on (a, c) TMAH-etched and (b, d) CMP substrates. Excitation is achieved with a 532nm laser, and substrate temperature is 79K. 74

Figure 4-6 Normalized PL spectra measured on excimer laser-processed (without dopant precursor) samples with 4 J/cm^2 and 3 repeat pulses at (a) the centre, (b) the edge, and (c) pulse overlapped regions, and on both TMAH-etched and CMP substrates. Excitation is achieved with a 532nm laser, and substrate temperature is 79 K. 76

Figure 4-7 Silicon band-band PL peak intensities from (a, b) laser doped and (c, d) laser-processed silicon substrates with CMP surface and TMAH-etched surface finish, as a function of number of repeat laser pulses and for a range of laser fluences, observed via µ-PLS measured at the centre of laser-doped regions. 77

Figure 5-1 Doping profiles measured by ECV for a selection of thermally boron-diffused samples used for µ-PLS analysis, with corresponding measured sheet resistances 82

Figure 5-2 (a) Normalized PL spectra of a selection of boron-diffused samples with different doping profiles, measured with a 532 nm laser at 79 K. (b) Modified PL spectra obtained by subtracting the PL spectra of undiffused Si (c) The corresponding doping profiles with sheet resistances. (d) Measured wavelengths of the doping peaks as a function of N_{surf} for all samples, along with Nguyen and Macdonald's results [143] measured from homogeneously heavily boron-doped silicon. 85

Figure 5-3 The coefficient of determination R^2 of two modelled functions (Gaussian and ERFC) for thermally boron-diffused samples. An R^2 of 1 indicates that the modelled functions perfectly fit the measured points. 87

Figure 5-4 Normalized PL intensity of the doping peak as a function of depth factor, (a) without any correction, and (b) including a correction for the effect of incomplete ionization on PL intensity. Representative samples shown in Figure 5-2 are also labelled accordingly. 89

Figure 5-5 Normalized and subtracted PL spectra of locally diffused samples, labelled as LB1-3 with N_{surf} and z_f , with a 532 nm excitation laser at 79 K. The corresponding profiles are shown in the inset. 92

Figure 5-6 The measured and reconstructed doping profiles, used for locally diffused samples (LB1 – 3), with corresponding sheet resistances. 93

Figure 5-7 2-D scanned maps of N_{surf}, for locally diffused samples through 30, 40 and 50 µm dielectric mask openings. 94

Figure 5-8 2-D scanned maps of z_f, for locally diffused samples through 30, 40 and 50 µm dielectric mask openings. 95

Figure 5-9 (a) Horizontal section of 2-D map of LB3-40µm sample's doping peak PL intensity, measured with different excitation intensity (74, 160, 320 kW/cm^2), and (b) normalized to 1 for the comparison. 97

Figure 6-1. The sheet resistances of the large area of laser doping, processed with (a) different pulse durations (100, 200, 400 and 600 ns) and (b) different temporal pulse profiles (ISO, SQR, INC and DEC) 103

Figure 6-2 (a,c) Temporal pulse profiles and (b,d) corresponding doping profiles measured via ECV profiling when applying (a,b) different shapes (ISO, SQR, INC and DEC), or applying (c,d) different pulse durations from 100 to 600 ns. Measured sheet resistances are provided for the comparison. 104

Figure 6-3 The coefficient of determination R^2 of two modelled functions (Gaussian and ERFC) for 15 laser-doped samples. An R^2 of 1 indicates that the modelled functions perfectly fit the measured points. 106

Figure 6-4 (a) Measured wavelengths of the doping peaks as a function of N_{surf} (b) Normalized PL intensity of the doping peak as a function of z_f without correction (black), and including a correction for the effect of incomplete ionization on the PL intensity (red). 107

Figure 6-5 Measured and reconstructed doping profiles of four distinctive laser-doped samples, with their corresponding sheet resistance. 108

Figure 6-6 Schematic illustration of the surface accumulation of dopants due to the segregation effects for (a) $k_i = 1$ and (b) $k_i < 1$ after laser doping. The figure is taken from Ref. [170]. 109

Figure 6-7 Comparison between the 4pp measured R_{sh} and the µ-PLS estimated R_{sh}. 110

Figure 6-8 2-D scanned maps of N_{surf} and z_f, for the large area laser-doped samples, processed with (a,c) 200 ns ISO waveform and 4 µm beam spacing, with (b,d) 600 ns SQR waveform and 8 µm spacing. 111

Figure 6-9 2-D scanned maps of N_{surf} and z_f, for locally laser-doped samples, processed with (a,c) 100 ns ISO waveform and 6 repeat pulses, with (b,d) 600 ns SQR waveform and 6 repeat pulses. 112

Figure 6-10 Estimated N_{surf}, z_f and R_{sh} as a function of repeat pulse numbers, for locally laser-doped features processed with different pulse durations (a,c,e) and different pulse shapes (b,d,f). Average value (bar graph) and one standard deviation (error bar) across the doped region are

used for this plot. The sheet resistance is calculated using average values of N_{surf} and z_f ... 113

Figure 6-11 Extracted $J_{0,laser}$ image and the arrangement of the large area and locally laser-doped structures with various laser parameters, applying 200 ns ISO waveforms with 3 different pulse energies (9, 11 and 13 μJ) and repeat pulses from 1 to 6. The placement of the inductive coil for PCD measurement is indicated by the dashed circle ... 115

Figure 6-12 Recombination parameter $J_{0,laser}$ as a function of the number of repeat pulses, for locally laser doped samples, processed with (a) different shapes of temporal profiles, and with (b) different pulse durations ... 117

Figure 6-13 2-D scanned maps of wavelengths, normalized PL intensities of the doping peak and the defect band, for locally laser-doped features, processed with the DEC waveform, 24 μJ, 2 or 6 repeat pulses ... 119

Figure 6-14 Normalized defect bands of all locally laser-doped features investigated in this chapter, processed with (a) different pulse shape and (b) different pulse duration. Box plots display the distribution of data measured within the doped region. The central rectangle spans the first quartile to the third quartile, and its mid-line means median. Other symbols are as follows: - : Min/Max, × : 99 %, □ : Mean ... 120

Figure 6-15 The averaged defect band as a function of $J_{0,laer}$, when processed with (a) different pulse shape or (b) different pulse duration. Number of repeat pulses is labelled only for the temporal profiles inducing the lowest $J_{0,laser}$ ... 121

Figure 6-16 Doping profiles of excimer laser-doped silicon samples, processed with 2.5/3.5 J/cm^2 and 1/3 repeat pulses (a) without and (b) with subsequent oxidation process. Corresponding PL spectra are depicted in (c) and (d), respectively ... 123

Figure 7-1 Measured τ_{eff} of a-Si:H(i)/a-Si:B coated samples after a-Si:H(i) deposition only, subsequent to 5 days ageing and doped layer deposition, and subsequent to various low temperature annealing conditions. All τ_{eff} values were extracted at the excess carrier density of 1×10^{15}cm^{-3} ... 130

Figure 7-2 The injection dependent τ_{eff} curve for a 20 nm a-Si:H(i) / 30 vol%B a-Si:B coated sample showing J_0 of 2.5 fA/cm^2, derived from Quokka simulation ... 130

Figure 7-3 Measured sheet resistance as a function of fluence for regions laser doped from a-Si:H(i)/a-Si:B films. The thickness of the a-Si:H(i) layer was varied from 5 nm to 20 nm. On top of the a-Si:H(i) layer, a 50 nm a-Si:B was deposited with 10 vol% or 30 vol% B ... 131

Figure 7-4 Normalized PL spectra on laser-doped samples through (a) 20 nm a-Si:H/ 50 nm 10 vol% B a-Si:B or (b) 20nm a-Si:H/ 50nm 30 vol%B a-Si:B with a fluence range of 1 ~ 4 J/cm^2 at the centre region. Excitation is achieved with a 532 nm laser, and the substrate temperature is 79 K. The spectrum of an unprocessed crystalline Si

and a 20nm a-Si:H/a-Si:B coated silicon sample is plotted for comparison. 133

Figure 7-5 Uncalibrated PL images of laser-doped samples through (a) 20 nm a-Si:H/ 10 vol% B a-Si:B or (b) 20 nm a-Si:H/ 30 vol%B a-Si:B after forming gas annealing at 250˚C for 15 minutes. Different fractions of the laser doped regions are employed, 0.5%, 1.5 % and 5 %. 134

List of Tables

Table 2-1 Optical parameter values of solid state and liquid state silicon, at the wavelengths at which the laser processing and μ-PLS measurements were conducted throughout this study. 14

Table 2-2 Thermal parameters of solid state and liquid state silicon. The solid state refers to parameter values at 300 K. 15

Table 2-3 Values of constants used in Schenk's BGN model [72]............................ 19

Table 2-4 Coefficients for equation (2.14) describing intrinsic silicon band-gap E_{gi} (eV) with temperature in K [69]... 20

Table 2-5 Parameters used to calculate the amount of incomplete ionization for heavily boron doped p-type silicon... 22

Table 2-6 Selection of remarkable achievements in laser-doped c-Si cells............... 24

Table 2-7 Diffusion coefficients of impurities in solid and molten silicon [85]........ 27

Table 2-8 Summary of the current dopant profiling techniques 44

Table 2-9 Summary of the current measurement techniques for recombination properties.. 45

Table 3-1 Threshold energy, associated phonon mode/energy and relative intensities of PL peaks in Figure 3-2 with notations as defined by Dean *et al* [133]; TA – transverse acoustical, TO – transverse optical, Γ – centre of reduced zone-zero wave vector, IV – phonon selected for intervalley scattering of electrons (two phonons, a and b). 48

Table 4-1 A qualitative indication of the presence of the defect-related 1230 nm/1280 nm PL peaks and broad-band defects in PL spectra of CMP and TMAH laser-processed (but undoped) samples for a range of laser fluence and pulse repeats, observed at centre, edge and overlapped laser pulse regions.. 68

Table 5-1 Comparison of ECV measured and μ-PLS estimated values 92

Table 6-1 Values of k_0 and k_i for some dopant elements in silicon [169]............... 110

Table 7-1 The average of PL counts and estimated *Voc* decrease in laser-doped regions shown in Figure 7-5 134

List of Abbreviations

Abbreviation	Description
μ-PLS	Micro-photoluminescence spectroscopy
4pp	Four-point probe
Al-BSF	Aluminium alloyed back surface field
BB	Band-band
BGN	Band-gap narrowing
CMP	Chemical-mechanical polish
CW	Continuous wave
DEC	Declining
DPSS	Diode-pumped solid-state
ECV	Electrochemical capacitance-voltage
ERFC	Complementary error function
FWHM	Full-width at half maximum
FZ	Float zone
IBC	Interdigitated back contact
INC	Inclining
ISO	Isosceles triangular
LBIC	Light beam-induced current
LIT	Lock-in thermography
LPCVD	Low pressure chemical vapour deposition
PCD	Photoconductance decay
PECVD	Plasma enhanced chemical vapour deposition
PERC	Passivated emitter and rear contacts

Abbreviation	**Description**
PERL	Passivated emitter and rear locally doped
PL	Photoluminescence
SEMDCI	Secondary electron microscopy dopant contrast image
SIMS	Secondary ion mass spectroscopy
SOD	Spin-on dopant
SQR	Square
THz-TDS	Terahertz time domain spectroscopy
TMAH	Tetramethylammonium hydroxide

List of Symbols

Symbol	Description	Unit
E_g	Band-gap energy	eV
$I_{corrected}$	The normalized PL intensity of the doping peak and divide it by the fraction of ionization	
J_0	The area weighted sum of recombination within a region	fA/cm^2
$J_{0,laser/pass}$	Recombination parameter for laser-processed/ passivated regions	fA/cm^2
L_H	Material heating depth	µm
L_{th}	Thermal penetration depth	µm
L_α	Optical penetration depth	µm
N_p	Peak dopant density	cm^{-3}
N_{surf}	Surface dopant density	cm^{-3}
R_{sh}	Sheet resistance	µm
z_f	Depth factor	µm
z_p	Position of peak dopant density	µm
λ	Wavelength	nm
$\lambda_{doping\ peak}$	Wavelength of the doping peak	nm
τ_{eff}	Effective lifetime	µs
τ_p	Pulse duration	ns

Chapter 1. Introduction

1.1 BACKGROUND

Since the mid-19th century, fossil fuel has been the major source of energy for civilization. In the late-19th century, great progress in electrical engineering made electricity an essential tool for modern society. The electrification of energy has continued to grow with the world's annual spending on electricity approached parity with spending on oil products in 2016 [1]. About 60 % of worldwide electricity in the same year was generated by the combustion of fossil fuels [2]. Although a large amount of electricity is still generated from fossil fuels, the contribution of renewable energy has grown reaching about 25 % of global electricity production [2]. For the last 10 years (2007 ~ 2017), the annual growth rate of renewable energy, excluding hydroelectric,[1] was about 16 % in contrast to fossil fuels which showed only a 2 % growth rate [3]. There are many influential and interconnected promoters of renewable energy across various fields, including in politics, economics and technology, due to the long-term certainty of renewable energy. Fossil fuels will eventually be depleted and the current growth rate of our heavily energy-dependent society can be only be sustained by utilizing inexhaustible and abundant renewable energy. In addition, not only concerns about global climate change, but also energy security has caused more attention to be paid to renewable energy. It is well known that greenhouse gas emissions cause global warming and that the level of emissions must be reduced to mitigate global climate change. One of the more promising and effective solutions is the decarbonisation of the electricity supply sector from fossil fuel to renewable energy, as electricity generation is the largest single contribution to greenhouse gas emission[4]. After the 1973 oil crisis, many countries felt the need to reduce dependence on any one source of imported energy while also increasing their diversity of energy sources by exploiting renewables [5].

Amongst the various renewable energy technologies, photovoltaics (PV), which directly converts light into electricity using semiconductor devices, experienced the most remarkable growth over recent years. The total global capacity

---

[1] During the same period, hydroelectricity accounted for only 3 % of annual growth.

of PV was only about 14.6 GW in 2008, but increased exponentially over the last decade, reaching about 386 GW in 2017 [6]. Deployment of PV was initially driven by various government policies with significant subsidies because of the uncompetitive cost to conventional energy [7]. However, constantly decreasing PV module prices have enabled PV to now compete with conventional power sources without financial support. The Levelised Cost of Electricity (LCOE) of utility-scale PV fell about 73 % between 2010 and 2017, from USD 0.36 /kWh to USD 0.10 /kWh, within the range of fossil fuel-generated electricity costs [7]. There was even a stunningly low bid of USD 0.0179 /kWh for a 300 MW solar project in Saudi Arabia in 2017 [8].

Although some alternative materials for PV, such as perovskite and cadmium-telluride, have demonstrated a rapid improvement in conversion efficiency in last couple of years [9-12], the current market-dominant technology is a crystalline silicon (c-Si) based solar cell/module, accounting for approximately 94 % of the total PV production in 2016 [13]. Silicon based solar cell technology is a mature technology with over 60 years of development and shows a high conversion efficiency, closer to the theoretical efficiency limit than any other PV technologies [14]. In addition, PV systems based on c-Si cells have shown high reliability and limited efficiency degradation in the field over a long period, therefore they are the most preferred PV technology on the market.

One of main cost reduction drivers for silicon PV is improvements in technology, including increases in performance and better manufacturing efficiency [7, 15]. In terms of performance increase, the improvement in conversion efficiency is obviously critical to reduce the overall cost — a 1 % relative increase in conversion efficiency leads to an almost 1 % reduction in average cost [15]. Enhancements in cell efficiency could be achieved by improving the entire value chain, from material to device fabrication. One of the key requirements is employment of high efficiency solar cell concepts, such as passivated emitter and rear cell (PERC) and interdigitated back contact (IBC) cell structures. As the push to achieve module efficiencies above 20 % has intensified, manufacturers have begun to employ these high efficiency cell structures in mass production [16]. In particular, PERC cells are gaining a significant market share over the currently prevailing aluminium alloyed back surface field (Al-BSF) cells and will become mainstream

after 2020 [17]. The market share of IBC cells is also increasing and is expected to rise from 2 % in 2017 to about 10 % in 2028 [17]. In fact, these concepts were introduced more than 20 years ago [18, 19], but could not be commercialized until 2009 due to the high costs associated with their relatively complex fabrication, compared to the classic Al-BSF cells. The conventional fabrication sequence for these high efficiency cells consists of complex and costly photolithography-based patterning, multiple thermal diffusions and chemical processes, making them unsuitable for mass production. Therefore, many researchers have studied how to reduce the cost and complexity of fabricating these structures. One promising approach is the implementation of laser processing to minimize or even entirely remove complicated patterning steps. In order to deploy the laser processing approach in cell fabrication successfully, there have been many studies of the fabrication of PERC and IBC cells utilizing laser processes [20-24]. However, the deployment of laser processing in the PV manufacturing industry has not progressed satisfactorily due to the lack of adequate characterization methods for the optimization of laser processing.

1.2 LOCALIZED FEATURES OF HIGH EFFICIENCY SOLAR CELLS

A key feature of high efficiency solar cell structures is that they have micron-scale localized contacts to minimize the proportion of highly recombination-active interface between the semiconductor and the metal. The idea of reducing the contact area was firstly proposed by Green in 1975 [25], and applied to the formation of a front emitter in a passivated emitter solar cell (PESC) structure with a 19.1 % cell efficiency record in 1984 [26]. This approach was extended to the rear surface/contact, as illustrated by a PERC structure with an 22.8 % efficiency record in 1989 [27]. By adding localized dopant diffusion in the rear contact areas, a 24 % efficiency cell, named the passivated emitter and rear locally doped (PERL) cell, shown in Figure 1-1, was reported in 1990 [18]. More refinement on the PERL cell structure [28] eventually lead to another efficiency record of 25.0 % [29].

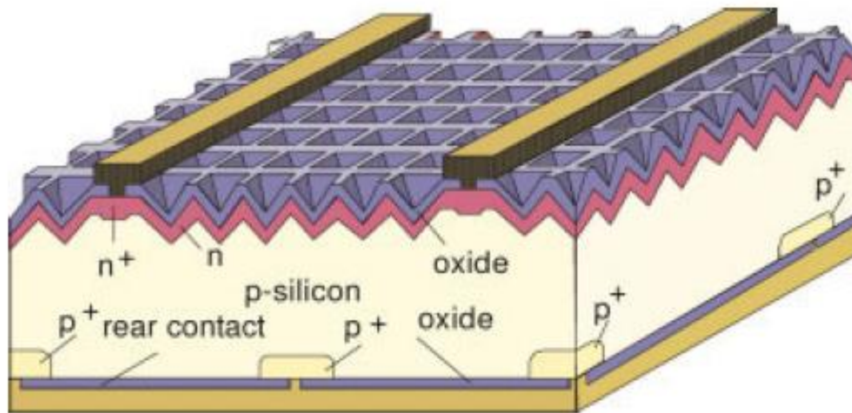

Figure 1-1 Schematic of the PERL structure. Note heavy n+/p+ doping and restricted contact area underneath metal contacts. The figure is taken from Ref. [29].

Another high efficiency cell structure, the IBC cell structure, was first designed by Schwartz and Lammert in 1975 [30]. The design consisted of alternating n- and p-type fingers on the rear surface to reduce internal series resistance and maximise the incident photon flux on the front side. In 1986, the more advanced IBC cell design by Swanson [19] was proposed which restricted the contact coverage to small points, as shown in Figure 1-2. This design already had a conversion efficiency above 20 % in the 1980s but was intended for application in concentrator solar cells [30-32]. Soon after, this design gained attention for its possible application in one-sun solar cells. The IBC design, in conjunction with heterojunction technologies, now surpasses the 25 % efficiency record of the PERL cell. Indeed, the current world-record efficiency of c-Si based solar cells is 26.3 %, based on those two technologies [33]. Heterojunction technology enables a higher open circuit voltage (V_{oc} = 0.73 ~ 0.75 V) compared with that of the homojunction technology (V_{oc} = 0.64 ~ 0.71 V) due to a very thin hydrogenated amorphous silicon (a-Si:H) on the c-Si substrate which provides a high-quality passivation and passivated contact structure. The IBC design, meanwhile, maximizes a short circuit current (J_{sc} = 41 ~ 43 mA/cm^2) [33]. Implementing the IBC design on a homojunction c-Si solar cell is also effective, showing an excellent efficiency rate of 25.2 % [34].

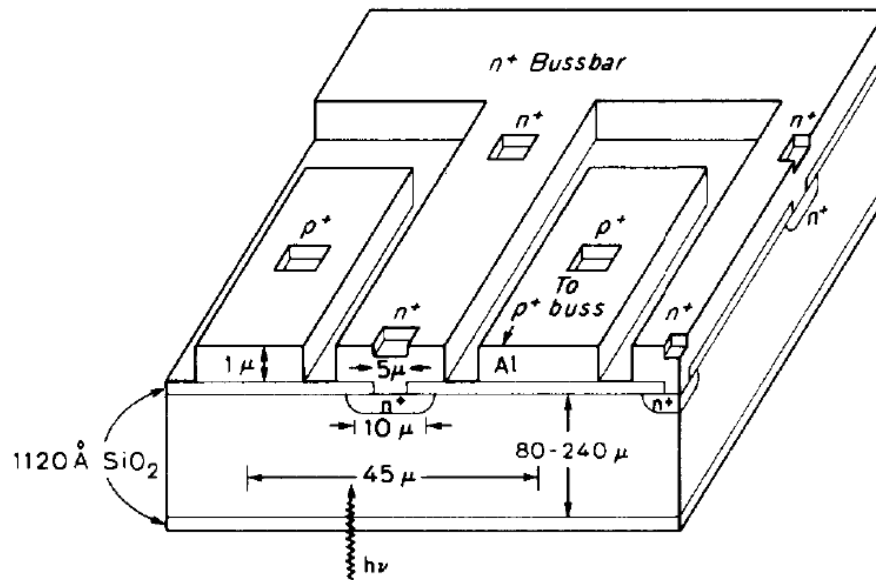

Figure 1-2 Geometry of point contacts IBC cells. All n+ and p+ heavily doped regions form micron-scale point contacts with metal. The figure is take from Ref. [19].

Examining Figure 1-1 and Figure 1-2, we find that both cell structures share two key features. Firstly, there are localized heavily n+/p+ doped regions underneath metal contacts. Secondly, the direct contact between the silicon and metal is restricted through openings of dielectric films which are smaller than the actual size of the doped region. Formation of such localized features is suited to laser processing since laser beams are typically focused onto small areas for high energy density. Thus, laser processing has now been applied to some applications of high efficiency silicon solar cells, for example, the ablation of thin-dielectric films for contact openings [35-37] and the formation of locally doped regions [38-40]. More advanced laser processing, simultaneous ablation and doping from dopant-rich dielectric films, known as PassDop technology, has also been proposed by Suwito *et al* [41]. However, although progressive research in laser processing has been conducted in laboratories, it has not been actively transferred to the PV industry. For example, the shares in laser processing for selective emitter fabrication were only about 5 % in 2017, and are expected to be about 20 % in 2028 [17].

The main reason for the slow diffusion of laser processing in the PV industry is that the conversion efficiency of laser-processed solar cells is still below that of cells made via the traditional method (lithographic mask patterning and thermal diffusion).

The advantage of laser processing in minimizing fabrication steps is outweighed by the conversion efficiency gap, making it not sufficiently attractive to override the traditional method. Although recent improvements in laser processing have reduced the efficiency gap [22, 42], these improvements can be accelerated when accompanied by the development of accurate and efficient characterization methods for localized features.

1.3 THESIS AIM AND SCOPE

In order to evaluate the quality of localized features and their impact on efficiency potential, resistive and recombination power losses; specifically contact resistivity and contact recombination properties in locally p+/n+ doped regions are typically examined [43, 44].

Measurements of recombination properties appear to directly represent the quality of the processed region. They normally indicate the level of damage in the processed region and thus help to judge the impact of the processing technique.

Contact resistivity is strongly dependent on dopant density, which is required to be very high in order to form ohmic contacts for sufficient current flow with small voltage drops across the contact [45]. Such heavily doped surface layers additionally help to prevent minority carriers from reaching recombination active metal contacts. As a result, a deep and heavy doping profile inducing a high electric field from the dopant gradient is typically applied to repel most minority carriers from the surface contact. However, the heavily doped layer is also expected to be a recombination active region owing to more Auger recombination. Thus, measurements of doping profiles are essential to estimate both contact resistivity and the recombination of localized features.

However, standard characterization tools for measuring those properties lack the spatial resolution to directly measure the properties of interest on micron-scale localized features. They require relatively large samples, so it is necessary to scale localized features to large sizes. This does not necessarily maintain and represent the properties of localized features. In particular, large fields formed by typical overlapping micron-size laser beams appear to be different compared to localized features. The overlapped region where more laser intensity is irradiated therefore has

different changes to its surface morphology and properties, compared to a region processed with a single and isolated pulse. Since laser processing induces melting and recrystallization cycles, it typically results in inhomogeneous surface morphology and properties, in particular at the boundary between the melted and unmelted regions. Thus, isolated pulse processed features themselves are not likely to be homogeneous, even if a homogeneous beam is applied.

As a result, there is a need to develop a new characterization method which is able to directly measure the doping profile and recombination properties of localized features without a specific sample structure. For a purpose of investigating impacts of laser processing, the new method should have high enough resolution to allow for spatial characterization of those two properties in a submicron regime. In this thesis, I propose such a novel characterization method using low temperature micro-photoluminescence spectroscopy (μ-PLS). Temperature-controlled μ-PLS has already proven to be a reliable, non-destructive and accurate characterization method. Utilizing the advantages of the high spatial and/or spectral resolution of the μ-PLS technique, many authors in the recent silicon PV literature have demonstrated measurements of various parameters including carrier lifetime [46], dopant density [47, 48], dislocations [49], metal impurities [50] and oxygen precipitates [51] with micro resolution. However, these other authors' methods for estimating dopant density are quite complex [47] or limited to lateral dopant density mapping [48]. In addition, there is no specific method for quantifying recombination properties using spectral information.

This thesis aims to further improve the μ-PLS technique for measurement of the doping profile and recombination properties of localized features in a simpler way. In addition, the proposed μ-PLS technique in this thesis is applied to locally laser-processed features to investigate the impact of laser parameters, which have been rarely studied.

1.4 THESIS OUTLINE

Chapter 2 reviews relevant background knowledge including the properties of silicon relating to laser/silicon interaction and the fundamental mechanism of laser doping. Specific parameter values, which will be considered in later chapters, are

referred to and calculated from the literature. This background is followed by a review of conventional and recently proposed characterization methods for localized features. By highlighting their limitations, the desired capabilities of a new characterization method for localized features are emphasised.

The methodology, upon which this work is based, is introduced in **Chapter 3.** The principle and applications of low temperature μ-PLS are briefly reviewed. The notable characteristics of the PL spectra are described along with how it is utilised in later chapters. In addition, the physical meaning and impact of μ-PLS measurement conditions, which must be considered in analysing the measured PL spectra, are stated in more detail. The laser and μ-PLS systems used in this work are also described in this chapter.

Chapter 4 demonstrates that the μ-PLS measurement is capable of spatial characterization with sub-micron precision by applying it to 248 nm laser processed silicon samples. This chapter focuses on laser-induced crystallographic damages as a function of position within the laser-processed region, in particular at specific positions such as at the boundary/edge of processed and unprocessed regions. The impact of laser parameters, such as laser pulse fluence and number of repeat pulses, on laser-induced damage is analysed by observing the relative level of defect-related PL spectra and absolute luminescence intensity. It is also found that the doping-related PL spectra, owing to the band-gap narrowing (BGN) effect, are related to the sub-surface dopant density/doping level. Furthermore, by comparing the defect-related PL signals observed after laser processing on two different substrate surface conditions, we show that wafer preparation can be an important factor impacting on the quality of laser-processed silicon.

In **Chapter 5**, the relationship between the doping-related luminescence peak (hereafter called the 'doping peak') and the heavily doped silicon layer is fully investigated. This is based on thermally boron-diffused silicon samples having various Gaussian function type doping profiles, in terms of surface dopant density and doping depth metric (depth factor). This chapter demonstrates that the doping profiles of localized features can be estimated from measured PL spectra only. We show that the wavelength of the doping peak has a reliable and simple linear relationship with the measured surface dopant density on a semi-log plot. Consequently, it is possible to establish a calibration curve which can be applied to

estimate the surface dopant density. A second calibration curve for estimating the depth factor is also established after correcting the measured doping peak PL intensity to account for the impact of incomplete dopant ionization at low temperatures on the PL intensity. Using these two calibration curves, surface dopant densities and depth factors are estimated and used to reconstruct doping profiles. To show the effectiveness of this method, the reconstructed profiles are compared to the measured doping profiles via ECV profiling. The two-dimensional (2-D) mappings of the surface dopant density and depth factor of the micron-scale locally diffused features are presented, by performing μ-PLS measurements at 2 μm spatial resolution.

The technique developed in Chapter 5 is applied to 532 nm laser-doped silicon samples to estimate the doping profile of the laser-doped silicon in **Chapter 6**. Using the newly established curves correlating μ-PLS measurements and the ECV curves from large-area laser-doped samples it is possible to estimate the surface dopant density and depth factor, and hence the doping profile, of laser-doped silicon. The impact of temporal pulse parameters, such as pulse duration and temporal profile shape, on doping profile and recombination properties of laser-doped silicon are then investigated. 2-D mappings of the surface dopant density and the depth factor of laser-doped features are also presented, as shown in the previous chapter. This chapter expands on the work of Chapter 4 regarding damage-related PL spectra. By correlating the defect-related luminescence band with the quantified recombination parameter determined by the analytic approach designed by Fell *et al* [52], the potential of the μ-PLS method for quantification of recombination properties is presented.

Chapter 7 demonstrates an application of the advanced laser doping process using multi-purpose films capable of providing both excellent surface passivation and effective local doping, via laser irradiation. A stack of intrinsic amorphous silicon (a-Si:H(i)) and boron-doped amorphous silicon (a-Si:B) is deposited via a combination of plasma-enhanced chemical vapour deposition (PECVD) and co-sputtering of silicon and boron. Irradiation using a 248 nm laser simultaneously removes the film and forms the sub-surface doped region beneath the film. Using the μ-PLS method, the evidence regarding doping and amorphous silicon layers is once again confirmed, and the recombination properties are characterized qualitatively.

Finally, **Chapter 8** summarises the key findings of this thesis and identifies the further work that could improve the μ-PLS method and its applications for laser doping characterization.

Chapter 2. Review of the current characterization methods for doped Si

2.1 OVERVIEW

Laser processing methods have already established niche roles for themselves s in the PV manufacturing industry, while showing potential for significantly more widespread use in the future.

Two simple laser techniques used in the c-Si solar cell industry are ‘cutting’ and ‘edge’ isolation [53]. These techniques use very high intensities, above the threshold required to evaporate materials, as non-contact and accurate cutting/scribing methods. Laser cutting is used for the resizing of wafers or the singulation of cells for concentrator cells in relatively low volumes. Recently, laser cutting has been applied in industrial production to cut solar cells in half to reduce cell-to-module losses during assembly [54].

The production of classic Al-BSF cells involves p-type silicon wafers which are diffused over the entire surface, including the rear and edge, with n-type phosphorous. The wrapping n-type emitter layer acts as a shunt pathway to the rear contact and therefore must be isolated: so-called ‘edge isolation.’ Common ways to achieve this include wet chemical [55] or plasma etches [56]. Another approach uses a laser to scribe a continuous groove around the edge of the wafer. The groove extends below the n-type doped shallow layer into the underlying p-type substrate to cut the shunt pathways [53]. A different application of the laser groove can be found in the laser grooved-buried contact (LGBC) cell structure [57]. Deep and narrow grooves are formed into the front emitter surface without exceeding the emitter depth and filled with metal to form the front contacts. This feature, a large and buried cross-sectional area of metal, has the advantage of lower shading and resistive losses, but also induces more recombination due to a large contact area between the silicon and metal. To minimize this detrimental effect, heavy diffusion is applied selectively in the groove. BP Solar commercialized LGBC cells in 2006 [58], but they are now no longer available in mass production.

The most advanced laser technique in PV is laser-induced dopant diffusion (laser doping). This technique received increased attention after localized heavy doping underneath metal contacts became a necessary requirement for high efficiency solar cells. With the advantage of micron-scale selective energy control and deposition, laser doping facilitates self-aligned heavy doping without subjecting the wafer to prolonged high temperature processes and likely corresponding degradation. Unlike laser cutting and scribing, which are simple contactless destructive processes, laser doping changes the electronic properties of the processed region by incorporating dopants into the substrate in the liquid phase by keeping intensities below the evaporation threshold. Depending on combinations of various laser parameters, such as wavelength, pulse duration, number of repeat pulses and beam fluence etc., laser doping can control doping level and depth easily. Furthermore, it is also desirable for laser doping to introduce minimum recombination centres while meeting the required doping level and depth. However, the characterization of locally laser-processed silicon is challenging using conventional characterization methods, so it is necessary to develop a novel method, one which is specifically suited to localized features.

This chapter firstly reviews the optical, thermal and selected electronic properties of silicon relevant to this thesis. Since most parameters are temperature dependent, the parameter values at processing and measurement temperatures are additionally calculated with comparison to the reference values at room temperature. This is followed by the description of the interaction between laser and silicon in terms of laser doping. At the end of this chapter, conventional characterization methods, commonly used in PV research and in this thesis as well, are described with emphasis on their limitations when applied to characterization of localized features. Recently developed techniques by other researchers are also reviewed.

2.2 SILICON PROPERTIES IN LASER PROCESSING

The properties of silicon have been studied extensively for decades, so virtually all its characteristics have been extensively analysed. In this section, only the properties of silicon relevant for laser processing and this work will be reviewed.

2.2.1 Optical properties

This work is heavily reliant on laser/silicon interaction, in both sample processing and characterization. Therefore, it is important to understand the optical properties of silicon. This section reviews silicon's optical behaviour, not only at room temperature, but also above its melting temperature (T > 1690 K) for point laser processing and liquid nitrogen temperature (T = 80 K) at which μ-PLS measurements are performed.

When incident light I_0 is irradiated on a silicon surface, it is firstly reflected by the value of reflectivity R_{Si} at the surface. The transmitted light is then absorbed as travelling in silicon, and the intensity of the light at a certain depth z is described as equation (2.1):

$$I(z) = (1 - R_{Si})I_0\exp(-\alpha z) \tag{2.1}$$

The degree of absorption is determined from the absorption coefficient α. The absorption coefficient is not constant but strongly depends on the wavelength λ and the extinction coefficient k as defined in equation (2.2).

$$\alpha = \frac{4\pi k}{\lambda} \tag{2.2}$$

Figure 2-1 plots the absorption coefficient of silicon in a wavelength range between 200 nm and 1400 nm. The figure is reproduced using Green's tabulated data with temperature coefficients [59] to compare α at 300 K and 79 K. The strong wavelength dependence of α is readily observable and its dependence on temperature is also clearly shown. For photon energies $h\upsilon$ > 3.4 eV (λ = 365 nm), the absorption coefficient saturates approximately 10^6 cm^{-1} regardless of temperature. Above this photon wavelength, it decreases with increasing wavelength, and shows a further reduction at a lower temperature. By taking the reciprocal of α, the optical penetration depth L_α, at which the intensity of light decays to *1/e* of its surface value, can be calculated.

Table 2-1 summarizes the calculated/referred values of optical parameters at 248 and 532 nm, at the wavelength at which laser processing and μ-PLS excitation were conducted throughout this study, from Ref. [59-61]. It is notable that the optical parameters of silicon are no longer dependent on wavelength when it is melted.

The absorbed photons generate electron/hole pairs when the incoming photons have energies $h\upsilon$ equal or greater than the band-gap energy E_g of the material. For silicon, the photon energy required for optical generation should be at least greater than the band-gap energy of silicon $E_g = 1.12$ eV, corresponding to less than $\lambda = 1107$ nm. Since silicon is an indirect band-gap semiconductor, it additionally needs to absorb or emit a phonon in order to adjust different values of crystal momentum for the transition between the conduction band and the valence band. This feature was observed in the spectrally resolved luminescence measurement (see 3.3).

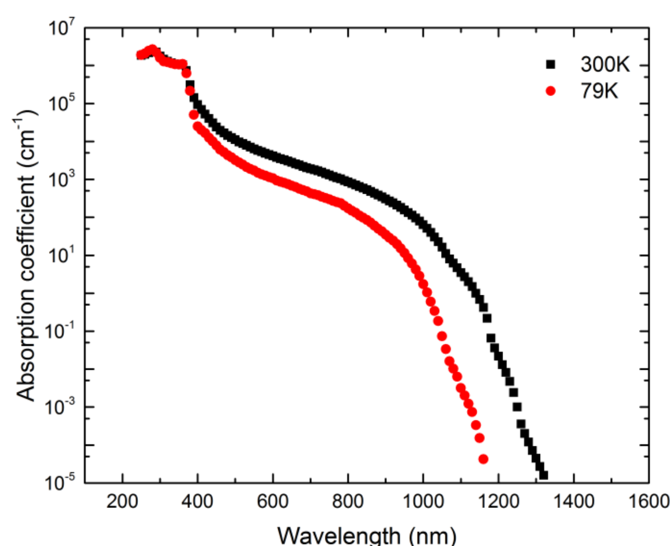

Figure 2-1 The absorption coefficient α of silicon as a function of wavelength at 79 K and 300 K. The figure has been reproduced from Ref. [59].

Parameters	Solid state (79 K)	Solid state (300 K)	Liquid state
R_{Si} (248 nm)	0.71	0.67	0.7
R_{Si} (532 nm)	0.35	0.37	0.71
α [cm^{-1}] (248 nm)	1.9×10^6	1.8×10^6	1.5×10^6
α [cm^{-1}] (532 nm)	2094	7850	1.2×10^6
L_α [nm] (248 nm)	5.2	5.4	6.6
L_α [nm] (532 nm)	4.7×10^3	1.3×10^3	8.5

Table 2-1 Optical parameter values of solid state and liquid state silicon, at the wavelengths at which the laser processing and μ-PLS measurements were conducted throughout this study.

2.2.2 Thermal properties

Parameters relevant to the thermal behaviour during laser processing are: the thermal conductivity $\kappa(T)$, specific heat $c(T)$, density ρ and thermal diffusivity $D_{th}(T)$. The typical parameter values for solid state and liquid state silicon are listed in Table 2-2 [62, 63]. The thermal parameters are also not constant and are strongly dependent on temperature and phase. The phase transitions of silicon occur at the melting temperature T_m = 1687 K and the evaporation temperature T_b = 3538 K.

Parameter	Solid state (300K) [62]	Liquid state [63]	Comment
$\kappa(T)$ [$Wcm^{-1}K^{-1}$)]	1.42	0.56	1.42 at 300 K to 0.287 at 1400 K
$c(T)$[$Jg^{-1}K^{-1}$]	0.71	0.97	0.67 at 273 K to 0.98 at 1373 K
ρ[g cm^{-3}]	2.33	2.53	
$D_{th}(T)$[cm^2s^{-1}]	0.85	0.23	$D_{th}(T) = \kappa(T)/\rho c(T)$

Table 2-2 Thermal parameters of solid state and liquid state silicon. The solid state refers to parameter values at 300 K.

Based on the heat equation for simple, one-dimensional (1-D), time-dependent conduction, the thermal penetration depth L_{th} during laser processing can be approximated with the pulse duration τ_p and the thermal diffusivity D_{th}, as defined in equation (2.3).

$$L_{th} \approx \sqrt{D_{th}(T)\tau_p} \tag{2.3}$$

For the nanosecond pulsed laser systems (τ_p = 1 ~ 1000 ns), the corresponding L_{th} is about 0.3 µm ~ 9.2 µm, and does not exceed 10 µm.

2.2.3 Electronic properties

The µ-PLS measurement is based on the radiative recombination processes of optically generated free charge carriers to characterize the electronic properties of the semiconductor. In this section, a brief description of radiative recombination

processes, in addition of other recombination processes, is given to help understand the μ-PLS measurement. The important characteristics of heavily doped silicon which has a considerable impact on the analysis of the PL spectra of heavily doped silicon are described.

Recombination properties

An excited electron moves from the valence band to the conduction band, leaving a hole behind – an electron-hole pair is created. They are then recombined in the opposite process; the excited electron at the conduction band falls back into the hole in the valence band. The recombination process can be categorized into three different recombination mechanisms: (a) radiative band-band, (b) defect level assisted, the so-called Shockley-Read-Hall (SRH), and (c) Auger recombination, as depicted in Figure 2-2.

Radiative band-band (BB) recombination is the direct inverse of optical generation. The photon emitted by the radiative BB recombination has energy close to the band-gap energy E_g of the material. The rate of radiative recombination is proportional to the product of the electron and hole concentrations. Considering the dopant density $N_{A/D}$ and the excess carrier density Δn due to the carrier injection in silicon, the corresponding radiative BB recombination rate is given as

$$U_{rad} = B(T)(N_{A/D} + \Delta n)\Delta n \tag{2.4}$$

where $B(T)$ is the temperature dependent radiative recombination coefficient of silicon. The most recently determined values of $B(T)$ can be found in Ref. [64].

Defect level assisted recombination is a two-step recombination process where a free electron relaxes to the defect level and then falls to the valence band, to complete the recombination with a hole. During the energy transition from the conduction to the valence band, the excess energy is released as either multiple phonons or photons. Defect levels are associated with the presence of impurities or crystallographic defects in the material, and typically lie deep within the inter-band. The rate of this recombination is obviously dependant on the carrier density and energy level of defects.

Auger recombination is also a band-band recombination, but involves three carriers without the emission of photons. An electron recombining with a hole gives

the excess energy to either an electron ('*eeh*' process) or a hole ('*ehh*' process). It then settles down to a lower energy state close to the band edge by emitting energy in the form of phonons. Traditionally, the Auger recombination rate is expressed as a sum of both *eeh* and *ehh* recombination, as given in equation (2.5).

$$U_{Aug} = C_n n^2 p + C_p n p^2 \tag{2.5}$$

where C_n and C_p are the respective Auger coefficients. The most cited values of the Auger coefficients are $C_n = 2.8 \times 10^{-31}$ cm^{6}s^{-1} and $C_p = 9.9 \times 10^{-32}$ cm^{6}s^{-1} [65]. Based on traditional Auger theory with Coulomb interactions, Richter *et al* [66] developed a more accurate and generalized model for the quantitative description of the Auger recombination rate. Since the Auger recombination process incurs energy exchange among multiple carriers, the probability of this process increases with a higher concentration of charge carriers. Therefore, Auger recombination becomes a dominant process in heavily-doped or highly injected silicon.

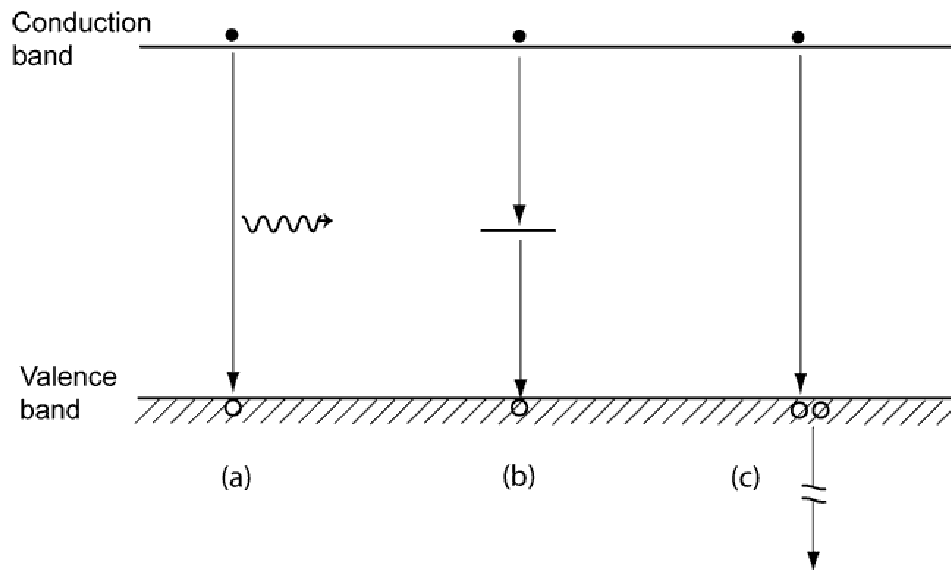

Figure 2-2 Simplified schematic of recombination processes in an energy band diagram: a) radiative BB b) SRH and c) Auger recombination.

Band-gap narrowing

Heavy doping and/or large carrier concentrations due to optical excitation or electrical injection result in a shrinkage of the band-gap in a semiconductor. This phenomenon is called band-gap narrowing (BGN). The consequence of BGN is an

increase in the equilibrium minority carrier density by orders of magnitude, resulting in a strong impact on the operation of the semiconductor device. Therefore, many researchers have searched for an accurate parameterization of BGN. There are currently three models which are able to quantify the shrinkage of the band-gap ΔE_g. The first one is the 'apparent BGN' model devised by del Alamo *et al.* in 1985 [67, 68]. Unfortunately, this model does not perfectly account for degeneracy effects for dopant densities above the effective density of states (N_c = 2.86 × 10^{19} cm^{-3} for electrons and N_v = 3.1 × 10^{19} cm^{-3} for holes at 300 K [69]), since Boltzmann statistics were used instead of Fermi-Dirac statistics. This model was then improved by Yan and Cuevas [70, 71], and considered the degeneracy effect by incorporating Fermi-Dirac statistics. However, both models were experimentally derived at 300 K as a function of the dopant density only, and therefore could not reflect the impact of other external conditions, such as excess carrier densities from optical/electrical generation and temperature. The last model, derived by Schenk [72], is a theoretical model based on quantum mechanics and is able to reflect all conditions.

Schenk's model describes the impact of the free carrier densities and the dopant densities on the BGN separately, as given by,

$$\Delta E_c = \Delta E_c^{xc} + \Delta E_c^{i} \tag{2.6}$$

$$\Delta E_v = \Delta E_v^{xc} + \Delta E_v^{i} \tag{2.7}$$

where ΔE_c^{xc} and ΔE_v^{xc} are the rigid quasi-particle shifts of the conduction and valence band edges due to the free carrier densities, and ΔE_c^{i} and ΔE_v^{i} are the ionic quasi-particle shifts of the band edges due to the dopant densities.

The rigid quasi-particle shifts are given by

$$\Delta E_c^{xc} = -Ry_{ex}\Delta_e^{xc} \tag{2.8}$$

$$\Delta E_v^{xc} = -Ry_{ex}\Delta_h^{xc} \tag{2.9}$$

where

$$\Delta_a^{xc} = -\frac{(4\pi)^3 n_\Sigma^2\left[\left(\frac{48n_a}{\pi g_a}\right)^{\frac{1}{3}} + c_a \ln\left(1 + d_a n_p^{P_a}\right)\right] + \left(\frac{8\pi\alpha_a}{g_a}\right) n_a\zeta^2 + \sqrt{8\pi n_\Sigma}\zeta^{5/2}}{(4\pi)^3 n_\Sigma^2 + \zeta^3 + b_a\sqrt{n_\Sigma}\zeta^2 + 40n_\Sigma^{3/2}\zeta} \quad (2.10)$$

The ionic quasi-particle shifts are given by

$$\Delta E_c^i = -Ry_{ex}\Delta_e^i \quad (2.11)$$

$$\Delta E_v^i = -Ry_{ex}\Delta_h^i \quad (2.12)$$

where

$$\Delta_a^i = -\frac{n_{ionic}(1 + U^i)}{\sqrt{\frac{\zeta n_\Sigma}{2\pi}}\left[1 + h_a \ln(1 + \frac{\sqrt{n_\Sigma}}{\zeta})\right] + j_a U^i n_p^{3/4}\left(1 + k_a n_p^{q_a}\right)} \quad (2.13)$$

In equations (2.10) and (2.13), the subscript a represents either the hole h or electron e and it should be noted that: 1) n_e and n_h are dimensionless electron and hole densities by $n_e \equiv na_{ex}^3$ and $n_h \equiv pa_{ex}^3$, 2) p_e and p_h are constants of Padè approximation, not hole densities. The other parameters are given by $n_\Sigma \equiv n_e + n_h$, $n_p \equiv \alpha_e n_e + \alpha_h n_h$, $\zeta \equiv (kT/q)/Ry_{ex}$, $U^i = n_\Sigma^2/\zeta^3$, $n_{\text{ionic}} = N_\Sigma + a_{ex}^3$, and $N_\Sigma = N_D + N_A$. Values of constants used in the above equations are listed in Table 2-3.

g_e	g_h	α_e	α_h	Ry_{ex}		a_{ex}	
12	4	0.5187	0.4813	16.55meV		37.19×10^{-8} cm	
b_e	b_h	c_e	c_h	d_e	d_h	P_e	P_h
8	1	1.3346	1.2365	0.893	1.153	7/30	7/30
h_e	h_h	j_e	j_h	k_e	k_h	q_e	q_h
3.91	4.20	2.8585	2.9307	0.012	0.19	3/4	1/4

Table 2-3 Values of constants used in Schenk's BGN model [72].

Intrinsic band-gap E_{gi} is also temperature dependent and so determined using equation (2.14) and Table 2-4 [69].

$$E_{gi}(T) = A + BT + CT^2 \tag{2.14}$$

T (K)	A	B	C
0 ~ 190	1.17	1.059×10^{-5}	-6.05×10^{-7}
150 ~ 300	1.1785	-9.025×10^{-5}	-3.05×10^{-7}
250 ~ 500	1.206	-2.73×10^{-4}	0

Table 2-4 Coefficients for equation (2.14) describing intrinsic silicon band-gap E_{gi} (eV) with temperature in K [69].

Using Schenk's model, the band-gap shrinkage $\Delta E_g = \Delta E_c + \Delta E_v$ and the corresponding reduced band-gap $E_g = E_{gi} - \Delta E_g$ are calculated according to various numbers of excess carriers and temperature, as depicted in Figure 2-3 and Figure 2-4. It is obvious that dopant density is the most critical parameter in determining the band-gap E_g. The impact of temperature and the excess carrier densities are also not negligible, so those should be considered accordingly. Although it is observed that the excess carriers have more impact on the band-gap shrinkage ΔE_g than the temperature (Figure 2-3 (a) and Figure 2-4 (a)), the resultant band-gap E_g depicted in Figure 2-3 (b) and Figure 2-4 (b) shows that the temperature variation induces a bigger change of E_g than the number of excess carriers. This is attributed to the large change in the intrinsic band-gap E_{gi} with temperature.

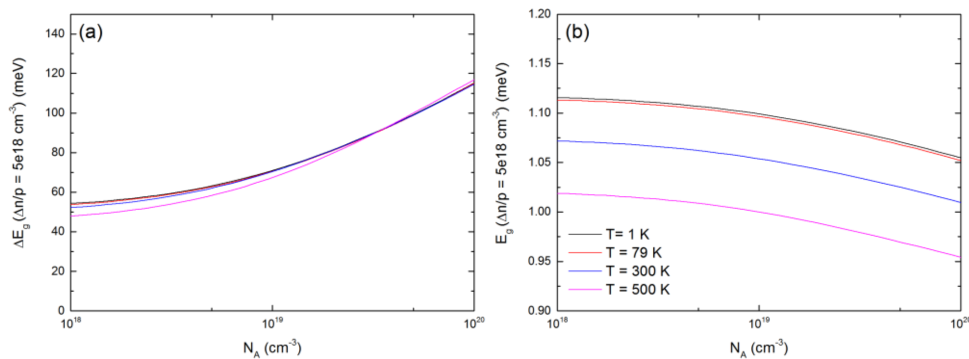

Figure 2-3 (a) The band-gap shrinkage ΔE_g and (b) the band-gap E_g as a function of dopant density and temperature, at the steady-state with the excess carrier $\Delta n/p = 5 \times 10^{18}$ cm^{-3}

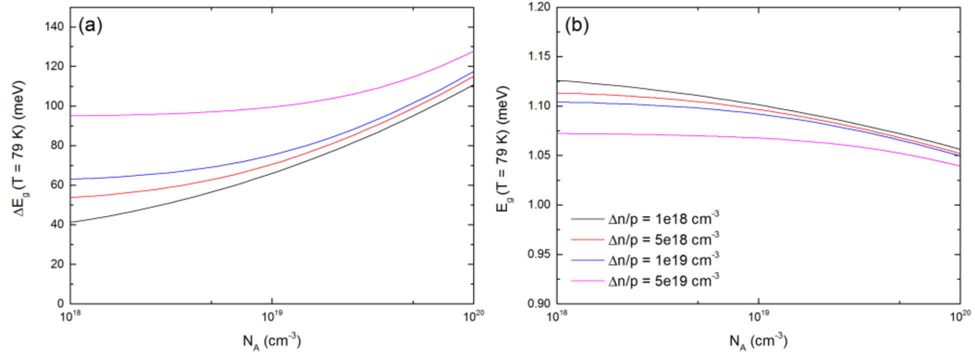

Figure 2-4 (a) The band-gap shrinkage ΔE_g and (b) the band-gap E_g as a function of dopant density and excess carriers $\Delta n/p$, at T = 79 K

Incomplete dopant ionization

Another characteristic of heavily doped silicon is incomplete dopant ionization. Heavily doped silicon has a Fermi level E_F close to the dopant energy state. Free carriers then have a higher probability of being captured at the dopant state and some dopant atoms remain neutral, so-called incomplete dopant ionization. As a result, the net free carrier density is noticeably smaller than the dopant density, even if all dopant atoms substitute silicon atoms in the lattice and are 'electronically active,' providing additional charge carriers. In addition, incomplete ionization is more pronounced at lower temperatures because even thermal energy is not high enough to activate dopant atoms. Altermatt *at al* [73, 74] have derived an accurate model for incomplete dopant ionization in c-Si in the temperature range from 30 to 300 K.

The degree of ionization for the acceptor is given by

$$\frac{N_A^-}{N_A} = \frac{1}{1 + g_A\, p/p_1} \tag{2.15}$$

where

$$g_A(T, N_A) = \frac{b}{g + (1-b)\, N_A/p_1} \tag{2.16}$$

with

$$p_1 = N_v \exp(\frac{-E_{dop}}{kT}) \tag{2.17}$$

$$b = \frac{1}{1 + (N_A/N_b)^d} \tag{2.18}$$

The dopant energy level E_{dop} varies with the dopant density and is expressed as

$$E_{dop} = \frac{E_{dop,0}}{1 + (N_{dop}/N_{ref})^c} \tag{2.19}$$

The effective density of states in the valence bands N_v depend on temperature [69], given as

$$N_v = 2.540933 \times 10^{19} (m_{dv}^*/m_0)^{3/2} (T/300)^{3/2} \tag{2.20}$$

where m_{dv}^* and m_0 are the density-of-states effective masses in the valence band and the electron rest mass, respectively, and the ratio of m_{dv}^* and m_0 is calculated from Ref. [75].

Using the above equations with constant values as listed in Table 2-5, the amount of incomplete ionization for heavily boron doped p-type silicon is calculated.

E_{dop}(meV)	N_{ref}(cm^{-3})	c	N_b(cm^{-3})	d	g
44.39	1.7×10^{18}	1.4	6×10^{18}	2.4	1/4

Table 2-5 Parameters used to calculate the amount of incomplete ionization for heavily boron doped p-type silicon.

Figure 2-5 plots the ratio of ionized boron atoms in boron-doped p-type silicon as a function of the dopant density and temperature. The dopant density in the range between 10^{16} and 10^{19} cm^{-3} is very susceptible to incomplete ionization and it becomes more significant as temperature decreases. However, almost complete ionization is observed for very heavily doped silicon, where the dopant densities are far above the Mott transition ($N_A > 2 \times 10^{19}$ cm^{-3}), regardless of temperature, since the dopant state approaches the band edge [73].

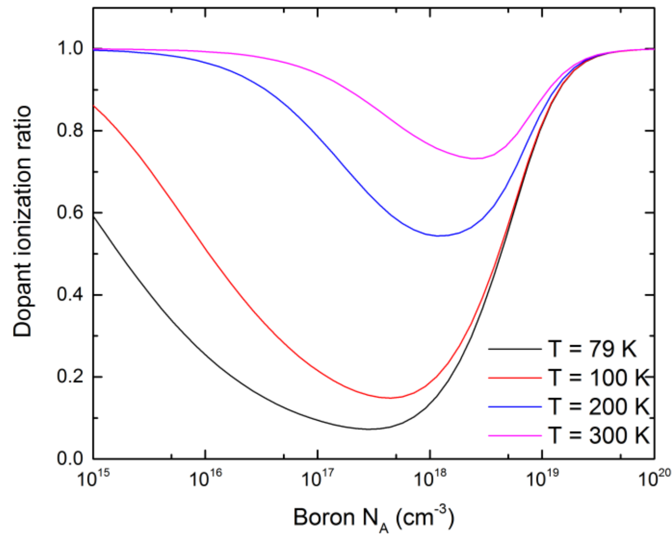

Figure 2-5 Ionization ratio as a function of boron density and temperature

In this work, since all μ-PLS measurements were conducted at liquid-nitrogen temperature (~ 80 K), at which incomplete dopant ionization is much more enhanced, the theory of incomplete ionization is considered in the analysis of the measured PL intensity of heavily doped silicon ($N_A = 10^{18} \sim 10^{19}$ cm^{-3}).

2.3 LASER DOPING FOR SILICON SOLAR CELLS

In this section, the history of laser doping in c-Si PV application is briefly described highlighting the major breakthroughs in laser-doped c-Si solar cell efficiency. The fundamental working principle of laser doping is then discussed.

2.3.1 The development of laser-doped silicon solar cells

The first laser doping was demonstrated by Fairfield and Schwuttke [76] in 1968. They made silicon diodes by irradiating a pulsed laser (λ = 694.3 nm) onto a polished silicon surface on which phosphorus was applied. The first application of this technique in c-Si PV was reported in the early 1980s [77, 78]. The conversion efficiency of the early laser-doped cell was about η = 13 ~ 14 %, slightly (1 ~ 2 %) lower than that of a cell fabricated via conventional furnace diffusion. Subsequently, there was little development in laser doping for PV application until the beginning of the 21st century, at which time there was considerable growth in the solar industry due to intense research being undertaken to find cost-effective production processes.

More recent achievements in laser doping for high efficiency c-Si solar cells are summarized in Table 2-6.

Year	Cell structure	Laser system	Eff. (%)	Ref
2009	Full area laser-doped emitter	λ= 532 nm, τ_p = 65 ns	18.9	[79]
2011	LDSE + Al-BSF	λ= 532 nm, τ_p = 2 µs	19.3	[40]
2016	PERL	λ= 1030 nm, τ_p = 1.3 µs	23.5	[42]
2017	IBC	λ= 532 nm, τ_p = 50 ns	23.2	[22]

Table 2-6 Selection of remarkable achievements in laser-doped c-Si cells

Eisele *et al* [79] demonstrated the potential of laser doping for high efficiency c-Si solar cells, raising the possibility that they may even replace the furnace diffusion process. The full area emitter was made by irradiating a 532 nm laser on the pure phosphorus precursor layer-deposited p-type float zone (FZ) silicon wafers. Because of the non-textured front side, relatively low efficiency η = 18.9 % was achieved, however, the high open circuit voltage V_{OC} = 677 mV verified that laser doping is comparable to furnace diffusion. The classic Al-BSF cell with the laser-doped selective emitter (LDSE) showed efficiency η = 19.3 % in 2011 [40]. Notably, this result was achieved using commercial grade large-area (156.9 cm^2) p-type CZ silicon wafers with standard production equipment. To date, the record efficiency for a laser-doped PERL cell is η = 23.5 % [42]. PassDop technology, a multi-purpose film providing both a dopant source for laser doping and good passivation, was applied in this cell for the formation of the rear local BSF. The most efficient laser-doped IBC cell η = 23.2 % was reported by Dahlinger *et al* [22]. Impressively, all emitter and BSFs were made via laser doping only and all lithographic steps for the contact formation were replaced by laser ablation.

2.3.2 Thermal interaction between lasers and silicon

After the development of high-powered lasers, application of these lasers in semiconductor processing was first suggested in the late 1960s. In the 1970s, ion implantation became the major method for doping silicon in the industrial

manufacture of semiconductors. At the same time, laser annealing was introduced as an alternative to high temperature thermal annealing in order to anneal damages induced by ionic bombardment in the ion implantation process. This led to increased research interest in understanding laser-semiconductor interaction from the late 1970s to the 1980s. Remarkable publications during this period established theoretical models to explain the fundamental phenomenon of the laser process in semiconductors, with experimental evidence. Wood and Giles [80] described the basic models based on macroscopic diffusion equations for heat and mass transport, taking into consideration the temperature and spatial dependencies of various parameters. Their model calculations clearly demonstrated the effect of various laser parameters (including pulse duration, temporal shape and energy density etc.), in terms of the temporal melting depth and temperature profile in silicon. Meyer *et al* [81] provided more general solutions which described the temperature increase of the laser-irradiated semiconductors. Their solutions are not restricted to silicon but is also applicable to a broad range of semiconductors and excitation conditions [82, 83].

The laser-semiconductor interaction is essentially the energy conversion of incoming optical energy to thermal energy in the semiconductor. Detailed descriptions of the various physical processes involved in this energy conversion include:

- The absorbed optical energy creates electron-hole pairs and provides the energy to existing and created charge carriers.
- The excited carriers emit phonons to be at quasi-equilibrium state (thermalization of ‘hot’ carriers). The emitted phonons contribute to the lattice heat.
- The excess carriers diffuse and recombine, and the recombination energy is transferred to the lattice.
- Once the absorbed energy is converted to lattice heat, it is free to diffuse to deeper depths via thermal conduction.

Considering above physical processes of heat delivery, the material heating depth L_H is given by

$$L_H = \frac{1-R(T_0)}{c(T_0)\Delta T}\int_{T_0}^{T_f}\frac{c}{\alpha(1-R)}[\frac{\chi_T}{L_{th}\alpha+1}+\frac{\chi_B^{NR}}{L_{th}\alpha+L_D\alpha+1}+\frac{\chi_S^{NR}}{L_{th}\alpha}]^{-1}dT \qquad (2.21)$$

where $\alpha = \alpha_1 + \alpha_2 + \alpha_{FC}$ is the total optical absorption coefficient, α_1 and α_2 are the one- and two-photon absorption coefficients, α_{FC} is the free-carrier absorption and L_D is the carrier diffusion length. χ_T, χ_B^{NR}, and χ_S^{NR} are the fractions of the absorbed optical energy which go into the thermalization of 'hot' carriers immediately after excitation, non-radiative bulk recombination, and non-radiative surface recombination respectively.

For the total optical absorption coefficient, α_1 is the intrinsic absorption coefficient as described in 2.2.1. The second efficient, α_2, is negligible since the photon energy of the lasers used in this work (λ = 248 or 532 nm) is much greater than the silicon band-gap E_g = 1.12 eV (λ = 1107 nm), and α_1 is much stronger than α_2 [82]. The last coefficient α_{FC} has a significant impact only for infrared light (λ > 1100 nm) and heavily doped layers [84], so it could be ignored in this study. The three terms $\chi_T, \chi_B^{NR}\chi_S^{NR}$ within the bracket are strongly dependent on experimental conditions. When the photon energy is well above the silicon band-gap E_g, the first term χ_T usually dominates, since most of the laser energy is then immediately transferred to the lattice due to the thermalization of 'hot' carriers, so the other two terms in the bracket could be ignored [81]. Therefore, equation (2.21) could be simplified considerably as is shown in equation (2.22).

$$L_H \approx \frac{1}{\alpha_1} + L_{th} \approx L_a + \sqrt{D_{th}(T)\tau_p} \qquad (2.22)$$

This indicates that the heating depth L_H is approximately the addition of the optical penetration depth L_a and the thermal penetration depth L_{th}. For the excimer laser (λ = 248 nm), L_H is equivalent to L_{th} since the corresponding L_α is less than 10 nm (see Table 2-1). However, L_H of the green laser system (λ = 532 nm) should consider L_α = 1.3 μm, but only at the solid state. Once the silicon reaches the molten phase, the optical penetration depth becomes negligibly small at all wavelengths as shown in Table 2-1. Therefore, the heating depth L_H of the laser-processed silicon is predominantly determined by the thermal penetration depth L_{th}, hence the pulse duration τ_p. This phenomenon is confirmed in Chapter 6.

2.3.3 Laser doping process

For silicon doping, Group III elements and Group V elements are used for p-type and n-type extrinsic silicon, respectively. The primary doping method in c-Si PV application is solid-state thermal diffusion where the impurity atoms move from the surface into the silicon crystal via the substitutional diffusion mechanism at high temperatures (900 ~ 1200 °C). The rate of diffusion is determined by the diffusion coefficient *D* of the impurity. This coefficient is also not constant but depends on the temperature and phase of silicon. Table 2-7 lists diffusion coefficient values of typical impurities in solid silicon at melting temperature and in the molten silicon [85]. The coefficient value in the solid phase is only in the order of 10^{-10} cm^2s^{-1}, therefore furnace diffusion is a slow process, lasting over a scale of minutes to hours. However, laser doping is a very fast process, typically taking less than a few microseconds for a similar doping depth processed via furnace diffusion, since laser doping is basically a liquid phase diffusion process.

Group	Impurity element	D in solid Si (cm^2/s)	D in liquid Si (cm^2/s)
III	B	1.0×10^{-10}	$2.4 \pm 0.7 \times 10^{-4}$
	Al	4.0×10^{-10}	$7.4 \pm 3.1 \times 10^{-4}$
	Ga	1.4×10^{-10}	$4.8 \pm 1.5 \times 10^{-4}$
	In	5.5×10^{-11}	$6.9 \pm 1.2 \times 10^{-4}$
V	P	1.0×10^{-10}	$5.1 \pm 1.7 \times 10^{-4}$
	As	1.0×10^{-11}	$3.3 \pm 0.9 \times 10^{-4}$
	Sb	1.3×10^{-11}	$1.5 \pm 0.5 \times 10^{-4}$

Table 2-7 Diffusion coefficients of impurities in solid and molten silicon [85].

Laser doping begins with the formation of silicon melts via laser irradiation. Dopant impurities then rapidly diffuse into the molten silicon. The melted region exists typically for only a few hundreds of nanoseconds, but it is enough for impurities to diffuse deeply due to the much bigger diffusion coefficients in the

liquid phase; approximately six orders-of-magnitude larger than those in the solid phase [85]. The molten region recrystallises via a liquid-phase epitaxy from the underlying unmelted silicon crystal. During recrystallization, diffused impurity atoms are integrated into substitutional sites in the lattice [86]. Because of the high speed non-equilibrium crystal regrowth, the density of substitutional dopants can readily exceed the equilibrium solid solubility limits [87].

Laser doping can be classified according to the application and structure of the dopant precursor, but the fundamental working principle is identical. Initial laser doping research was conducted in the late 1970s to early 1980s [77, 88] using a gaseous precursor flowing over the substrate. At the same time, there were also attempts to use a liquid precursor in laser doping. Initial 'wet' laser doping involved immersing a substrate in a bath containing a dopant-rich organic solution and irradiating its surface through the liquid with a pulsed laser [89]. Another type of 'wet' laser doping involved a laser beam guided within a chemical acid jet, fired at high pressure onto the substrate [90]. However, both gaseous and liquid laser doping imposed three challenges [91]: 1) slow throughput, 2) dealing with safety issues resulting from the remaining gaseous or liquid chemicals on the substrate, 3) incremental operating costs due to the complexity of the process. The currently favoured technique uses a solid film precursor, classified as a "Laser Induced Melting of Pre-Deposited Impurity Doping" (LIMPID) [92]. The dopant-rich solid film includes painted-on phosphorus [76], red phosphorus [93], sputtered boron [94], silicon nanoparticle ink [44], and a polymer-based phosphorus/boron spin-on dopant (SOD) [95]. Other solid precursors which could be readily integrated in c-Si cell processing are borosilicate (BSG) and phosphosilicate glasses (PSG), which are grown as a part of a furnace diffusion process. In most cases, LIMPID is a 'two-step' process which consists of the deposition of a solid dopant precursor and the removal of the remaining film after dopant incorporation via laser irradiation. However, the extra step of peeling off the residual dopant source layer could be removed by implementing a multi-purpose film as is used in PassDop technology. This technique utilises phosphorous-doped amorphous silicon-carbide films (a-SiC_x:P) as both a passivating layer and a dopant source layer [41]. Other PassDop-like cases were reported using a Al_2O_3/a-SiC_x:H stack [96] and a phosphorus-rich PECVD SiN_x layer [97]. This current work demonstrates that a stack of intrinsic amorphous silicon (a-

Si:H(i)) and boron doped amorphous silicon (a-Si:B) is also able to function as a multi-purpose film (Chapter 7). In other laser doping experiments in this thesis, a proprietary poly-boron precursor from *Filmtronics* is spun on the substrate and used as a solid dopant precursor.

2.4 LIMITATIONS OF THE CURRENT CHARACTERIZATION TECHNIQUES

For the characterization of doped silicon, a number of measurement techniques have been developed that show accuracy and reliability. As mentioned in 1.3, accurate measurements of the doping profiles and recombination properties of the doped silicon layer are critical for estimating the efficiency potential of the solar cell. In this section, traditional methods for measuring doping profiles and recombination properties in PV research are described with emphasis on their limitations when applied to localized features. Recently proposed characterization methods specifically developed for localized features are also reviewed. The purpose of this is to clarify the requirements for the new characterization method undertaken in this thesis.

2.4.1 Dopant density profiling

The easiest and simplest characterization method for doped semiconductor layers is the sheet resistance R_{sh} measurement via a four-point probe. The R_{sh} measurement is very convenient to judge the doping level quickly and a direct measure of the resistance of thin films that are nominally uniform in thickness. However, the practical dopant density across the doped region is typically not homogeneous, so it is necessary to measure the variation in dopant density for an accurate characterization of the doped region.

Four-point probe

A four-point probe (4pp) consists of four collinear probes with equal spacing, where a constant current is applied in the outer two probes and the voltage drop is measured in the inner two probes, as shown in Figure 2-6. The sheet resistance of a rectangular sample can be calculated using equation (2.23), where the correction factor C is based on the ratio of sample dimension a to d and on the ratio of the dimension d to probe separation s [98].

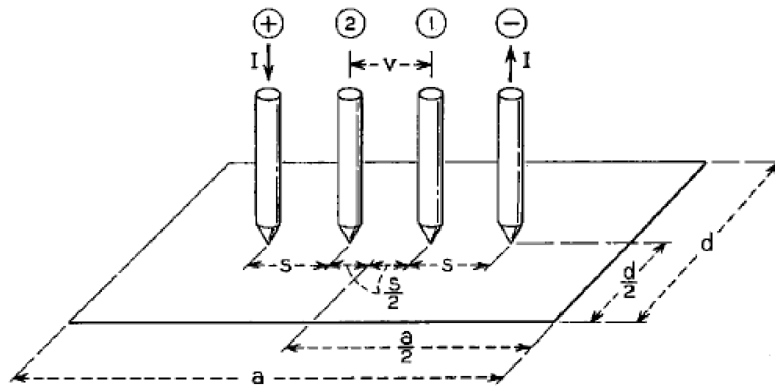

Figure 2-6 Configuration of four-point probes on a rectangular sample. The figure is taken from Ref. [98].

$$R_{sh} = \frac{V}{I} C\left(\frac{a}{d}, \frac{d}{s}\right) \tag{2.23}$$

A 4pp is the simplest and most reliable measurement for the sheet resistance R_{sh} of the heavily doped layer. However, it requires a sample size large enough (> 10 mm) to allow the probes to be placed. In order to use a 4pp on the laser-doped region, micron-scale laser beams are typically overlapped to create a relatively large doped area. The probe therefore cannot measure the actual R_{sh} of a locally laser-doped region. In addition, more detailed information on the doped layer, such as dopant density and doping depth, is unable to be measured precisely. A certain R_{sh} value in a doped layer could be a measurement either of a shallower profile with a heavier surface dopant density or a deeper profile with a lighter surface dopant density.

Electrochemical capacitance-voltage profiling

The Electrochemical Capacitance-Voltage profiling (ECV) technique is the most common tool used to measure doping profiles in semiconductors. ECV profiling basically consists of two steps: one is the measurement of the differential capacitance/voltage of a Schottky barrier at the semiconductor sample-electrolyte interface to obtain the carrier densities, the other is the electrochemical dissolution reaction to etch the material at a controlled rate. These two steps, the repetitive etch and measure cycles, are repeated to profile the dopant density as a function of depth.

A measured ECV profile could be used to extract the surface dopant density N_{surf} and the doping depth z_j, or it can be aggregated as the sheet resistance R_{sh} as follows

$$R_{sh} = \frac{1}{q\int_0^{z_j} \mu_{maj}(z)N(z)dz} \tag{2.24}$$

where $N(z)$ is a dopant density N at a certain depth z and $\mu_{maj}(z)$ is the corresponding majority carrier mobility, as determined by Klaassen's model [99, 100].

The semiconductor sample is placed in contact with the electrolyte to form the electrochemical cell (see Figure 2-7), designed by Ambridge and co-workers [101, 102] in the early 1970s. The sample-electrolyte interface works as the Schottky barrier without the need for metal Schottky contacts. When the interface is reverse-biased, a depletion region is created near the sample surface. Based on normal semiconductor-metal junction theory, the charge carrier density N at the edge of the depletion region of width w_d is given by

$$N(w_d) = \frac{1}{q\varepsilon_0\varepsilon_r A^2} \times \frac{C^3}{dC/_{dV}} \tag{2.25}$$

with

$$w_d = \frac{\varepsilon_0\varepsilon_r A}{C} \tag{2.26}$$

where ε_0 is the permittivity of free space, ε_r is the relative permittivity of the semiconductor sample, q is the electronic charge, A is the area of the semiconductor sample-electrolyte contact which is simply determined by the size of the mounting ring. Using a slowly modulated high frequency voltage, quantities of C and dC/dV at the edge of the depletion region are obtained and substituted in equation (2.25) to calculate the charge carrier density N. This carrier density is equivalent to the density of ionized dopant atoms within the depletion region. Since band bending in the depletion region leads to complete ionization of dopant atoms, the ECV technique measures all substitutional dopant atoms, so classified as an electrical profiling. Another function of the electrolyte is to dissolve the semiconductor sample for depth profiling. The etching of the sample depends on the dissolution current across the

semiconductor sample-electrolyte interface and the presence of holes. For the p-type semiconductor, majority carriers are holes, so dissolution is readily achieved by simply forward biasing the junction. However, the n-type semiconductor requires illumination to generate additional holes. Optically generated holes are then attracted to the surface by reverse biasing the junction and promoting the dissolution reaction near the sample surface.

Although the ECV technique is accurate and practical for determining all substitutional dopant atoms as a function of depth, it is destructive and can only be applied to relatively large (typically ~ 10 mm^2) and laterally uniformly doped samples. Furthermore, the measurement takes quite long time because of the slow etching rate (typically ~ 1 μm/hr). In this work, a *Wafer Profiler CVP21* from *WEP control* is used for the ECV measurement.

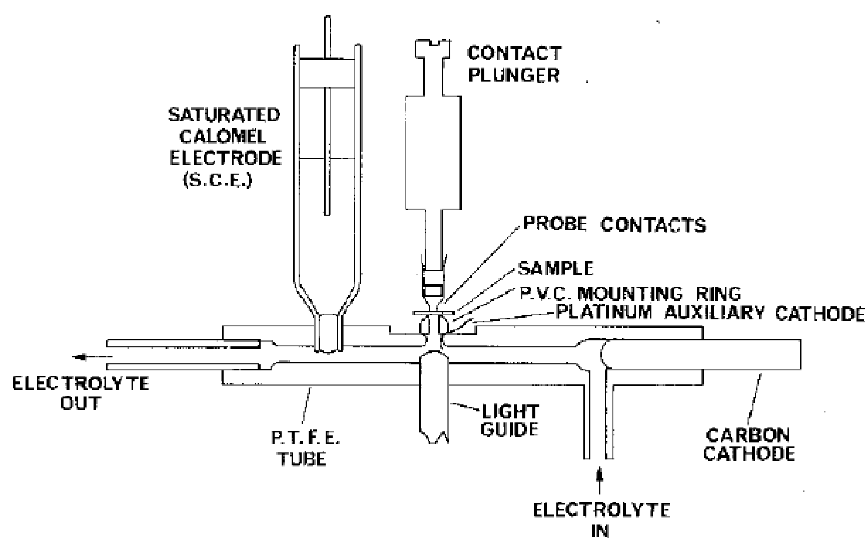

Figure 2-7 Schematic diagram of the electrochemical cell in an ECV profiler. The figure is taken from Ref. [101]

Secondary Ion Mass Spectrometry

Secondary Ion Mass Spectrometry (SIMS) is also frequently used to measure doping profiles in silicon. This technique involves chemical profiling which counts total dopant concentration without distinguishing between active and inactive dopant atoms, so classified as a chemical profiling. The spatial resolution of SIMS is so high,

typically about 0.1 μm laterally and in the order of 1 nm depth-wise, that it enables micron characterization of the sample even in two and three dimensions [103]. As a result it has been employed to measure the doping profile of locally laser-doped silicon by many researchers [77, 78, 88, 96, 104-107]. In addition, SIMS is capable of detecting all elements as well as isotopes and molecular species, so it can be used to detect the amount of unwanted impurities, such as oxygen and nitrogen, during the laser doping process [104, 108]. Unfortunately, SIMS is time consuming and expensive tool, unsuitable for frequent measurements.

Terahertz Time Domain Spectroscopy

Jen *et al* [109] presented a new approach to high-resolution dopant density mapping using transmission mode terahertz time domain spectroscopy (THz-TDS). THz-TDS is a spectroscopic technique in which the properties of materials are probed with very short pulses of terahertz radiation (a sub-picosecond pulse regime). Terahertz pulses are typically generated and radiated by an ultrashort pulsed laser on a sample using optical techniques. The THz pulses propagated through the sample are then measured in a detector that is simultaneously illuminated with the ultrashort laser pulse. In Jen's early work [110], the power ratios — pulses propagated through the sample divided by a reference pulse propagated the same distance through air or the reference sample — in the frequency domain were presented as a very sensitive indicator of dopant density. Since THz radiation absorption increases with a number of free carriers, and hence dopant concentration, the resonant peak amplitude of the power ratio decreases with dopant concentration as shown in Figure 2-8.

Based on this phenomenon, they predicted a doping profile by adapting repetitive etch-measure cycles like ECV profiling. The difference between this and the electrochemical approach used in ECV is that anodic oxidation is incorporated to remove the silicon, layer by layer.[2] The material library — which contains the THz radiation absorption and refractive index of doped silicon at several doping concentrations spanning the doping range of interest — is required to convert THz radiation measurements to dopant density. This method constructs the doping profile backwards from the last etched to the non-etched. The data of the last etching is analysed first, to determine the background dopant density by comparing it with the

[2] Authors mentioned that any other etching techniques can be incorporated.

reference wafer. The "(n+1) th" etched sample data is then used as the basis to estimate the dopant concentration in the "n th" etched sample. The accuracy of this method is greatly dependent on the precision and volume of the material library. Since THz-TDS dopant profiling is based on free carrier absorption in doped silicon, this technique is an electrical profiling like the ECV technique. Although the results of this method have been proven using experimental data comparing the constructed doping profile with the SIMS measurement [109], a comparison with ECV measurements would be more convincing.

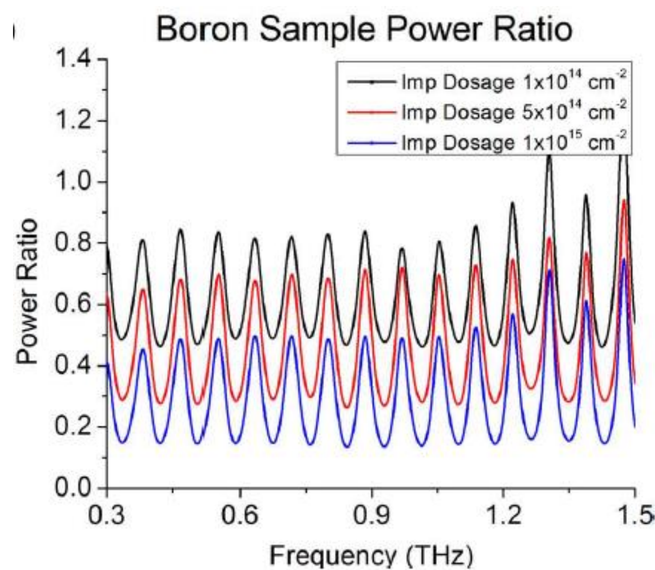

Figure 2-8 Power transmission ratios of different levels of boron concentration. The figure is taken from Ref. [110].

Secondary Electron Microscopy Dopant Contrast Image

Scanning electron microscopy (SEM) is generally used to visually inspect micron-structures in nanometre resolution. The most common SEM mode is detection of secondary electrons (SE) emitted from atoms excited by an electron beam. The detected SE not only reveals specimen topography, but also recognizes p- and n-type doped regions qualitatively using image contrast, in which p-doped regions appear brighter than n-doped regions [111]. It has even been found that the contrast level in the SE image depends on doping concentration levels [112]. Utilizing this phenomenon, known as the Secondary Electron Microscopy Dopant Contrast Image (SEMDCI), Xu *et al* [95] demonstrated 2-D dopant density mapping

of locally laser-doped silicon quantitatively, as shown in Figure 2-9. Based on the quantitative relationship between dopant density and image contrast from thermally diffused samples, SE contrast images of laser-doped silicon were converted to 2-D dopant density images. The most significant advantage of this characterization method is that dopant distribution over several orders of magnitude could be visualized easily in nanometre resolution. Other advantages of this method are its fast measurement capability, high spatial sensitivity and simple sample preparation. However, the quantification accuracy of this method is not as precise as ECV or SIMS; in particular the image contrast near the surface cannot represent actual surface dopant density due to the edge effect where electrons preferentially flow in and out [113]. Furthermore, the quantitative relationship of the dopant density-contrast is quite sensitive to substrate background dopant density and the SEM settings, which must be carefully controlled. To further ensure accurate quantification it is necessary to freshly cut before measuring.

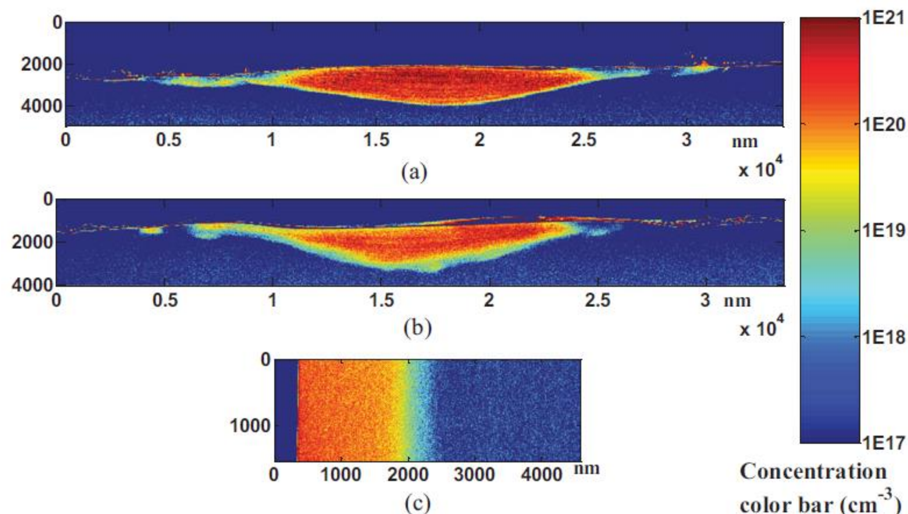

Figure 2-9 Two-dimensional boron concentration map of laser-doped samples processed with a Q-Switched DPSS laser with: (a) pulse energy of 15 μJ and pulse distance of 125 nm; (b) pulse energy of 17.5 μJ and pulse distance of 500 nm. (c) A thermally boron-diffused sample is given as the reference. The figure is taken from Ref. [95].

Photoluminescence based dopant density mapping

In silicon PV research, photoluminescence (PL) imaging is a very popular characterization method due to its numerous applications in spatially resolved characterization. One of the PL imaging applications is imaging of total dopant

density. Lim *et al* [114, 115] proposed two PL-based techniques for imaging dopant densities in silicon wafers. The first one determines the absolute boron density in p-type wafers by monitoring the rate of iron-boron (FeB) pairing after they are dissociated by optical or thermal perturbations. A series of PL images measured at intervals after the dissociation of FeB pairs are processed and converted to a dopant density image. Since this technique is based on FeB pairing and the observation of lifetime changes in PL images, sufficient Fe concentration in the wafer and surface passivation is necessary. The second technique determines the net doping concentration in either n- or p-type wafers by utilizing the linear relationship between PL intensity and dopant concentration in low injection. To ensure the linear relationship, a high bulk lifetime with an unpassivated surface is required to pin the excess carrier density.

These two PL-based techniques enable fairly simple and rapid dopant mapping but they are limited to wafers, and are not suitable for locally laser-processed features. The spatial resolution is relatively high but is limited to about a few hundred micrometres depending on the pixel size of the detector in the PL imaging tool. In addition, since these techniques are developed for the purpose of characterizing homogeneously doped wafers, they are not able to do depth profiling.

2.4.2 Recombination properties measurement

The recombination property of heavily doped regions is typically quantified by the recombination parameter J_0, which expresses cumulative recombination including radiative, Auger, SRH and surface recombination. This parameter represents a pre-factor in the calculation of the injection-dependent recombination current, so is frequently referred to as a standard measure of the quality of a doped region.

J_0 extraction via photoconductance decay measurements

The most common method for extracting J_0 is proposed by Kane and Swanson [116]. This method is based on measurements of the effective lifetime τ_{eff} of the simple p-n junction sample via the contactless photoconductance decay (PCD) method. The inverse τ_{eff} with the bulk intrinsic lifetime τ_b correction has the following relationship with J_0

$$\frac{1}{\tau_{eff}} - \frac{1}{\tau_b} = 2J_0 \frac{N_A + \Delta n}{qWn_i^2} \tag{2.27}$$

where n_i is the intrinsic carrier density and W is the sample thickness. Therefore, J_0 could be extracted by plotting the corrected inverse τ_{eff} as a function of injected carrier concentration. This method assumes that J_0, τ_{SRH} and n_i are constant over a range of injected carrier concentrations. The accuracy of this method is ensured by the use of a high-lifetime and high-resistivity substrate for high injection condition in the lightly doped substrate, and uniform carrier concentration throughout the sample [117]. The approximation of the uniform carrier concentration necessitates additional requirements, for example symmetric surface conditions, a relatively low J_0 of the doped region and transient generation condition. Andrew *et al* [118] accounted for the depth-wise non-uniform carrier concentration to improve J_0 accuracy by numerically solving the one-dimensional carrier concentration profile. This improvement is particularly effective for a moderately doped substrate with a higher J_0 when measured via the Quasi-Steady State PCD. Despite various theoretical assumptions and sample/measurement specifications, it is a widely accepted method to determine the J_0 of the heavily doped region. The requirements for the PCD measurements in this analysis, however, limit the minimum area of the doped region to be more than the size of an inductive coil in a PCD instrument; for example, only 4 different doped regions can be placed on a typical lab-scale 4-inch wafer.

Spatially resolved local recombination characterization

To overcome the spatial resolution limit of the conventional PCD based technique, imaging methods have been chosen and developed to characterize local recombination properties quantitatively. The most popular imaging methods are light beam-induced current (LBIC) mapping [119-121], lock-in thermography (LIT) [122, 123], and PL imaging [124, 125].

LBIC is the optical variant of the well-known method of electron beam-induced current (EBIC) imaging. Instead of an electron beam, a p-n junction sample surface is scanned by a focused laser beam and the induced current is measured for imaging. The sample requires external contacts to be under short circuit conditions hence the resultant raw image is an image of the short circuit current. The spatial

resolution is dependent on the excitation beam size, so it is possible to do a sub-micron scale measurement [121].

The LIT method uses a thermocamera to image local recombination characteristics. Certain local heat sources are periodically applied by various means, typically at a modulation frequency of 10 Hz. The measured infrared (IR) images are then evaluated to images of the local temperature modulation amplitude and the phase. When LIT is performed in the dark (DLIT), the recombination current can be quantitatively imaged. The -90˚ phase shifted component of the DLIT image, taken under two or three different bias voltages, can be converted to the local recombination current density image [122]. The resolution of DLIT is in millimetres, typically about 2 mm for a 10 Hz modulation, due to thermal diffusion length.

PL imaging is the latest, but most popular method in PV research. Basically, this technique is a measurement of the radiative recombination of excess carriers after homogeneous illumination with appropriate light filtering to eliminate the excitation light. PL imaging was initially demonstrated as an alternative method of measuring the effective lifetime of the PCD measurement [126]. With appropriate additional experimental conditions and theoretical interpretations, local series resistance and recombination current images can be obtained from PL images [125].

Although the above three techniques are able to characterize various properties spatially they are typically limited to the wafer or device level. In addition, in order to quantify/map the recombination current, the formation of external contacts is necessary for all methods.

Analytic approach to extract J_0 using a PL image and simulation

Fell *et al* [52] proposed a new approach to quantify the recombination properties of locally doped regions, using a PL image and 3-D numerical simulations using Quokka [127]. This approach employs 2-D/3-D carrier transport modelling to fit the unknown local recombination property to a measured quantity. A sample structure requires an unprocessed reference region, which needs to be sufficient in size for a PCD measurement. In other regions of the sample, the locally doped regions form arrays with specified pitches in the x-and y-directions. The size of the array also should be considered, to minimize the smearing effect from adjacent processed/unprocessed regions in the PL measurements.

The first step in this analysis is the derivation of the recombination property, $J_{0,pass}$ or surface recombination velocity S_{pass}, of the reference region and the measurement of basic parameters, such as thickness W and bulk resistivity ρ. Using PCD measurements, the τ_{eff} in the reference region is measured. Iterative simulations of the carrier lifetime curve using Quokka's optimizer function are performed, with varying $J_{0,pass}$, until the optimal fit to the measured carrier lifetime curve is obtained. Additionally, the SRH-dominated bulk lifetime could be a variable together with $J_{0,pass}$ in the simulation, if the bulk lifetime is not clearly determined (see Figure 7-2).

In the next step, measured PL signals in the reference region are correlated with the simulated PL to derive the calibration factor. PL signals in the reference region are taken at various illumination levels; distinct levels of photon flux are recorded using a photodiode. The PL imaging tool used in this work is a BT Imaging LIS-R1. The excitation source is a homogenized 808 nm laser. A silicon CCD with a short-pass filter captures the emitted PL signal with a cut-off wavelength of 1025 nm, to reduce the light smear. The optical properties, external reflection R_{ext} at the excitation laser wavelength (808 nm), and the internal reflections of the front and rear sides R_f & R_r over a range of wavelengths (250 ~ 1600 nm) of the sample, are characterized via OPAL 2 [128] or direct measurements. Setting all measured and simulated parameters as boundaries in Quokka (e.g. W, ρ, bulk lifetime, $J_{0,pass}$, R_f, R_r, R_{ext}), PL signals over the range of excitation photon flux used to take PL images of the reference region are simulated. The calibration factor is then determined from the ratio of the measured PL signal to the simulated PL signal at the same excitation photon flux.

$$C = \frac{I_{PL,measured}}{I_{PL,simulated}} \; [counts\ s^{-1}] \qquad (2.28)$$

where the $I_{PL,measured}$ is the averaged PL count across a region equivalent to the detection area of the inductive coil used to extract the τ_{eff} in the reference region.

The third step establishes simulated PL signals versus the recombination parameter $J_{0,d}$ of the locally doped regions curve, to extrapolate $J_{0,d}$ from measured PL signals. In order to simulate PL signals, it is necessary to define a 3-D domain of a unit cell replicating the geometrical properties of the locally doped sample structure

in Quokka. Figure 2-10 depicts the exemplary 3-D domain of the unit cell used in Chapter 6 to analyse recombination of locally laser-doped regions.

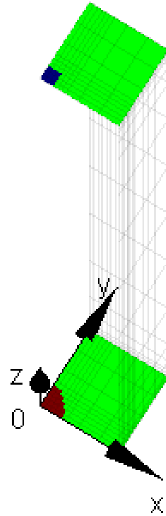

Figure 2-10 3-D domain of a unit cell used in local recombination analysis in Chapter 6. Red is a circular laser-doped p+ region. Blue is a virtual contact for simulation. Green represents the no-conductive boundaries. Width and height of a unit cell is a half of actual pitch size.

The previously derived $J_{0,pass}$ value is used for the passivated (green) region. The only simulation parameter varied is the recombination parameter $J_{0,d}$ of the locally doped (red) region. Simulated PL intensity is then calibrated with the calibration factor C which is obtained from the previous step (Equation (2.28)). Figure 2-11 shows an example of the simulated PL curve as a function of $J_{0,d}$ with different pitches. It is worthwhile noting that the sensitivity of the PL signal is affected significantly by the pitch size — the pitch size should be chosen carefully for clear distinction of low value $J_{0,d}$ from the PL intensity. For example, in Figure 2-11, $J_{0,d}$ in a range between 100 and 1000 fA/cm^2 is only distinguishable with 60 μm pitch.

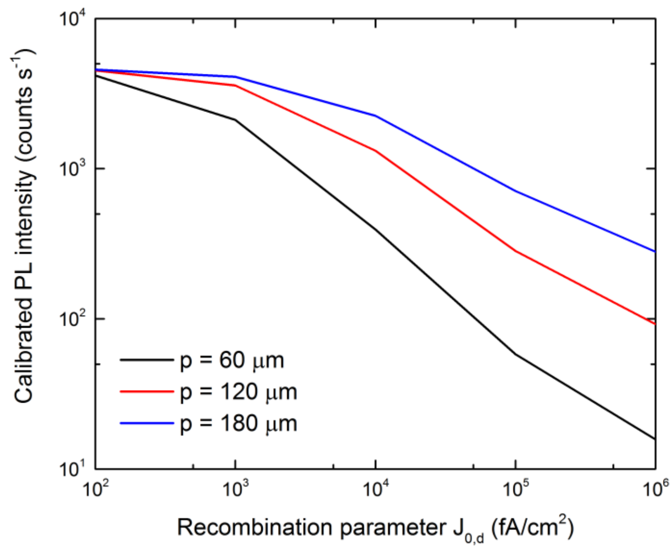

Figure 2-11 An example of simulated PL intensity for a constant pitch of 60 µm, 120 µm and 180 µm as a function of local recombination parameter $J_{0,d}$.

Finally, the measured uncalibrated PL image of the locally doped sample is converted to the $J_{0,d}$ image by extrapolating $J_{0,d}$ values using this curve, as depicted in Figure 2-12. We use an averaged value across a processed area to represent local recombination $J_{0,d}$ in this study.

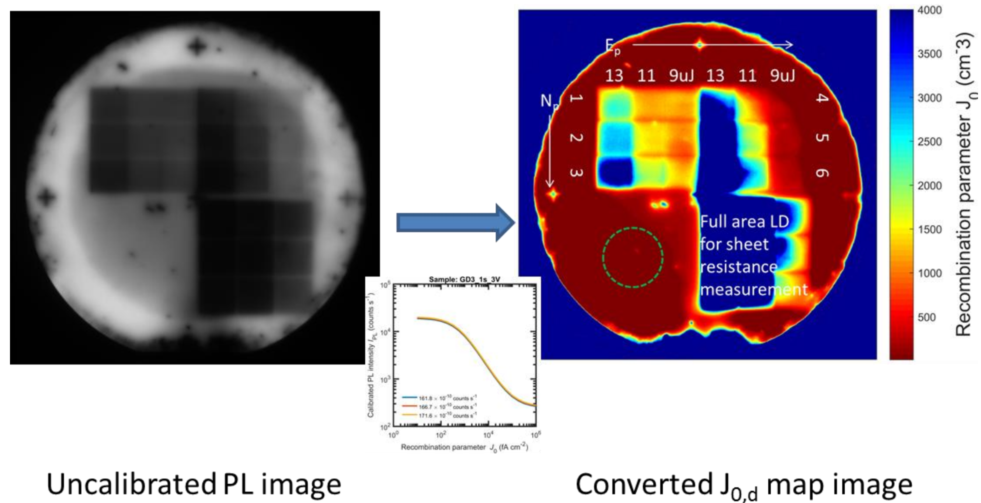

Figure 2-12 A calibration curve established by correlating measured τ_{eff} and PL counts in the reference region (green dot circle) is used to extrapolate the $J_{0,d}$ values of the locally laser-doped sample from the uncalibrated measured PL image.

This analytic approach is able to examine the recombination properties of localized features, since measurements and simulations are conducted directly on localized features without scaling up the doped region using overlapping laser pulses. Additionally, an extensive range of parameters could be examined in a single PL measurement by fitting many small boxes of arrays on a standard lab-scale size substrate. However, this method is not a direct measurement/characterization of the localized features. Because of the resolution limit of a PL image, area-averaged PL counts — in which all PL emissions from the localized features and other regions are aggregated — are used and linked to the simulation. The simulation thus estimates the overall PL emissions of a unit cell according to the variable $J_{0,d}$ of a locally doped region, under the assumption that the other properties are homogeneous across all unit cells. The properties of the localized features themselves are also assumed to be uniform. As a result, the accuracy of this method is heavily dependent on precise measurements of parameters, such as resistivity, thickness, passivated surface recombination properties and the optical properties of dielectric film. Small errors or uncertainties in the measured parameters would propagate at each step as the analysis proceeds. In the same way, homogeneous passivation and bulk substrate are essential for accurate characterization.

2.5 SUMMARY AND IMPLICATIONS

In this chapter background knowledge relevant to this study, including the properties of silicon and the working principles of laser/silicon interaction, are described. This has been done not only to assist with understanding the theory behind laser/silicon interaction, in particular laser doping, but also to reference influential factors which must be considered in the application of the low temperature μ-PLS measurements used in later chapters.

This chapter also demonstrates that conventional characterization methods, usually employed in PV research for measuring doping profiles and recombination properties, are not suitable for localized features due to the lack of spatial resolution. It has also been shown that even more recently developed characterization methods have some drawbacks. Table 2-8 and Table 2-9 summarize the main features of

reviewed characterization methods for evaluating doping profiles and recombination properties, respectively, along with their drawbacks.

For dopant density mapping, information about electrically-active dopant concentration is typically more valuable in analyses of the electronic properties of a solar cell, such as series resistance and contact properties. For this reason, an electrical profiler is preferable to a chemical profiler in PV research. Conventional depth profiling always works in a destructive manner, for example etch-measure cycles, as shown in ECV, SIMS and THz-TDS. A repetitive working mechanism such as this naturally leads to a slow process. It additionally requires a precise depth control module/apparatus thus increasing the complexity of the measurement. However, when the capability is weighted to rapid 2-D mapping, the depth profiling function is diminished, as in PL-based techniques. Although SEMDCI is able to do cross-sectional 2-D rapid and high-resolution dopant mapping, its accuracy and sensitivity to external conditions make it difficult for it to be an optimum method for localized features.

The quantification of recombination properties is not straightforward, as has been shown in all the methods. A specific sample structure, external conditions or theoretical boundaries are typically required or considered, and they should be determined carefully. In addition, extra sample preparations and the formation of external contacts are typically required, as was illustrated in the LBIC, DLIT and PL methods. Furthermore, with the exception of μLBIC, their resolution is not high enough to observe the variation in recombination properties across the localized feature with sub-micron precision.

Consequently, it is worth developing a characterization method that is capable of:

- Electrical dopant profiling and recombination properties in lateral 2-D and depth-wise 1-D
- Rapid and non-destructive measurement
- Accurate measurement with high spatial resolution in sub-micron precision
- Simple measurement without extra sample preparation

In this thesis, μ-PLS is proposed as a solution which satisfies all of the above requirements. Before going on to verify it experimentally, the basic principles of μ-PLS and its applications used in this thesis are described in the next chapter.

	Profiling type	**Measurable dimension**	**Spatial resolution**	**Main drawbacks**
4pp	N/A	Planar 2D	~ 10 mm	No depth profiling
ECV	Electrical (Substitutional dopants only)	Depth-wise 1D	~ 10 mm^2	• Low resolution • Destructive • Slow process
SIMS	Chemical (Total dopant concentration)	1/2/3D	~ 0.1 μm	• Destructive • Costly • Slow process
THz-TDS	Electrical	1/2/3D	Possibly Sub-μm regime	• Destructive • Require accurate 'material library' and algorithm
SEMDCI	Electrical	Cross-section 2D	Sub-nm regime	• Less accuracy • Sensitive to substrate doping and SEM setting
PL image-based technique	Electrical	Planar 2D	~ 160 μm depending pixel size of CCD	• Low resolution • No depth profiling

Table 2-8 Summary of the current dopant profiling techniques

	Spatial resolution	Contact requirement	Main drawbacks
PCD	Depending on inductive coil size (typically cm regime)	X	• Low resolution • Only for low J_0
LBIC	Sub-μm regime	O	Contact formation
DLIT	Sub-mm regime	O	Low resolution
PL	~ 160 μm depending pixel size of CCD	O/X	• Low resolution • Require contacts for J_0 quantification
Analytic PL+Simulation	Depending on simulation boundary condition	X	• Precise measurements of boundary parameters • Assumption/Requirement of homogeneous boundary parameters

Table 2-9 Summary of the current measurement techniques for recombination properties

Chapter 3. Methodology for μ-PLS characterization of localized features

3.1 OVERVIEW

In this thesis, μ-PLS is proposed as a solution for characterizing localized features. To underpin why μ-PLS is suitable for local characterization, this chapter provides detailed information about μ-PLS. After a general description of the working principles of μ-PLS, the luminescent responses of silicon under specific conditions are described, along with existing applications that have been previously detailed in the literature. Details on luminescence and its particular application to this work are given. Hardware systems, including the laser processing systems and μ-PLS measurement systems used in this thesis, are also introduced.

3.2 WORKING PRINCIPLES OF LOW TEMPERATURE MICRO-PLS

When a material is illuminated by a laser beam with energy larger than the band-gap of the material, electrons in the material are excited to a higher energy level — the so-called photo-excitation. The excited electrons finally recombine with holes and then release energy as they relax and return back to a lower energy level. When the relaxation energy form is the emission of photons (luminescence), this process is called photoluminescence (PL). By analysing the emitted PL in a spectrum, photoluminescence spectroscopy (PLS), more detailed information about the material can be obtained. When photo-excitation is confined to a small area less than 10 μm diameter, it is defined as micron-photoluminescence spectroscopy (μ-PLS). Since the PLS technique is based on the energy transition between the conduction band and the valence band, the measured PL spectrum naturally contains information regarding the band structure of the material. Furthermore, PLS measurements at low temperatures reveal more detailed information about the band structure, for example the degree of BGN [129, 130] due to heavy doping. In addition, sub-band-gap emissions from defect or dislocation levels are only observable at lower temperatures, since at higher temperatures the carriers trapped at the defect/dislocation levels are thermally excited back to the band edges [131, 132].

3.3 PHONON-ASSISTED RADIATIVE RECOMBINATION OF INTRINSIC SILICON

As briefly mentioned in 2.2.1, silicon is an indirect band-gap material, which in turn requires additional phonon emissions or absorptions to adjust the crystal momentum for the inter-band transition, as shown in Figure 3-1. This is represented as multiple luminescent peaks (see Figure 3-2). All spectral peaks represent the radiative recombination of free electron-hole pairs with the assistance of momentum-conserving phonons. Since different phonon modes and energy are associated in each peak, peaks are separated by the amount of associated phonon energy. Table 3-1 summarizes detailed information on all PL peaks of intrinsic silicon, including their energy, associated phonon's mode and energy level, and their relative intensity. All notations and values are taken from Ref. [133]. With the exception of the TO and TO + O^{Γ} peaks, all peaks are visible only at low temperatures of less than 50 K, otherwise they merge into a single and broad peak as temperature increases (see Figure 3-3).

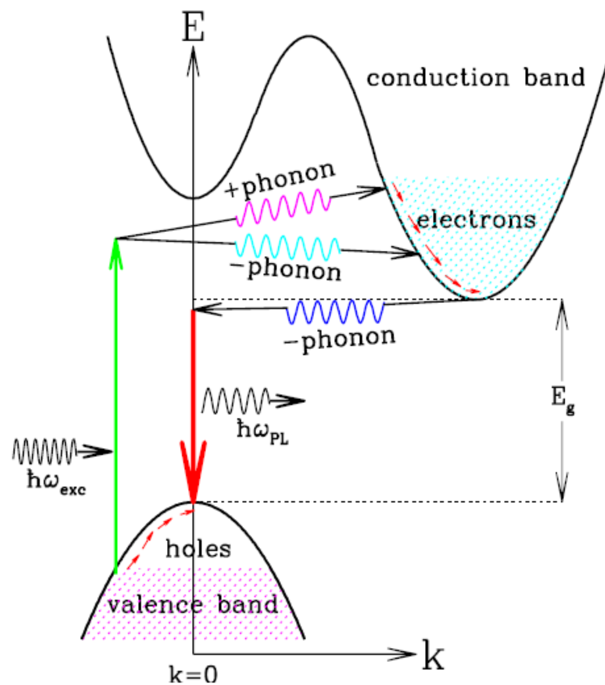

Figure 3-1 Band diagram illustration for the photoluminescence process in silicon. The momentum conserving phonons are associated in the radiative recombination.

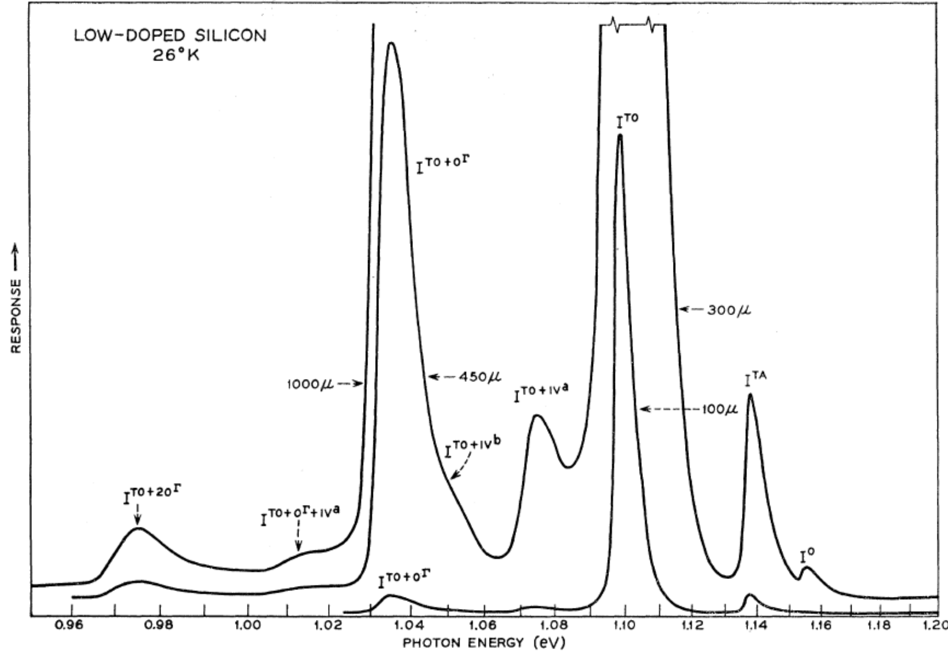

Figure 3-2 PL spectra of intrinsic silicon (lightly phosphorus-doped 2×10^{14} cm^{-3}), measured at 26 K. All spectral peaks represent the radiative recombination of e-h pairs with the assistance of the indicated phonons. Detailed information on all peaks is listed in Table 3-1. The figure is taken from Ref. [133].

Threshold energy		**Phonon energy**	**Assignment**	**Relative intensity**
eV	nm	meV		
1.1545	1073.9	~ 0	NP	~0.004
1.1365	1090.9	18.3	TA	0.035
1.0970	1130.2	57.8	TO	1.00
1.074	1154.4	80.8 (57.8 + 23)	TO + IV^{a}	0.016
1.051	1179.7	103.8 (57.8 + 46)	TO + IV^{b}	~0.008
1.0315	1201.9	122.3 (57.8 + 64.5)	TO + O^{Γ}	0.07
1.013	1223.9	142 (57.8 + 64.5 + 21.5)	TO + O^{Γ} + IV^{a}	~0.0025
0.968	1280.8	187 (57.8 + 64.5 + 64.5)	TO + $2O^{\Gamma}$	~0.01

Table 3-1 Threshold energy, associated phonon mode/energy and relative intensities of PL peaks in Figure 3-2 with notations as defined by Dean *et al* [133]; TA – transverse acoustical, TO – transverse optical, Γ – centre of reduced zone-zero wave vector, IV – phonon selected for intervalley scattering of electrons (two phonons, a and b).

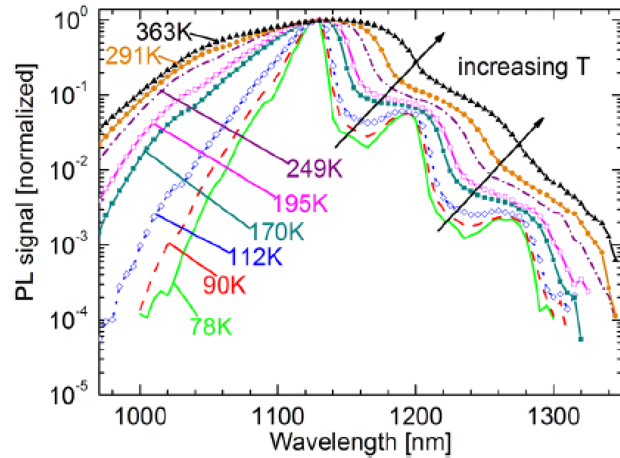

Figure 3-3 Temperature dependence of intrinsic silicon PL spectra in the temperature range of 78 K ~ 363 K. Peaks merge into a single broad and low peak as temperature increases. The figure is taken from Ref. [134].

At our μ-PLS measurement temperature (liquid-nitrogen temperature ~ 80 K), two main peaks are clearly observable: one of which is a 1130 nm peak associated with the TO phonon only, whereas the other is a 1200 nm peak associated with the TO and O^{Γ} phonons as shown in Figure 3-4. Hereafter, a peak near 1130 nm is named as a Si BB radiative peak (close to silicon E_g) and a peak near 1200 nm as a Si phonon replica.

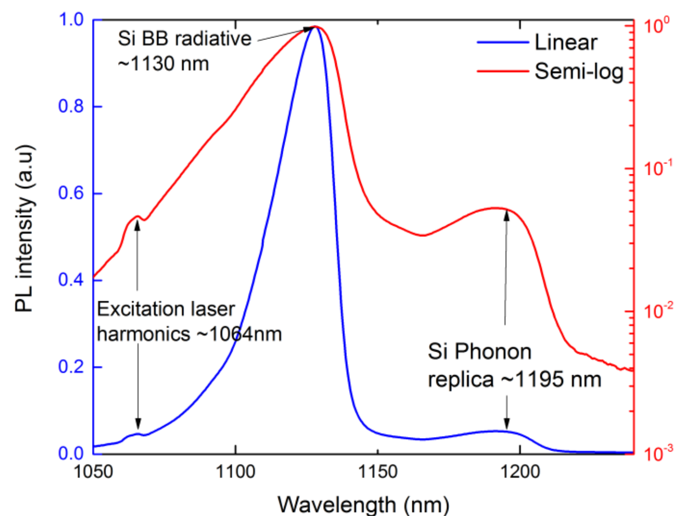

Figure 3-4 PL spectra of intrinsic silicon measured at liquid-nitrogen temperature (~ 80 K) in linear (blue) and semi-log (red) scales, using a 532 nm DPSS CW laser with an excitation power of 11 mW (~ 130 kW/cm^2). Except for a laser harmonics peak at around 1064 nm, two peaks related to radiative recombination in silicon are observed.

3.4 IMPACT OF DOPANT IMPURITIES ON PL SPECTRA

Dopant impurities in silicon are represented by a shallow dopant energy state (near the conduction band for n-type, near the valence band for p-type) in the band-gap diagram. Figure 3-5 illustrates the band structure of lightly doped and heavily doped p-type silicon, showing that the band structure differs significantly according to the impurity concentration. For lightly doped p-type silicon, the dopant band is close to the valence band, but separated clearly from the valence band (E_A in Figure 3-5 (a)). From the dopant band, the radiative recombination occurs in addition to the radiative recombination relating to the intrinsic band-gap. As can be seen in the figure, the gap between the conduction band edge and the dopant band is slightly smaller than the intrinsic band-gap. As a result, the dopant band bound luminescent peak locates at a slightly higher wavelength (~ 1150 nm) than the wavelength of the intrinsic band-gap PL peak (Si BB radiative peak ~ 1130 nm in Figure 3-4). Utilizing this phenomenon, Tajima [135] developed the first PLS-based technique for quantifying boron and phosphorous dopant concentration in silicon. He found that the PL intensity ratio of the dopant bound PL peak (either boron or phosphorus) to the intrinsic PL peak has a linear relationship with dopant concentration. Colley and Lightowlers [136] applied the same technique and reported transferable calibration curves for measuring boron, phosphorous and aluminium concentrations after correcting the PL spectra for the measurement system response. However, the above PL analysis methods were all based on PL signals measured at the liquid helium temperature of 4.2 K and limited to light dopant density in a range of 10^{12} cm^{-3} ~ 10^{15} cm^{-3}. This detection range was extended up to a dopant concentration of 10^{17} cm^{-3} by Iwai *et al.* [137], who used the same technique but increased the measurement temperature to 20 K. Recently, Liu *et al* [138] demonstrated that this technique is also valid at relatively high temperatures (liquid-nitrogen temperature ~ 80 K), and were even able to measure up to a dopant concentration of about 5×10^{17} cm^{-3}.

For more heavily doped (> 10^{18} cm^{-3}) silicon however, such a method cannot be applied, since the band structure of heavily doped silicon is totally different compared to that of lightly doped silicon as seen in Figure 3-5. When the dopant concentration increases, in particular to more than the Mott transition (> 2×10^{18} cm^{-3}), there are at least four simultaneous phenomena as follows:

1. The conduction band and the valence band rigidly shift toward one another due to many-body effects [139]. Mutual exchange and Coulomb interactions among the increased free carriers cause a downward shift of the conduction band. This shift is further enhanced by ionized impurity scattering. The valence band is affected in the opposite way, so causing an upward shift [140].
2. The two band edges have “tailing” into the band-gap due to the effect of a random impurity distribution [139]. The actual impurity distribution in heavily doped silicon is nearly random. The fluctuation of the local potential due to the random distribution of ionized impurities causes a spatially dependent distortion of the quantum density of states. However, the statistical average of the fluctuating density of states over the entire lattice merges into a certain exponential function, the so-called band tail. The band tail leads not only to a marginally smaller band-gap but also to a wider distribution of free carriers around the two band edges.
3. The dopant band merges with the band tail to form a more extended band tail [141]. In lightly doped silicon, dopant impurities create localized states, all of which have the same discrete energy level, owing to sufficient space among dopant atoms preventing any quantum-mechanical interaction. However, in highly doped silicon, randomly distributed dopant atoms with small spacing result in a statistically averaged variation of the dopant energy level, forming a dopant band. The width of a dopant band increases with the dopant concentration, hence eventually combining with the band tail at a dopant concentration above the Mott transition.
4. The Fermi level moves into the valence band (for p-type silicon), which means the semiconductor becomes degenerate [142].

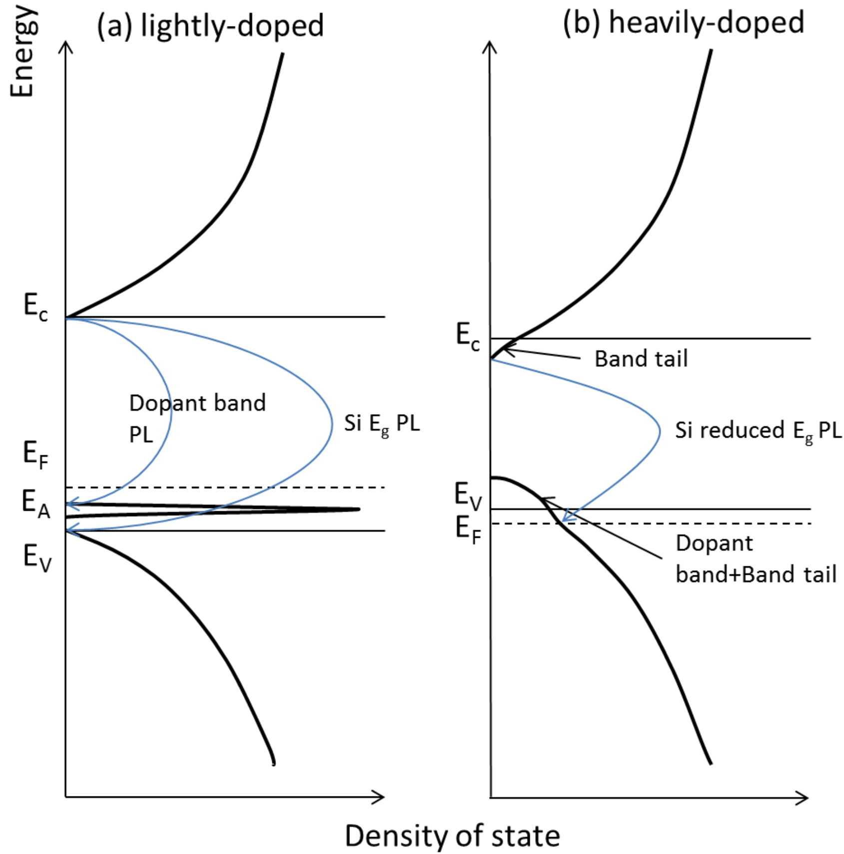

Figure 3-5 Schematic illustration of the band structure of (a) lightly-doped and (b) heavily-doped p-type silicon. Simplified band-band luminescence channels are given for each band structure. E_c, E_v, E_A, and E_F are the conduction band, the valence band, the acceptor dopant energy level, and the Fermi level, respectively.

Nguyen and Macdonald [143] demonstrated the separate impact of the above four phenomena on the luminescence spectra of heavily doped p-type silicon. The narrowing band-gap definitely incurs a PL spectrum shift toward longer wavelengths (lower energies). However, the Fermi energy level has a counter effect on this shift toward higher wavelengths. As the Fermi level moves further below the valence band, the PL spectrum shifts not only toward shorter wavelengths (higher energies) but also broadens because of increased optical band-gap (gap between E_c and E_F in Figure 3-5) and band filling effects. In addition, the wider carrier distribution over the energy level due to perturbed bad edges (band tail + dopant band) leads to spectrum broadening. Accounting for all those impacts, the influence of the dopant density on the PL spectrum is observed via two simple properties of the spectrum (1) the shifting of PL peaks and (2) the broadening of the peaks.

Utilizing this phenomenon, Roigè *et al* [48] demonstrated the dopant density quantification of heavily laser-doped micron-structures. Their approach was based on PL spectra measured at room temperature. They observed that the broad room temperature PL spectrum shifts and widens progressively towards longer wavelengths for dopant density above 5×10^{18} cm^{-3}. By monitoring the intensity-weighted spectral position of the PL spectrum, they established a calibration curve and applied to dopant density quantification of locally laser-doped regions. However, it is not explicitly stated whether the measured density is the surface dopant density or the depth-wise averaged density. Heinz *et al* [47] also presented lateral 2-D mapping of dopant density, using the μ-PLS system. However, their approach was based on the PL intensities which were obtained from two PL measurements with the large and small pinhole sizes of a confocal microscope at room temperature, rather than analysing spectral positions of the PL spectrum.

3.5 IMPACT OF CRYSTALOGRAPHIC DEFECTS ON PL SPECTRA

The first observation of dislocation-related photoluminescence in silicon was reported by Drozdov *et al* [144] in 1976. They found that dislocations in silicon give rise to four characteristic deep-level PL peaks, the so-called "D-line"; D1 (0.812 eV ~ 1527 nm), D2 (0.875 eV ~ 1417 nm), D3 (0.934 eV ~ 1327 nm), and D4 (1.000 eV ~ 1240 nm), as shown in Figure 3-6. Since then, D-lines have been studied intensively to reveal their physical origins and characteristics.

Suezawa *et al* [131] proposed a model in which two different traps, one with a shallow level and the other with a deep level in the band-gap, are related to the radiative recombination process of each D-line PL peak (see Figure 3-6). In later experimental results, their physical origins were clarified. Sauer *et al* [132] categorized the four D-lines into D1/D2 and D3/D4 groups based on evident observation of their consistent spectral response in pairs. They hypothesized that the D1/D2 lines originate from secondary defects around dislocations while the D3/D4 arise from the dislocations themselves. This grouping has been verified by many researchers and is now generally accepted. Higgs *et al* [145], based on highly spatially resolved cathodoluminescence spectroscopy, reported that the intensities of the D1/D2 lines are higher between slip dislocations, while those of the D3/D4 lines

are higher on slip dislocations. Using μ-PLS mapping around the grain boundaries of mc-Si, Tajima *et al* [51] demonstrated that the D1/D2 lines were distributed around grain boundaries, whereas the D3/D4 lines were located directly at grain boundaries. They additionally found a preferential oxygen precipitation-related PL peak (labelled D_b), which has an energy level close to the D1 line, on the dislocations [49, 51]. Nguyen *et al* [146] demonstrated that the D1 and D2 lines have different origins. They showed that the D1 line was enhanced when the metal impurities at the dislocations were cleaned, whereas D2 remained unchanged. They also assumed that D3 is not the phonon replica of D4 and that they might have different origins, since both lines showed different energy shifts when measured away from grain boundaries.

The spectral shapes of D-lines are critically dependent on the dislocation density. Sauer *et al* [132] demonstrated that D-lines intensities grow clearly as dislocation density increases, whereas the band-band luminescent peak (Si BB radiative) is effectively quenched. In addition, the sharp D-lines are merged, forming a broad band as the dislocation density increases > 10^9 cm^{-2}.

The D-lines are also heavily dependent on temperature. As mentioned briefly in 3.2, all D-lines are clearly observable at temperatures below 90 K. All D-lines become weaker as the temperature is raised. D1/D2 lines and D3/D4 lines merge into two bands above 90 K. As the temperature increases above 150 K, the deep-level PL is represented as one featureless broad band and its intensity decreases as it approaches room temperature [51]. However, the oxygen precipitation related PL component D_b, which even emits from deep levels close to the D1 level, is still observable at room temperature [49, 51].

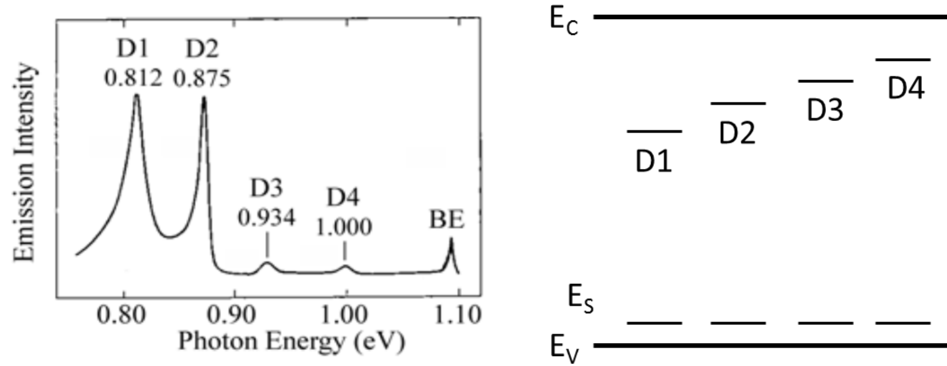

Figure 3-6 (Left) Dislocation-related D-lines of PL spectra, measured at 4.2 K from plastically deformed silicon [144]. (Right) Band structure illustration for the recombination of D1~D4 lines, proposed by Suezawa *et al* [131]

3.6 CHARACTERISTICS OF THE PL SPECTRA OF HEAVILY DOPED LAYERS

Locally heavily doped layers created via thermal diffusion, laser doping, or ion implantation are formed at the surface region. The depth of the doped layers for PV application is typically less than a few micrometres with inhomogeneous dopant density along the depth. Therefore, when the heavily doped layer is excited with an excitation laser source which has an absorption depth greater than the doping depth, PL is emitted from both the heavily doped layer and the intrinsic silicon substrate. As a result, the detected PL spectrum is a superposition of the spectra from the heavily-doped layer and the intrinsic silicon substrate. Figure 3-7 shows the normalized PL spectrum of the heavily doped silicon sample via laser doping and illustrates a superposition of the PL components from both layers. The doping peak represents PL components from the heavily doped layers. Owing to the BGN as described in 3.4, the wavelength of the doping peak is slightly higher (lower energy level) than that of the Si BB radiative peak. A phonon replica of the doping peak is also observable at around 1225 nm. Since the wavelength of D4 line is also close to that, the 1225 nm peak could be a mixture of the D4 line and a phonon replica of the doping peak, if the sample contains dislocations.

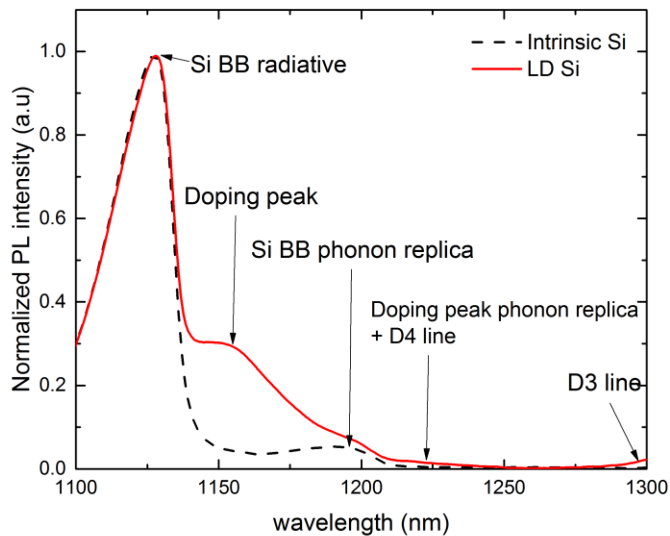

Figure 3-7 Superposition of PL emissions from the heavily doped layer and the intrinsic silicon substrate result in two distinctive peaks, the Si BB radiative and doping peaks. The spectrum from an undoped silicon sample (Intrinsic Si) is given for comparison. The spectrum was measured from a heavily laser-doped silicon sample (LD Si).

In order to analyse the characteristics of the doping peak more clearly and easily, the PL component from the underlying silicon substrate is subtracted as illustrated in Figure 3-8. In Chapter 5 and Chapter 6, this subtraction of intrinsic silicon PL component is used in the analysis. It is quite useful for the PL spectra of relatively lightly doped samples which have either a light surface dopant density or a shallow doping depth. Since the observation of dislocation in the heavily laser-doped samples is one of this work's interests, and has been demonstrated by many authors [147, 148], it is also useful to highlight dislocation-related PL peaks (D3 and D4 lines) at above 1200 nm wavelength ranges by removing undamaged intrinsic silicon PL component.

In this work, all PL spectra were normalized to a Si BB radiative peak (~ 1130 nm) unless specifically stated. The first purpose of the normalization was to clearly show specific features in the PL spectra relating to doping and defects/dislocations. The second purpose was to compare samples processed on different substrates. The absolute PL intensity is proportional to the p-n product and is thus heavily dependent on the carrier lifetime of the substrate, excitation conditions and the optical properties/morphology of the sample surface. Therefore, direct comparison of absolute PL intensities is meaningful under limited conditions, whereas normalization of PL intensities enables comparison among different substrate

conditions under relaxed conditions. Lastly, the relative intensity still has a lot of meaning since the excitation volume is fixed. For example, the relative PL intensity of the doping peak can be seen as a portion of the heavily doped layer of the total excited volume.

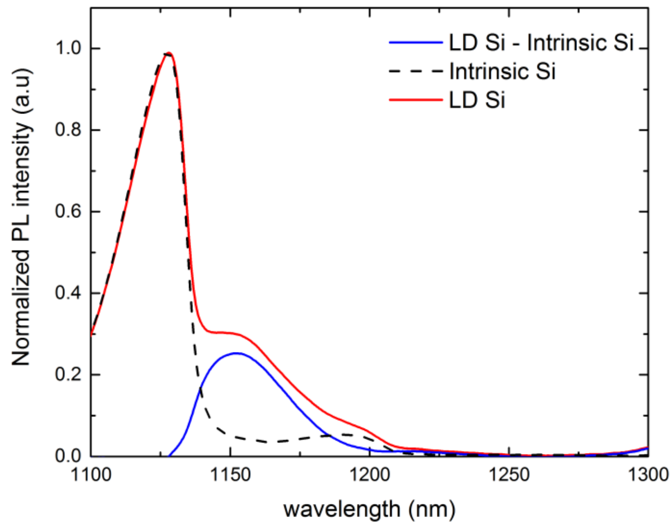

Figure 3-8 Decoupling the PL emissions of the heavily laser-doped layer from the PL spectrum shown in Figure 3-7 by subtracting the PL component of intrinsic silicon.

3.7 MICRO-PLS SYSTEM CONFIGURATION AND SETUP

Two μ-PLS systems from the same manufacturer were employed in this work. One is the old system, *Horiba T64000* and the other is the new system, *Horiba LabRAM*. The old system was employed in Chapter 4 and Chapter 7, and the new system was used in Chapter 5 and Chapter 6. Both systems have the same system configuration, as depicted in Figure 3-9. The difference is the detection sensitivity and precision of the sample stage step for mapping. The new system has much better sensitivity and more precise sample stage control. Other system specifications/conditions are identical or equivalent for both systems.

The excitation laser beam was focused onto the sample surface via a 50 × objective lens whose numerical aperture is 0.55. The focused excitation-spot diameter was approximately 1 ~ 2 μm. The emitted PL was directed into a monochromator whose grating was set at 150 grooves/mm, providing a spectral resolution of 0.25 nm. It was then detected by a liquid-nitrogen-cooled InGaAs array detector for a spectrum range between 800 nm and 1600 nm, or by a silicon detector

for a spectrum range between 400 nm and 1000 nm. The sample stage has a minimum step size of 0.1 μm in both the X and Y directions enabling fine 2-D mapping across the sample surface (only applicable for the new system). A liquid-nitrogen-cooled *Linkham* stage was used to control the sample temperature. The excitation laser source used in this work was a diode-pumped solid-state (DPSS) continuous wave (CW) 532 nm laser with a maximum power of 24 mW measured at the stage. The excitation intensity was controlled by inserting the appropriate neutral-density (ND) filters. The spectral response of the entire system was determined by a calibrated halogen-tungsten light source.

The power range of the excitation laser applied in this work was between 6 mW and 24 mW. Since the excitation spot size was a few microns in diameter, the excitation intensities were from 76 kW/cm^2 to 320 kW/cm^2. This range of excitation intensities resulted in high carrier densities (> 10^{18} cm^{-3}) as demonstrated by Gundel *et al* [46]. Therefore, diffusion of the photo-generated carriers was limited by Auger recombination, hence the carrier profile was confined close to the illuminated surface area and beam absorption depth.

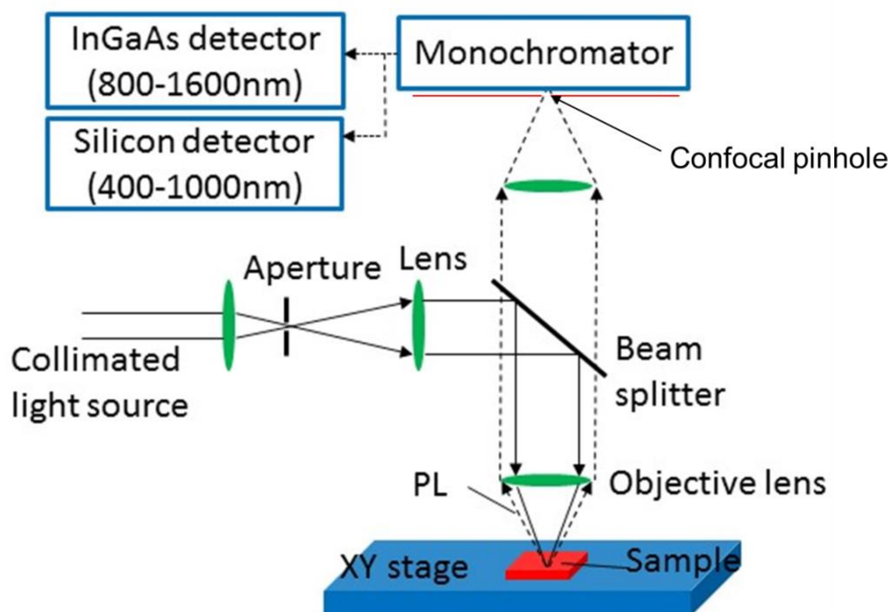

Figure 3-9 Schematic of the μ-PLS system

3.8 LASER SYSTEMS AT ANU

3.8.1 Excimer laser system

The excimer laser system (λ = 248 nm) used in this work (Chapter 4 and Chapter 7) is a *Coherent COMpexPro 110F* which uses a krypton-fluorine gas mixture as the lasing medium. Figure 3-10 depicts the configuration of the laser system and the temporal pulse profile at a 25-kV discharge voltage.

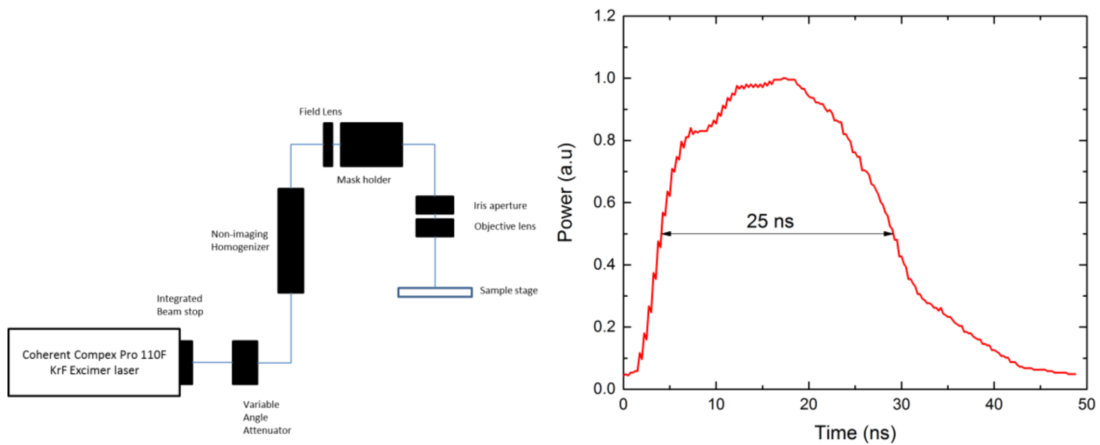

Figure 3-10 (Left) Schematic of the excimer laser system, and (Right) the temporal pulse profile measured at 25 kV discharge.

A maximum average power and pulse energy is $P_{avg,max}$ = 30 W, at a maximum pulse repetition frequency f_p = 100 Hz, and $E_{p,max}$ = 400 mJ respectively. As seen in Figure 3-10, the temporal pulse profile is similar to an asymmetric Gaussian function with about 25 ns full-width at half Maximum (FWHM) and approximately 40 ns total pulse width. The output pulse energy from the machine is set by controlling the discharge voltage from 19 to 30 kV. A variable angle attenuator enables further tuning of the pulse energy at the target plane. After passing through a non-imaging homogeniser, the beam has good uniformity, less than 5 % energy variation across the beam area. The beam is then delivered to a field lens with a long focal length to reduce beam divergence. A transmission mask also could be installed at this point to define the process features, size and shape. In this case a rectangular variable aperture was used, which is micrometre-controlled to produce a rectangular feature. Before the sample stage, another objective lens was inserted with an iris aperture to remove higher spatial frequencies. The end objective was fixed

without a galvanometer scanner, so the beam was directly incident to the stage, hence the process direction can be controlled only via the x-y stage transition. At this stage, sufficient and stable power readings were only possible with the available power meter when using a large area (500 × 500 μm^2) beam. Smaller features were then assumed to have an equivalent energy density, based on the good energy uniformity across the large area beam.

3.8.2 Green laser system

Figure 3-11 illustrates the configuration and arbitrary waveform generation function of the green laser system used in Chapter 6. A *Pyroflex 25* fibre laser system generates an infrared laser beam (λ = 1064 nm), with a maximum pulse energy of E_p = 500 μJ. This system allows users to adjust the pulse duration ($0 < \tau_p \leq 600$) and height in 1 ns resolution, so that is possible to generate arbitrary pulse shapes on demand (see also Figure 6-2). The pulse repetition rate is controlled by the external function generator up to 500 kHz. The infrared laser beam is then converted to the green laser beam (λ = 532 nm) via the frequency doubling crystal. After splitting the beam, the residual infrared beam is dumped, and the green laser beam is delivered to a variable angle attenuator for fine pulse energy tuning. A beam expander is inserted to match the focal plane of the beam to the sample stage height. A galvanometer scanner with an x-y gantry stage enables a more flexible process than the excimer laser system. However, the beam is not homogenized, so the spatial beam profile has Gaussian distribution with a 4σ diameter of about 16 μm on the target surface.

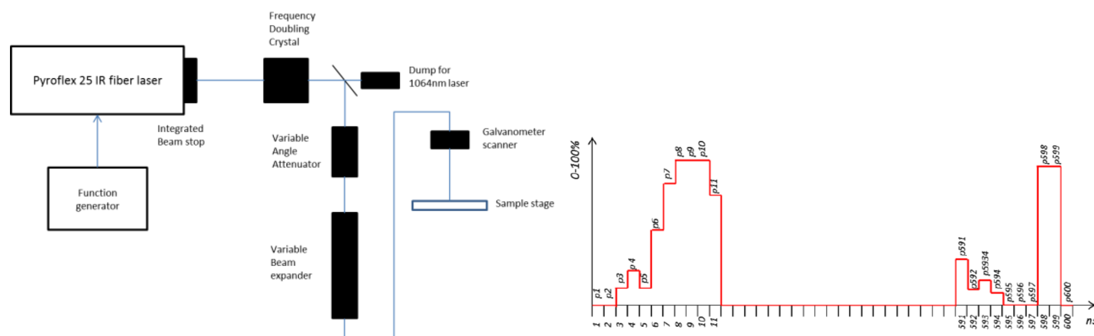

Figure 3-11 (Left) Schematic of the green laser system, and (Right) the demonstration of arbitrary waveform generation in 1 ns resolution.

3.9 SUMMARY AND IMPLICATIONS

This chapter provides general information on PLS characterization. PL spectra measured at low temperatures is proven to be a reliable method to accurately diagnose the band structure of silicon. BGN owing to heavy doping is clearly represented by the PL peak shifting toward longer wavelengths and broadening. Deep-level PL at the longer wavelength ranges (> 1200 nm), the so-called "D-lines," are closely related to the formation of defects/dislocation. In the literature, it was noted that D1/D2 lines stem from secondary defects or impurities around dislocations, whereas D3/D4 lines are an intrinsic feature of dislocations. Based on this fundamental principle, with the advantage of having highly resolving optical μ-PLS measurements, dopant distribution and recombination active locations across localized features are spatially investigated in the following chapters.

Chapter 4. Spatial characterization of laser-induced doping/damage in Si with different surface conditions

4.1 INTRODUCTION

It is well known that the laser process induces defects near the sample surface [76, 108, 148-152]. The impact of the defect is usually evaluated in terms of recombination properties using the conventional characterization methods introduced in 2.4.2 [90, 149, 153, 154]. Alternatively, the formation of laser-induced defects can be investigated directly using microscopic images, SEM or transmission electron microscopy (TEM) [76, 108, 148, 150, 152]. Microscopic visual inspection shows the spatial distribution of defects in localized features clearly, but it is not practical to use repetitive measurements to explore a wide range of laser parameters due to the extra sample preparations needed for imaging specimens. For example, the complex and sophisticated preparation steps required to fabricate cross-sectional specimens using focused ion beam (FIB) milling makes it difficult for TEM to be used as a repetitive characterization tool. In some cases, Yang etching [155] is also employed to delineate defects [108, 150].

This chapter illustrates that these laser-induced defects can be characterized spatially by μ-PLS without specific sample preparations. Using the advantage of high spatial resolution (down to 1 μm) and the easily repeated measurements of μ-PLS, the impact of various laser parameters was investigated by observing the defect/dislocation-related PL spectra at specific positions. These include the centre of the processed region, the boundary/edge of processed and unprocessed regions, and the boundary between two overlapped laser pulses, as shown in Figure 4-1. The impact of laser parameters on laser doping was also investigated by observing the doping peak (see 3.4 and 3.6).

This chapter begins with a study of laser damage from the PL spectra of laser-irradiated samples without the inclusion of dopants. This is then compared with the PL spectra of laser-doped samples to observe the level of doping and to determine where laser damage is most prevalent within the laser-doped regions. Lastly, we

study the effect of sample surface conditions on damage introduced via the laser process.

4.2 EXPERIMENTAL DETAILS

Two sets of samples were prepared: one set with polished surface conditions and the other set with relatively rough surface conditions. Polished surfaces were achieved via standard chemical-mechanical polish (CMP), prepared by the manufacturer. The rougher surfaces were formed by chemical etching in tetramethyl ammonium hydroxide (TMAH) solution for 10 minutes, which is typically employed to remove saw damage from as-cut wafers. The resultant surface conditions of the CMP and TMAH-etched substrates can be compared in the microscopic images in Figure 4-1. Apart from the surface condition, other properties of both substrates were kept consistent. Both sample substrates were phosphorus doped, n-type FZ silicon wafers with resistivity of around 6 Ω·cm, corresponding to a background doping level of around 7×10^{14} cm^{-3}. Prior to depositing the dopant precursor, both substrates were RCA cleaned to remove any precipitates. B155 Poly boron SOD from *Filmtronics* was then applied using a benchtop spinner at 2000 RPM for 50 seconds. The dopant source was subsequently baked at 90 ˚C for 20 minutes to remove solvents. A 248 nm KrF excimer laser with a homogeneous 320 × 320 μm^2 rectangular shaped beam was used, under nitrogen processing gas flow (to reduce oxidation and other particle contamination) at atmospheric pressure and room temperature. The laser irradiation melts a shallow layer (typically in the order of 1 µm or less), thus introducing dopants into the melted layer subsequent to recrystallization. A variety of single or multiple repeat pulses, up to 10, were employed with various fluences in the range of 1.5 to 4 J/cm2. Consecutive laser pulses were spaced by 300 µm to form an overlapped region about 20 µm wide. The samples were not passivated to avoid any impact of dielectric films on laser-processed silicon [108, 156].

The µ-PLS system employed in this study was a Horiba T64000 with a liquid-nitrogen-cooling cryostat to maintain the sample temperature at 79 K. The excitation source was a CW 532 nm DPSS laser (with an incident spot size down to about 1 µm diameter on the sample surface) using a 50× objective lens, and an excitation power

kept at approximately 6 mW for all measurements. The emitted PL signal was measured by a liquid-nitrogen cooled InGaAs detector. The spectral response of the entire system was determined with a calibrated tungsten-halogen lamp. Detailed information on the μ-PLS system is given in 3.7.

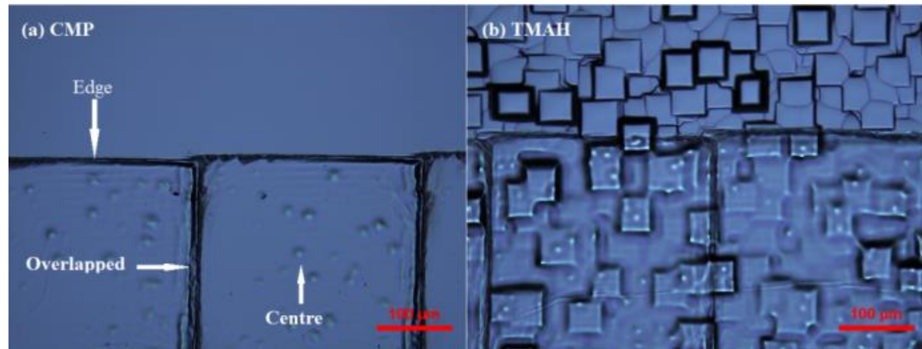

Figure 4-1 Microscopic images of laser-doped regions (4 J/cm2) on (a) CMP and (b) TMAH-etched substrates, indicating PLS measurement locations; the centre, the edge and the overlapped regions

4.3 PL SPECTRA OF EXCIMER LASER-DAMAGED SI

In order to assess the impact of damage induced via the laser doping process, it is useful to distinguish the PL signals observable due to damage and those due to doping. To achieve this, the defect-related PL signals were first observed from silicon substrates that had been processed by the excimer laser without inclusion of the dopant precursor but using laser parameters known to be compatible with doping. The range of doping inducible fluence is between 1.5 J/cm^2 and 4 J/cm^2 with repeat pulses of 1 ~ 10 (see Figure 4-4).

Figure 4-2 shows the normalized PL spectra of the excimer laser-processed samples measured at different positions within the laser-processed region. The plots also contain the PL spectra measured for the same substrate types, but prior to any laser processing; it is worth noting that in this case the observed signal was identical for both the CMP and TMAH samples and hence only one spectrum was plotted. Compared to the spectra of the unprocessed Si, most spectra of the laser-processed samples show specific local PL peaks at around 1230 nm and 1280 nm. These two PL peaks are quite small (in this case a log scale is used for the y-axis, while for later

plots a linear axis is used to better illustrate features present after laser doping) but are distinctive compared to the spectra observed on the unprocessed substrates.

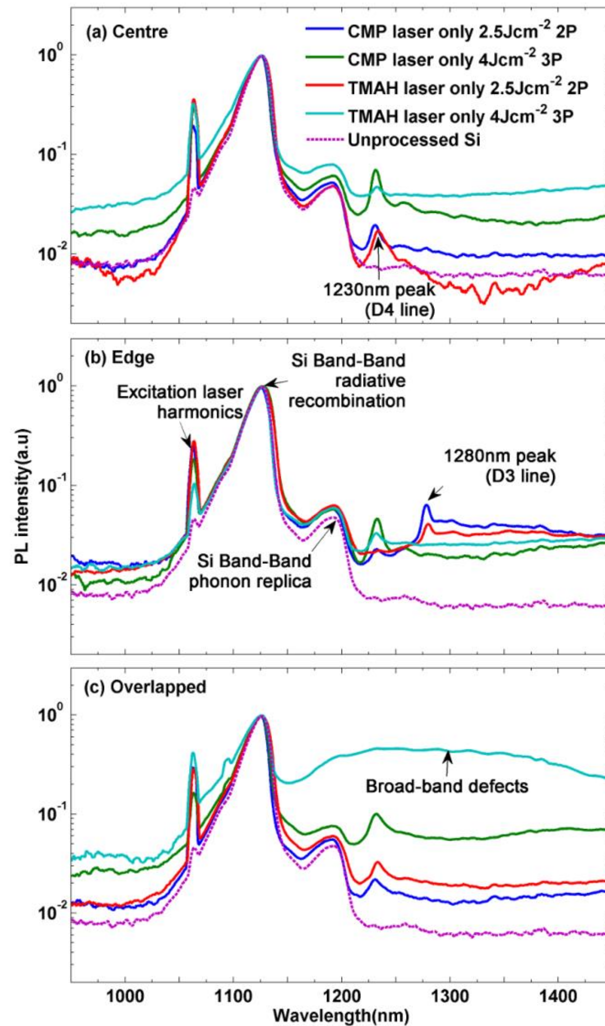

Figure 4-2 Normalized PL spectra measured on excimer laser-irradiated samples without a the inclusion of dopants at (a) the centre, (b) the edge, and (c) pulse overlapped regions, on both TMAH-etched and CMP substrates. Excitation is achieved with a 532 nm laser, and substrate temperature is 79 K.

The locations of these two PL peaks are close to the D4 and D3 lines which are emitted from intrinsic dislocations in the crystalline silicon and are particularly observable near liquid-nitrogen temperatures [51, 146]. The characteristic wavelength reported in the literature for the D4 line is consistent with our observed 1230 nm peak in Figure 4-2, whereas the characteristic wavelength corresponding to the D3 line is slightly lower than the value reported in the literature, which varies between 1290 nm and 1305 nm, depending on the relative position around

dislocation sites [146]. These luminescence peaks were not observable at all on unprocessed silicon; therefore, we can reasonably conclude that the two PL peaks at 1230 nm and 1280 nm observed in Figure 4-2, are emitted from dislocations caused by the laser irradiation. The fact that the other two deep-level lines, D1 and D2 — which are known to originate from secondary defects and impurities trapped by the strain field around dislocations [51] — were not observed. It suggests that either the laser irradiation (without the dopant) has created dislocations where such additional defects and impurities are not incorporated, or their concentrations are too low to emit corresponding PL peaks. Furthermore, the intensities and widths of the 1230 nm and 1280 nm peaks are low and narrow, so the density of dislocations is low unless employing high fluence. It is observed that the presence of both the 1230 nm and 1280 nm peaks are dependent upon laser parameters and the measurement location.

Table 4-1 summarizes the presence of specific 1230 nm (as ● in the table) and 1280 nm (as ○ in the table) peaks as well as the presence of a high level of broad PL band in the range of 1200 ~ 1500 nm (here referred to as broad-band defects, ◊ in the table), observed in the PL spectra of laser-damaged CMP and TMAH samples for a variety of typical laser parameters.

Flunence	**Pulse**														
	Centre					Edge					Overlapped				
CMP	1	2	3	5	10	1	2	3	5	10	1	2	3	5	10
1.5J/cm^2			●+○	●+○	●+○			N/A					N/A		
2 J/cm^2		●/○	●+○	●+○	●	○	○	○	○	○	●+○	●+○	●+○	●+○	●+○
2.5J/cm^2	●	●	●	●	●	○	●+○	●+○	●+○	●+○	●+○	●	●	●	●
3 J/cm^2	●	●	●	●	●	○	●+○	●+○	●+○	●	●+○	●	●	●	◊
4 J/cm^2	●	●	●	●	●	○	●	●	◊	◊	●	●	◊	◊	◊
TMAH															
1.5J/cm^2			●+○	●+○	●+○			N/A					N/A		
2 J/cm^2	○	●/○	●+○	●+○	●	○	○	○	○	○	●+○	●+○	●+○	●+○	●+○
2.5J/cm^2	●	●	●	●	●	○	○	○	●+○	●	●+○	●	●	●	◊
3 J/cm^2	●	●	●	●	●	○	●+○	●+○	●+○	◊	●	●	●	●	◊
4 J/cm^2	●	●	●	●	●	○	●	●	◊	◊	●	●	◊	◊	◊

The presence of both peaks in a pair indicated as ●+○

●: 1230nm peak ○: 1280nm peak ◊: Broad-band defects (1200 ~ 1500 nm)

Table 4-1 A qualitative indication of the presence of the defect-related 1230 nm/1280 nm PL peaks and broad-band defects in PL spectra of CMP and TMAH laser-processed (but undoped) samples for a range of laser fluence and pulse repeats, observed at centre, edge and overlapped laser pulse regions.

PL spectra corresponding to low fluences (1.5 J/cm^2) at edges and overlapped regions are excluded, since in these cases the laser process itself produced minimal or no visible impact on the wafer surface and therefore precise positioning of the excitation laser beam at the edge or overlapped regions was not possible. Note that the boundary of the processed region is only visible for fluences above 2.0 J/cm^2. However, positioning at the center of the region could more easily be achieved because of the relatively large beam size (320 × 320 μm^2); thus PL spectra corresponding to low fluence (1.5 J/cm^2) at centers are included.

With increasing fluence and repeat pulses the 1230 nm peak becomes evident, whereas the 1280 nm peak disappears. When lower fluence is applied, both the 1230 nm and 1280 nm peaks are observed, but the 1230 nm peak only is seen as fluence increases. Interestingly, PL spectra measured at the edge region, processed with a lower fluence or single pulse, show only the 1280 nm peak, unlike other regions where both PL peaks are present in a pair. Moreover, the edge and overlapped regions show a high level of broad PL band (1200 ~ 1500 nm) when the regions are processed with very high fluence (4 J/cm^2) and multiple pulses (> 3). When comparing the presence of those PL peaks on different surface conditions in Table 4-1, they are not very dependent on the surface conditions, apart from evidence of more broad PL band on the TMAH samples under high fluence irradiation.

4.4 PL SPECTRA OF EXCIMER LASER-DOPED SI

The observations of PL spectra relating to laser processing without the introduction of any dopant, as described in the preceding section, provides good evidence of the damage induced by the laser-induced melt and recrystallization process itself. However, most processes of interest involving a significant melt and recrystallization event at the substrate surface are accompanied by the introduction of dopants to form heavily doped n-type or p-type silicon. We therefore investigate doping and damage resulting from a laser doping process, observed via the PL spectra of laser-doped samples. The normalized PL spectra of a variety of laser-doped samples, as measured at the centre of the laser-doped region, are demonstrated in Figure 4-3. The spectrum observed for an unprocessed silicon sample is also plotted for comparison.

The first observation made was evidence of heavy doping via the local PL peak at around 1160 nm. This luminescence emission from heavily doped sub-surface layers is due to BGN, while the PL peak, at around 1130 nm, comes from the underlying silicon substrate. It is well known that a higher dopant or carrier concentration results in a reduction in the band-gap of silicon, resulting in radiative recombination at a lower energy (longer wavelength emission).

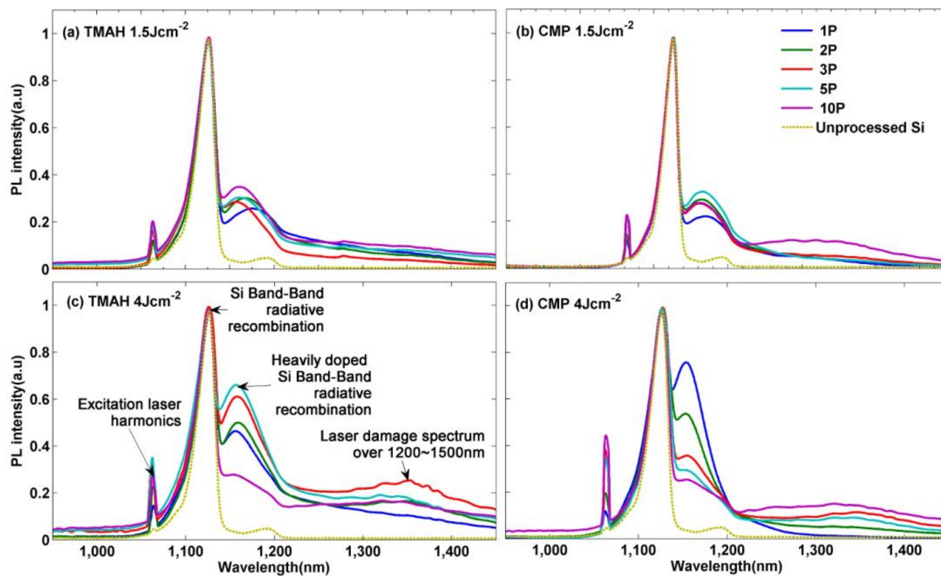

Figure 4-3 Normalized micro-PL spectra measured on excimer laser-doped samples with (a, b) 1.5J/cm2 or (c, d) 4J/cm2 at the centre regions on (a, c) TMAH-etched and (b, d) CMP substrates. Excitation is achieved with a 532nm laser, and substrate temperature is 79K.

For doping profiles which are not homogenous along the depth, for example a typical doping profile resulting from a tube diffusion or laser doping process, the degree of BGN also varies with depth and hence emission occurs over a range of wavelengths. Nonetheless, if the excitation irradiance is absorbed strongly near the substrate surface, as is the case for the 532 nm laser light, and if generated carriers and hence recombination is confined to the absorption zone, by using high intensity irradiance and hence ensuring Auger-limited carrier diffusion, then recombination in the most heavily doped region just below the surface dominates, and the emission spectra peak becomes a proxy for the surface dopant density. Therefore, we can estimate the relative degree of surface dopant density by observing the wavelength at

the local PL peak corresponding to the heavily doped layers (here referred to as the doping peak).

Figure 4-4 plots the wavelengths of the doping peaks and sheet resistances as a function of the number of repeat pulses for three fluences. The range of applied fluences has shown to yield a wide range of doping levels. The spectra were measured at the centre of the laser-doped regions on both TMAH-etched and CMP samples. Since the doping peak is broad, low and asymmetric, particularly at low fluence or very high fluence with multiple pulses, the PL peak wavelength is determined by taking the median of wavelengths having PL intensities larger than 99.5 % of the maximum value within 1140 nm and 1200 nm. By comparing Figure 4-4 (a, c) and (b, d), it is concluded that the surface condition does not greatly affect the resultant level of doping since the figures do not exhibit clear differences. Moreover, both samples show similar trends with both fluence and the number of repeat pulses.

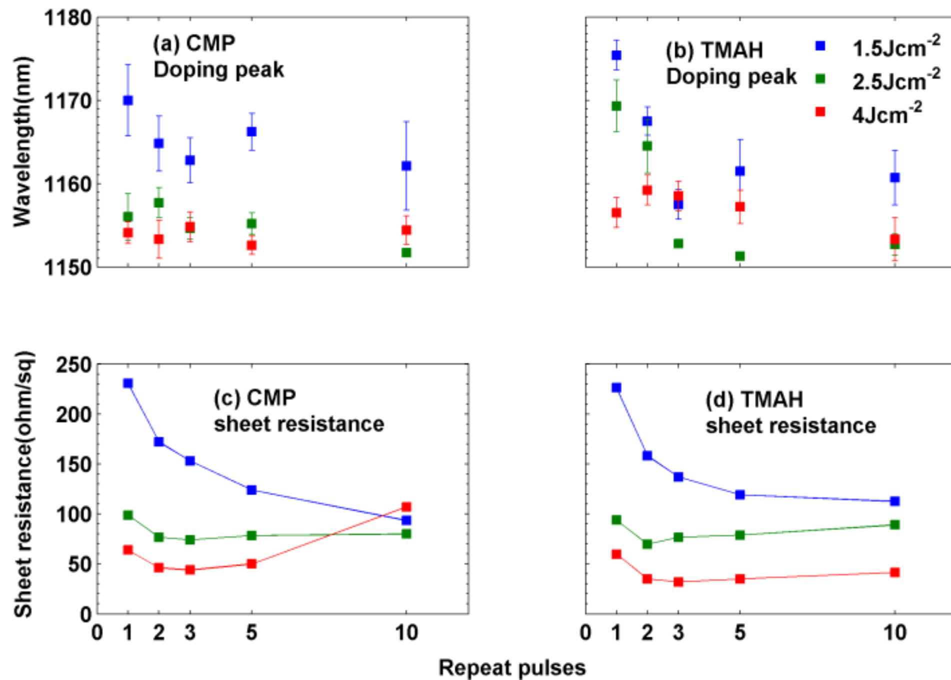

Figure 4-4 The wavelengths of the doping peaks and sheet resistances from laser-doped silicon substrates with (a, c) CMP surface and (b, d) TMAH-etched surface finish, as a function of number of repeat laser pulses and for a range of laser fluences, observed via μ-PLS measured at the centre of the laser-doped regions.

The total dose and depth of laser-doped samples is determined by the fluence and number of repeat pulses [39, 104]. The initial laser pulse melts the silicon sub-surface layer while simultaneously incorporating dopant atoms from the dopant precursor into the melt, and in particular for higher fluences removing or ablating some of or the entire dopant precursor films itself, prior to complete recrystallization. A higher fluence generally leads to more dopant atoms being introduced, but also to a larger melt depth and longer melt period and hence a deeper and flatter distribution of dopants within the recrystallised layer. As a result, at higher fluences we observe lower sheet resistance, owing both to the higher dose deeper doping, and a lower wavelength of the doping peak; the outcome of a lower surface dopant density associated with a deeper and flatter doping profile. Subsequent pulses typically introduce little or no additional dopant atoms for higher fluences (the dopant precursor being completely consumed or removed by the initial pulse e.g. for 2.5 J/cm^2 and 4 J/cm^2 in this experiment) but do introduce some additional dopants for lower fluences (1.5 J/cm^2 in this case).

The dominant mechanism associated with repeat pulses is the re-melt and re-distribution of the existing dopant atoms within the melt layer, similar to the effect of a traditional thermal 'drive-in' step and resulting in a doping profile characterised by both lower surface dopant density and greater depth [39, 104]. A deeper and flatter profile yields a lower sheet resistance, even for the same total dose, simply because carrier mobility increases with decreasing dopant density [157]. Hence it can be readily observed that subsequent pulses generally reduce sheet resistance while also reducing the wavelength of the doping peak.

Such a change is generally more evident after the second pulse than after subsequent pulses. This is the case first because the dopant precursor being partly or wholly removed by the first pulse means that more intense laser irradiation actually reaches the silicon surface for the second and subsequent pulses, and secondly because the actual diffusion of dopants within the molten-phase necessarily reduces with each pulse as the dopant gradient lowers. Additionally, it was observed that for higher fluences it appears that many repeat pulses may even result in material ablation and removal of doped silicon and hence a resultant increase in sheet resistance.

As shown earlier, damage and defects caused by laser processing are represented in the PL spectra in the wavelength range of 1200 ~ 1500 nm. A similar feature has been reported in laser-annealed silicon, which shows a multitude of broad bands at around 1360 nm [151], whereas the distinctive D1-D4 lines have been observed by other authors [147]. Moreover, a specific PL peak at around 1270 nm, showing similar features to dislocation-related PL peaks at a sub-grain boundary of a mc-Si, is also observed near the edge of laser-doped regions. Compared to the PL spectra in Figure 4-2, Figure 4-3 shows an elevated PL signal in this range without specific dislocation peaks being evident. In fact, dislocation-related PL peaks such as the D3 and D4 lines may still be present, but might be masked by the PL signal of continuous deep-levels formed by the laser doping process. It is additionally possible that the density of intrinsic dislocations (D3 and D4) might actually be suppressed due to the dislocation pinning effect of boron dopants in the laser-doped region, as reported previously for heavily doped silicon [158, 159].

This damage signal rises as higher fluences and a larger number of repeat pulses are applied. Moreover, the rise in the defect-related PL signal is observed to be greater at the edge of the doping or at overlapped regions, indicating the introduction of more severe damage at the silicon recrystallization boundaries (the interface between the laser melt region and surrounding region which remains solid throughout – noting that for the overlapping pulse regions the silicon has solidified and completely cooled between subsequent pulses). This difference in PL spectra among all measurement positions is only modest up to moderate fluence (< 3 J/cm^2) but becomes noteworthy at high fluence.

Figure 4-5 demonstrates the normalized PL spectra at the edge and overlapped laser-doped regions at 4 J/cm^2 for different numbers of repeat pulses and on different substrate surfaces. As seen in the figure, the magnitude of the PL signal corresponding to laser-induced damage at the edge and overlapped regions is much greater than observed for measurements taken at the centre of doped regions in Figure 4-3.

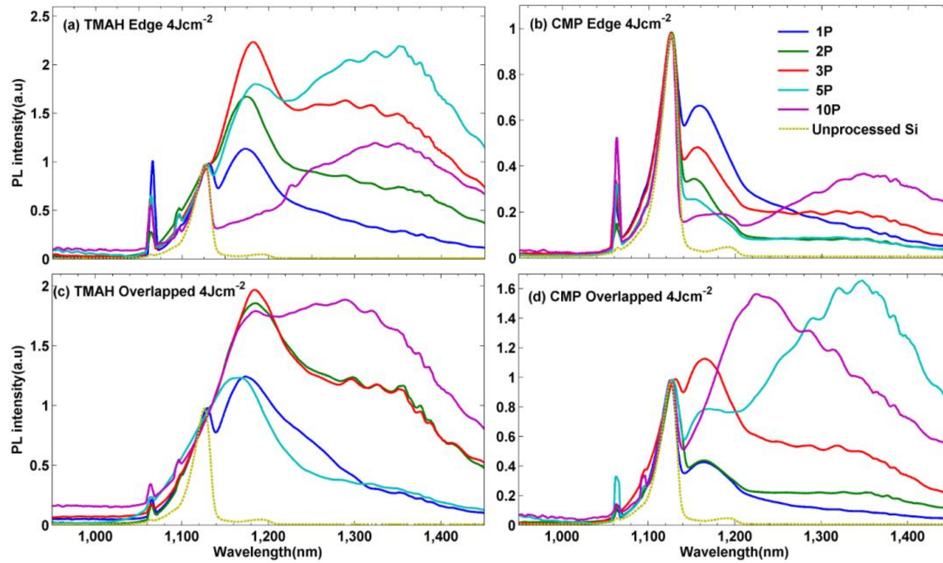

Figure 4-5 Normalized PL spectra measured on excimer laser-doped samples with (a, b) the edge and (c, d) the overlapped regions on (a, c) TMAH-etched and (b, d) CMP substrates. Excitation is achieved with a 532nm laser, and substrate temperature is 79K.

Furthermore, the PL peak due to the heavily doped region is not readily observable for some measurements, since it is masked by the dominant laser damage spectrum; indeed, the intrinsic silicon signal itself is barely recognisable for some of these samples, owing to the very high level of laser-induced damage and hence the dominance of defect-related recombination. It is difficult therefore to make any assessment of surface dopant density at those measurement positions (see 6.6). In addition, measurements at the edge/overlapped regions yielded more irregular PL spectra than measurements at the centre. Measurement at multiple points along the same edge or overlapped regions typically resulted in considerably different spectra for many samples, indicating that damage at the micron scale can be quite non-uniform for these interface regions. This observation is consistent with the visual appearance of these edge and overlapped regions at high magnification: they generally have a rough and pitted appearance in comparison to the centre of doped regions. On the other hand, the centre gives reasonably consistent PL spectra over different measurement points.

4.5 IMPACT OF SUBSTRATE SURFACE CONDITIONS ON LASER DOPING

The effect of the initial wafer surface conditions on the level of laser doping damage can be observed by comparing the PL spectra of Figure 4-3 (c) and (d) or Figure 4-5 (a) and (b). At low fluence (1.5 J/cm^2), measurements at the centre region of both surfaces emit similar PL spectra as shown in Figure 4-3 (a) and (b), with relatively low defect-related PL signals. However, the two different surfaces yield markedly different PL spectra at high fluence processing (4 J/cm^2), as seen both in Figure 4-3 (c) and (d) and in Figure 4-5. This difference is particularly clear for μ-PLS measurements taken at the edge of the doped region and at overlapped regions, with TMAH-etched surfaces resulting for all cases in a larger degree of defect-related recombination.

In order to demonstrate the impact of surface conditions more clearly, Figure 4-6 plots normalized PL spectra of laser-processed (both with and without the introduction of dopants) for both TMAH-etched and CMP substrates, measured at the centre, at the edge and at the overlapped pulse regions. It appears that less laser doping-related damage is induced on the smoother CMP surface, whereas more laser doping damage is induced on the rougher surface, although in both cases the damage created by the laser process is considerably greater than when processing takes place without dopant introduction. Moreover, the damage-related PL signal is amplified at the edge and the overlapped regions. Consequently, major electronic quality degradation in laser doping processes can be concluded to come from the pulse edge and overlapped regions.

In this study, all PL spectra were normalized to the silicon band-band PL peak, to clearly show specific features in the PL spectra relating to laser damage. However, the effect of laser damage is also reflected in the absolute measurement of the silicon band-band radiative recombination PL intensity, which is correlated to the minority carrier lifetime and hence the crystalline quality. Thus, provided that the excitation intensity, luminescent escape, and detection fraction is identical in each case, the measured band-band intensity of different samples can be directly compared.

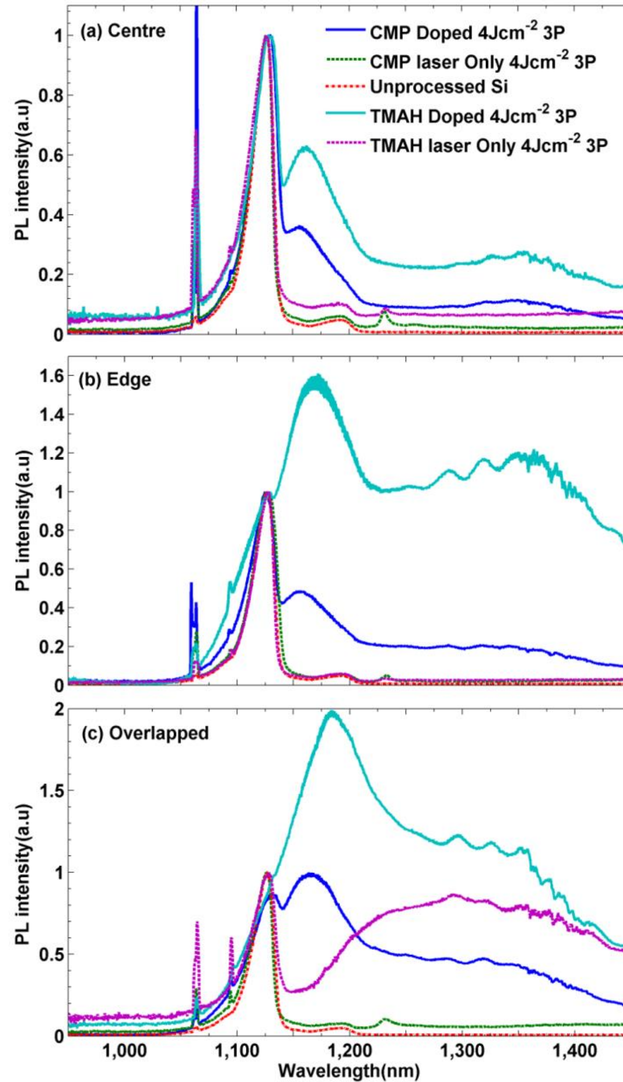

Figure 4-6 Normalized PL spectra measured on excimer laser-processed (without dopant precursor) samples with 4 J/cm^2 and 3 repeat pulses at (a) the centre, (b) the edge, and (c) pulse overlapped regions, and on both TMAH-etched and CMP substrates. Excitation is achieved with a 532nm laser, and substrate temperature is 79 K.

Figure 4-7 summarizes the silicon band-band luminescent peak intensity of the doped and undoped samples measured at the centre of the processed regions for CMP and TMAH-etched surface conditions. It is confirmed that higher fluences and a larger number of repeat pulses results in a lower absolute band-band PL emission, indicative of the crystalline degradation of the substrate. In addition, while this same trend is still observed, in the case of laser-doped substrates the band-band PL intensity is also lower. These observations are consistent with preceding observations and conclusions regarding, for example, the formation of more dislocations and

defects with a higher fluence/more repeat pulses, and the creation of greater broad defect-related PL band when dopants are introduced during laser processing.

It is, however, noted that this trend can only be seen in CMP samples, where the smooth surface results in minimal optical difference. The amount of excitation irradiance coupled into, and luminescent emission coupled out of the samples (and subsequently detected), are expected to be consistent at the smoother surface interface. In contrast, as seen in Figure 4-1, TMAH samples show a considerably varied surface before and after laser processing. As a result, significantly different amounts of light can be coupled into and out of the air and silicon interface when measured at different positions, since the irradiated region is small in comparison to the surface feature sizes. Therefore, the absolute PL intensity of TMAH-etched samples cannot be easily used to indicate crystalline quality.

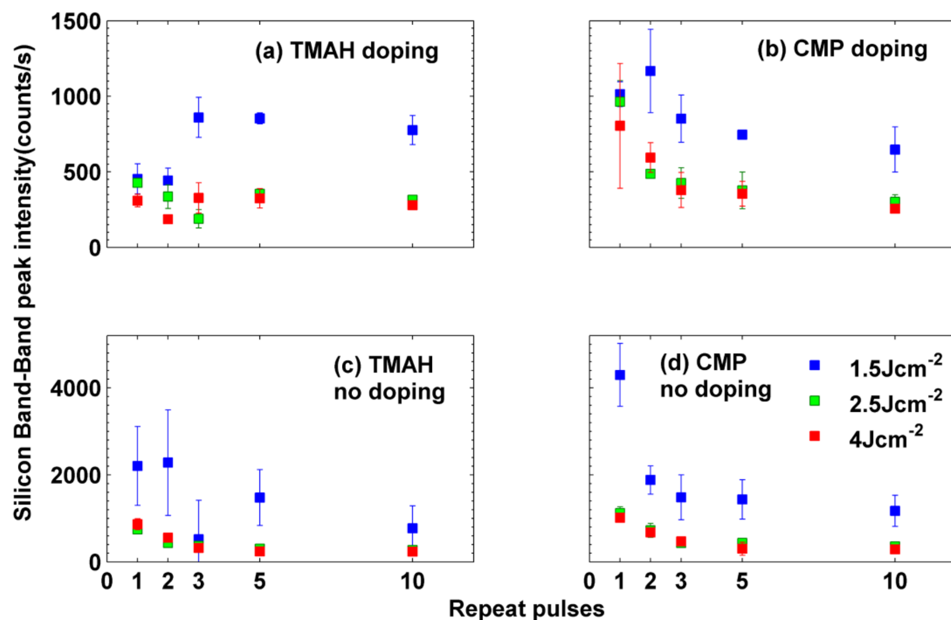

Figure 4-7 Silicon band-band PL peak intensities from (a, b) laser-doped and (c, d) laser-processed silicon substrates with CMP surface and TMAH-etched surface finish, as a function of number of repeat laser pulses and for a range of laser fluences, observed via μ-PLS measured at the centre of laser-doped regions.

4.6 CHAPTER SUMMARY

This chapter demonstrates that μ-PLS is capable of spatial characterization within the laser-processed region in micron-scale. High spatial resolution of μ-PLS measurement enables investigation of the impact of various laser parameters on the formation of dislocations and the doped layer as a function of position within the laser-processed region, and in particular at specific positions such as at the boundary/edge of processed and unprocessed regions.

The formation of dislocations in the laser-processed regions is confirmed by observing specific D4 and D3 lines in PL spectra measured in laser-irradiated samples without the inclusion of dopant atoms. As the laser fluence or number of repeat pulses increases, the D-lines increase and eventually form a broad defect-related PL band between 1200 nm and 1500 nm at very high fluence and repeat pulses. In addition, the presence of both D-lines is different according to the position of the processed region and applied laser fluence/repeat pulses. However, those specific D-lines are no longer observable after the introduction of dopants. The broad defect-related PL band, as observed from the high fluence laser-irradiated sample without dopants, is shown in the laser-doped sample regardless of laser fluence and number of repeat pulses. Moreover, a significantly higher level of defect-related PL band is identified at the edge of the processed region and the boundary between overlapped pulse regions, highlighting the significant role of the edges of the laser-doped region on the crystallographic degradation of laser doping.

The heavily laser-doped layers are characterized from the local PL peak at around 1160 nm (doping peak). The position of the doping peak can be attributed to BGN corresponding to different levels of sub-surface dopant density, which is achieved via laser doping with various combinations of laser fluence and repeat pulses.

In the comparisons of the defect-related PL spectra observed after laser processing between the two different substrate surface conditions (TMAH-etched and CMP), the lower defect-related PL spectra is observed with the smoother surface sample (CMP). This indicates that wafer surface preparation can be an important factor impacting on the quality of laser-doped silicon.

In the next chapter, the finding that the position of the doping peak is related to the surface dopant density/doping level is investigated in more detail. Utilizing this phenomenon, a new method for the quantification of dopant density in doped silicon layers is developed, based on the measured PL spectra only.

Chapter 5. Determination of dopant density profiles of thermally boron-diffused Si

5.1 INTRODUCTION

The previous chapter discovered that the relationship between the doping peak and sub-surface dopant density. Based on this feature, a new method is developed which is able to determine not only 1-D depth-wise doping profile, but also map dopant densities in lateral 2-D from the measured PL spectra alone. The method proposed in this chapter estimates the key defining parameters of doping profiles and thus reconstructs them mathematically for thermally boron-diffused silicon samples. Micron-resolution of μ-PLS measurements enables to perform 2-D mapping of those key parameters of locally boron-diffused features.

5.2 EXPERIMENTAL DETAILS

5.2.1 Sample preparation

The samples investigated in this work were produced via a two-step diffusion process; a quartz tube-furnace boron deposition step followed by a wet-chemical etch to remove the boron rich layer (BRL), and a subsequent high-temperature drive-in step. All samples were prepared on 100 Ω·cm high-resistivity n-type (100) orientation silicon wafers. Sample preparation is described in further detail by Yan and Cuevas in their investigation of BGN in heavily boron-doped silicon [71]. A total of 29 different doping profiles were used in this study, with surface dopant densities N_{surf} ranging from 3.34×10^{18} cm^{-3} to 1.56×10^{20} cm^{-3}, and with a range of different diffusion depths between 0.3 μm and 3.5 μm. A small selection of these doping profiles is depicted in Figure 5-1, all sample profiles being determined via calibrated ECV measurements.

Localized, heavily doped samples for the purpose of demonstrating dopant mapping via μ-PLS were also made using the same two-step diffusion process. Features were created via lithographically defined openings (30, 40 and 50 μm diameter), through a dielectric diffusion mask consisting of a thermally grown silicon

dioxide layer (~ 30 nm SiO_2) beneath a LPCVD stoichiometric silicon nitride layer (~ 80 nm Si_3N_4). Three different diffusion recipes were used on the same high-resistivity n-type silicon wafers – yielding light, moderate and heavy doping. The resultant profiles were measured via the ECV technique on additional 1 cm × 1 cm dielectric openings on each patterned wafer. All dielectric masks were subsequently removed in high concentration HF solution prior to measuring the PL spectra.

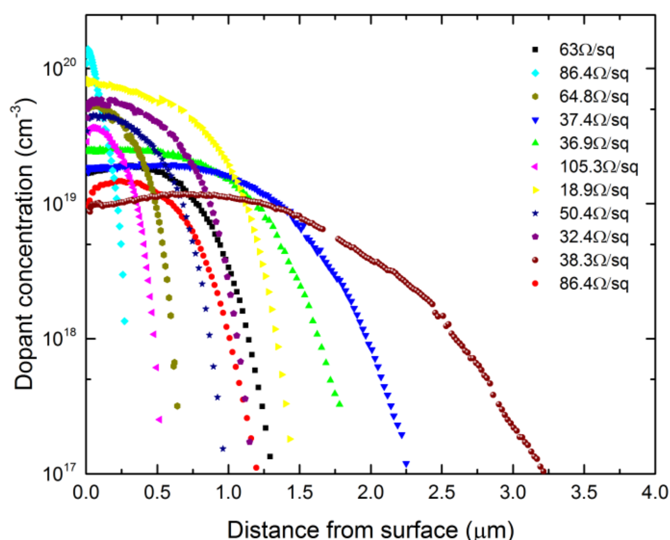

Figure 5-1 Doping profiles measured by ECV for a selection of thermally boron-diffused samples used for μ-PLS analysis, with corresponding measured sheet resistances

The μ-PLS system employed in this study is a *Horiba LabRAM* system equipped with confocal optics. For all measurements, the sample temperature was kept at 79 K via a liquid-nitrogen-cooled cryostat. The excitation source was a CW 532 nm DPSS laser, with an on-sample incident spot diameter of about 1 μm, achieved using a 50 × objective confocal lens whose numerical aperture is 0.55. The excitation power was kept at approximately 10.5 mW (equivalent to 134 kW/cm^2) for all measurements. The absorption depth of the excitation light at 79 K in silicon is around 4.7 μm, as calculated in 2.2.1, while Auger recombination at such high injection levels restricts carrier diffusion out of the excitation region and thus effectively limits the region of luminescence to a diameter of around 2 μm [46]. A liquid-nitrogen cooled InGaAs array detector captured the emitted PL spectra, with spectral resolution of 0.4 nm. The spectral response of the entire system was determined with a calibrated tungsten-halogen lamp. In order to compare the PL

spectra of different samples, the intensity of the PL spectra was normalized to the silicon band-band peak (~1130 nm) from the underlying lightly doped substrate. All samples measured in this work have reasonably planar surfaces formed via saw-damage etching in 25% TMAH solution, without any passivation films present.

Since the measured PL spectra contain the silicon substrate band-band peak as well as the doping peak of interest, subsequent to each measurement the PL spectra measured from undiffused control silicon was subtracted to more easily resolve the luminescence peak from the heavily doped layers (see 3.6). This is illustrated in Figure 5-2 (b). For the locally diffused samples, a 2-D scan mapping with 2 µm spatial resolution was conducted, and the full PL spectra measured and analysed at each point to characterize the locally doped regions in terms of N_{surf} and doping depth across the entire feature.

5.2.2 Key parameters defining the doping profile

For each doping profile three key profile characteristics were subsequently defined – the peak dopant density N_p, the peak dopant density position z_p, and the depth factor z_f. Since the dopant density for some samples varies considerably in the region immediately below the surface, the surface dopant density N_{surf} was also defined by averaging the dopant densities within 50 nm from the surface. The depth factor z_f was defined as employed in the PC1D simulator [160] by fitting a complementary error function (ERFC) or a Gaussian function to these profiles. This was possible since the two-step diffusion process results in a doping profile that can be approximated either by ERFC or Gaussian function, depending upon the process temperature and time of each step, and whether the process can thus be characterized as either a finite or infinite source diffusion [161]. The two functions described by equations (5.1) and (5.2) respectively, for a dopant density N at depth z, can each be defined by a peak concentration N_p, the depth at which that peak concentration occurs z_p, and a depth factor z_f.

$$N(z) = N_p \left\{ 1 - erf\left[\frac{|z - z_p|}{z_f} \right] \right\} : \text{ERFC} \quad (5.1)$$

$$N(z) = N_p \, exp\left[\frac{-\left(z - z_p\right)^2}{z_f^2} \right] : \text{Gaussian function} \quad (5.2)$$

5.3 ESTIMATING KEY PARAMETERS OF DOPING PROFILES

5.3.1 Relationship between N_{surf} and doping peak wavelength

Measured PL spectra, subtracted PL spectra showing only components from the heavily doped layers, and the corresponding doping profiles measured via ECV, of a selection of samples are depicted in Figure 5-2 (a), (b) and (c), respectively. Figure 5-2 (a) clearly shows two distinct PL peaks, at around 1130 nm and 1160 nm, corresponding to the radiative recombination of the underlying silicon substrate (Si BB) and the recombination in the heavily doped silicon layer (doping peak), respectively. The spectrum measured from an undiffused sample is also included for comparison. This spectrum is consistent for any undiffused silicon sample and additionally represents the emission spectrum from the excited substrate region immediately below the diffused layer in our samples.

Since the doping profiles are not homogenous with depth, the detected PL signal is a weighted sum over the individual spectra emitted from the varying doping concentrations, resulting in a broadening of the peak. Due to the fact that the excitation irradiance is absorbed most strongly near the sample surface, and the high intensity incident irradiation ensures an Auger-dominated carrier lifetime in the underlying substrate, the generation and recombination of carriers is confined near the front surface. Furthermore, emissions from nearer the front surface have a higher probability of falling within the detection angle of the detector. As a result, PL from recombination just below the surface, in the region of the heaviest doping, dominates over PL from further below the surface. Therefore, the wavelength of the doping peak can be regarded as a proxy for the surface dopant density. To more clearly resolve the doping peak, particularly useful for light and/or shallow doped layers such as sample 6, the normalized PL spectra of an undiffused silicon is subtracted and identify the wavelength of the doping peak.

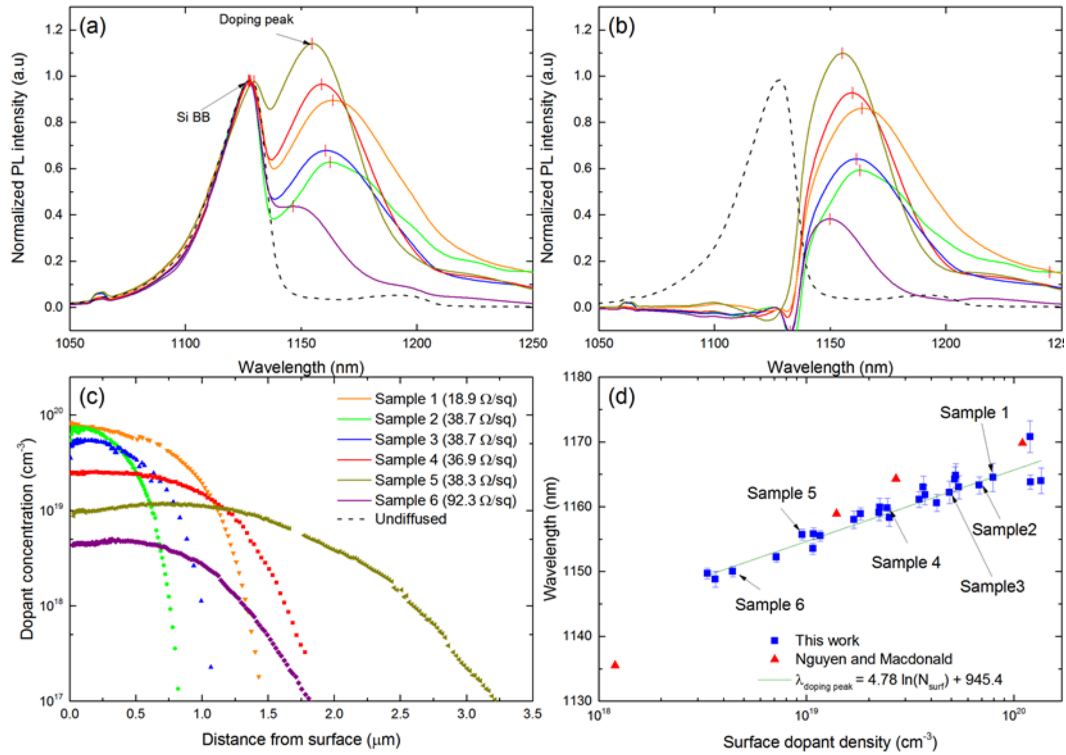

Figure 5-2 (a) Normalized PL spectra of a selection of boron-diffused samples with different doping profiles, measured with a 532 nm laser at 79 K. (b) Modified PL spectra obtained by subtracting the PL spectra of undiffused Si (c) The corresponding doping profiles with sheet resistances. (d) Measured wavelengths of the doping peaks as a function of N_{surf} for all samples, along with Nguyen and Macdonald's results [143] measured from homogeneously heavily boron-doped silicon.

The hypothesis that the wavelength of the doping peak is a proxy for the surface dopant density is verified in Figure 5-2 (d). For all samples, the wavelength corresponding to the doping peak was plotted as a function of N_{surf}. Error bars indicate the range of wavelengths having PL intensities larger than 99.5 % of the maximum doping peak PL intensity, and thus represent the uncertainty in determining the exact location of the doping peak. Nguyen and Macdonald's results [143], measured under similar conditions on homogeneously heavily boron-doped silicon wafers, also support our conclusion by showing close agreement with our measured values. Our data clearly reveals that the wavelength of the doping peak increases with increasing N_{surf}, displaying a consistent linear relationship on a semi-log plot over the range of interest. Thus, it was able to establish a simple 'calibration curve' for estimating N_{surf} from the wavelength of the doping peak. The relationship, which can subsequently be applied to any boron-diffused surfaces if PLS measurements are taken under similar conditions, is also shown in Figure 5-2 (d), and is described by equation (5.3).

$$\lambda_{doping\,peak} = (4.78 \pm 0.25)\ \ln(N_{surf}) + (945.4\ \pm 10.9) \qquad (5.3)$$

It was observed that the amount of peak shifting towards a longer wavelength does not match what might be anticipated from the simple application of theoretical BGN models, thus serving to highlight the complexity of the PL spectra modification which occurs with heavy doping. Based on Schenk's BGN model [72], when the dopant density increases from ~ 3×10^{18} cm^{-3} to ~ 1×10^{20} cm^{-3}, a theoretical band-gap shrinkage of around 60 meV occurs, whereas the peak shifting observed results in an apparent narrowing of only about 20 meV ($\Delta\lambda$ ~ 20 nm). Much less peak shifting was observed than is predicted by the BGN model, due to the counter influence of the degenerate effect which occurs in silicon at very high doping, as discussed in 3.4. Increasing the dopant density obviously causes more BGN, resulting in the peak shifting towards a longer wavelength. However, in degenerate silicon, the Fermi level E_F moves into the valence band (for p-type), not only shifting the spectra to a shorter wavelength (higher energy), but also broadening all PL spectrum. This broadening effect of degenerate silicon is also observable in Figure 5-2 (b), where the width of the doping peak is observed to increase with N_{surf}. Therefore, since most of the samples investigated in this work experience the competing influences of BGN and the degenerate effects, a separate study would be required to apply a theoretical fit to this data. This work will consequently rely upon the empirical relationship established here for the further analysis of doped features.

5.3.2 Relationship between z_f and doping peak intensity

The previous section has established that the position of the doping peak corresponds directly to the surface dopant density, yet it was also observed in Figure 5-2 (b) that for samples the relative intensity of the doping peak varies considerably with the profile depth. The doping peak corresponds to emissions from the heavily doped sub-surface region while the silicon band-band PL peak corresponds to emissions from the underlying substrate. The ratio of these intensities therefore reflects how much emission originates from the heavily doped layer compared to the underlying substrate. Since the depth of the excitation region is largely fixed according to the absorption depth of the excitation wavelength, this ratio could

therefore represent a measure of the depth of the heavily doped layer. Furthermore, the doped layer has a smooth transition between high and low doping, rather than a step change, and so rather than defining a simple doped layer depth we instead apply a commonly used depth metric, the depth factor z_f, for doped layers.

In order to find values of z_f and determine which function gives better fit to the measured ECV curves, all measured doping profiles of the investigated samples were iteratively fitted to both equations (5.1) and (5.2) to find z_f, which gives the minimum residuals between the measured data and the modelled functions. Using the optimal values of z_f for each function, the coefficient of determination R^2 of both two functions was calculated for all samples in Figure 5-3.

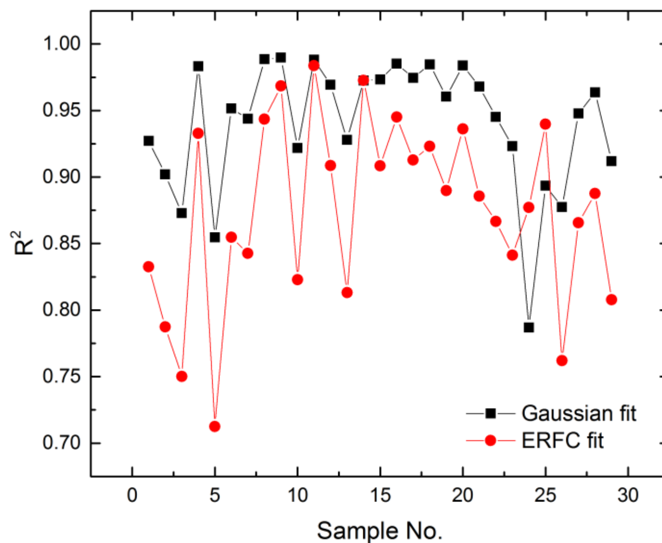

Figure 5-3 The coefficient of determination R^2 of two modelled functions (Gaussian and ERFC) for thermally boron-diffused samples. An R^2 of 1 indicates that the modelled functions perfectly fit the measured points.

As can be seen in the figure, most samples show a better fit to the Gaussian function than the ERFC, therefore z_f was fitted from the Gaussian function for all samples and an attempt was made to correlate this value with the normalized PL intensity of the doping peak. The Gaussian fit was consistent with expectations, given that the boron source glass was removed prior to the final thermal drive-in process in each case, meaning the dopant source was finite. A consistent fit between the doping peak PL intensity and depth factor means that we can use the PL spectral analysis to not only estimate the diffusion depth, but also reconstruct the doping

profile based on the relationship already established for the surface dopant density, assuming the profile follows a Gaussian shape. It was also observed that the reconstructed profile cannot include the term z_p, which is required for a profile with maximum dopant concentration occurring at a position considerably below the surface, as there is currently no reliable means of extracting the z_p component from the PL spectra analysis.

Figure 5-4 (a) plots the normalized PL intensity of the doping peak versus the depth factor for all samples. Generally speaking, the doping peak PL intensity increases monotonically with the diffused layer depth, as anticipated from theoretical considerations. However, it is evident from this data set that there is quite a wide spread in the depth factor at similar levels of doping peak PL intensity. In addition, lightly doped samples ($N_{surf} < 1 \times 10^{19}$ cm^{-3}) show a much larger discrepancy compared to the other samples. For example, in Figure 5-2, sample 6 shows a relatively deep profile compared to the other samples, whilst having the lowest doping peak PL intensity.

As discussed in 2.2.3, incomplete dopant ionization is significant for lightly doped samples ($N_{surf} < 1 \times 10^{19}$ cm^{-3}), and it is also more pronounced at the lower temperatures at which our PLS measurements occur. The absolute PL intensity for the heavily diffused layer is related to the ionized dopant density, since the PL intensity is proportional to the p-n product or in our case ~ $(N_A + \Delta n) \times \Delta n$, where N_A is the ionized dopant density and Δn is the excess carrier density [162]. As the PL spectra of diffused layers are primarily influenced by N_{surf}, any sample where significant incomplete ionization occurs under PLS measurement conditions will exhibit an overall reduced PL intensity at those wavelengths corresponding to the doping-induced BGN, compared to that which might be anticipated by consideration of the measured N_{surf} alone, at room temperature. The reduction in PL intensity will approximately correspond to the fraction of non-ionization which occurs near the surface during the PLS measurement conditions. This interpretation is supported by comparing samples 1, 4 and 6 in Figure 5-2. Although all samples have a similar profile depth, sample 6 shows a much lower doping peak PL intensity than the other two samples, since according to our calculations in 2.2.3, sample 6 has only about 46% of the dopants activated near the surface at 79 K.. Therefore, it is necessary to

consider the effect of incomplete ionization, calculated for each measured N_{surf}, on the PL intensity when correlating the depth factor to the PL intensity.

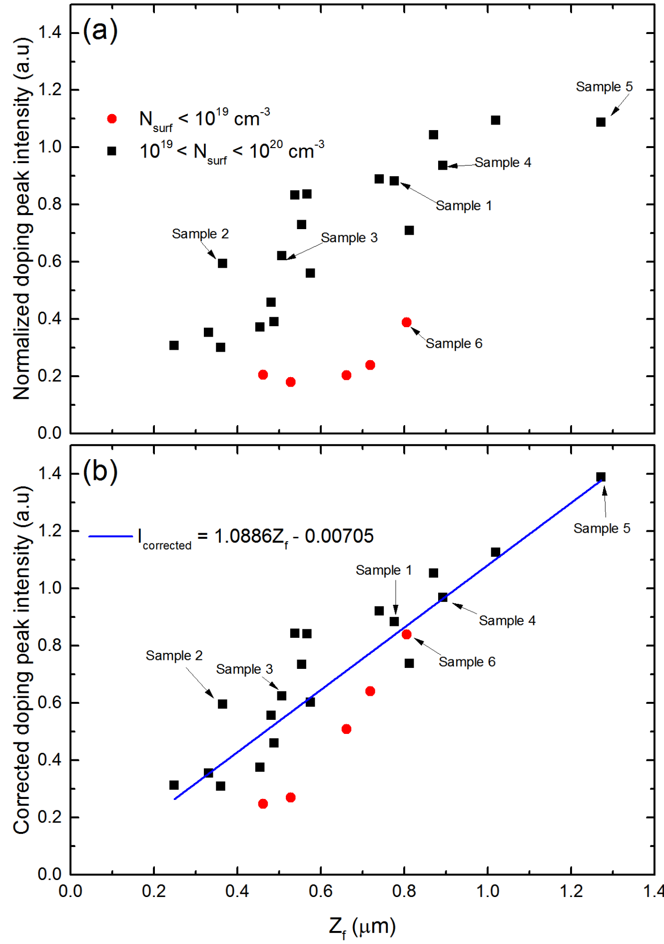

Figure 5-4 Normalized PL intensity of the doping peak as a function of depth factor, (a) without any correction, and (b) including a correction for the effect of incomplete ionization on PL intensity. Representative samples shown in Figure 5-2 are also labelled accordingly.

Figure 5-4 (b) again plots the normalized PL intensity of doping peak against depth factor, but with a simple division of the raw PL intensity by the fraction of ionization for each sample. The result shows an improved linear relationship between the doping peak PL intensity and the depth factor across all sample types, compared to Figure 5-4 (a). In particular, the measurements for the lightly doped samples now follow the main linear trend more closely. However, there is still quite a wide spread, most likely due to uncertainty associated with variable excess carrier density Δn among samples, leading to an unpredictable p-n product, and also due to non-ionisation fractions which are not fixed for any given sample but rather vary with

depth. Meanwhile, an accurate estimation of the value of Δn is very difficult since it not only depends on the generation profile (excitation intensity), but also on the electronic properties of the substrate, diffused layer and surface. Particularly, the unpassivated surface conditions incur a significant change in Δn near the surface, so that shallower profiles are more heavily influenced by surface conditions. As a result, individual samples would have a different value of Δn even under the same excitation conditions, which in turn influences the relative PL intensity of the doping peak and the substrate band-band peak. Therefore, if it is possible to estimate an accurate value of Δn for each individual sample, the more precise depth factor can be deduced. Nonetheless, the simple linear calibration curve between the corrected PL intensity of doping peak and the depth factor is established here for the remainder of our work (see Figure 5-4 (b) and equation (5.4)), in order to approximately reconstruct the doping profiles from PLS measurements.

$$I_{corrected} = (1.0886 \pm 0.128)\, Z_f - (0.00705 \pm 0.08562) \qquad (5.4)$$

This calibration curve is also valid only when the PLS measurement is conducted under conditions similar to those stated in this chapter.

5.4 APPLICATION TO LOCALLY DIFFUSED SAMPLES

5.4.1 Reconstructing doping profiles

In this section, the validity of this characterization method is examined by reconstructing doping profiles of separately made locally diffused samples based on μ-PLS measurements alone. The process of reconstructing profiles proceeds as follows:

1. Find N_{surf} from the wavelength of the doping peak $\lambda_{doping\ peak}$, based on equation (5.5) (rearranging equation (5.3) in terms of $\lambda_{doping\ peak}$)

$$N_{surf} = exp\left(\frac{\lambda_{doping\ peak} - 945.4}{4.78}\right) \qquad (5.5)$$

2. Find the fraction of ionization of the estimated N_{surf} obtained from step.1 at 79 K.
3. Measure the raw normalized PL intensity of the doping peak and divide it by the fraction of ionization obtained from step. 2
4. Find z_f from the corrected PL intensity $I_{corrected}$ from step.3, based on equation (5.6) (rearranging equation (5.4) in terms of $I_{corrected}$)

$$z_f = \frac{I_{corrected} + 0.00705}{1.0886} \tag{5.6}$$

Since there is no reliable way to find N_p and z_p from this µ-PLS analysis, and typically N_p is close to N_{surf}, set $N_p = N_{surf}$ and $z_p = 0$ in equation (5.2) and substituted all estimated N_{surf} and z_f in the simplified equation (5.7).

$$N(z) = N_{surf} exp\left(\frac{-z^2}{z_f^2}\right) \tag{5.7}$$

Figure 5-5 plots the normalized and subtracted PL spectra of locally diffused samples with the corresponding doping profiles, measured from large-area regions uniformly diffused through 1 cm × 1 cm dielectric openings. Three different profiles were prepared for light (labelled as LB1 in Figure 5-5), moderate (LB2) and heavy (LB3) doping cases, showing distinct N_{surf} and diffusion depths. The corresponding 4pp measured sheet resistances are 353, 60 and 24 Ω/sq, respectively. All measured values and µ-PLS estimated values are summarized in Table 5-1.

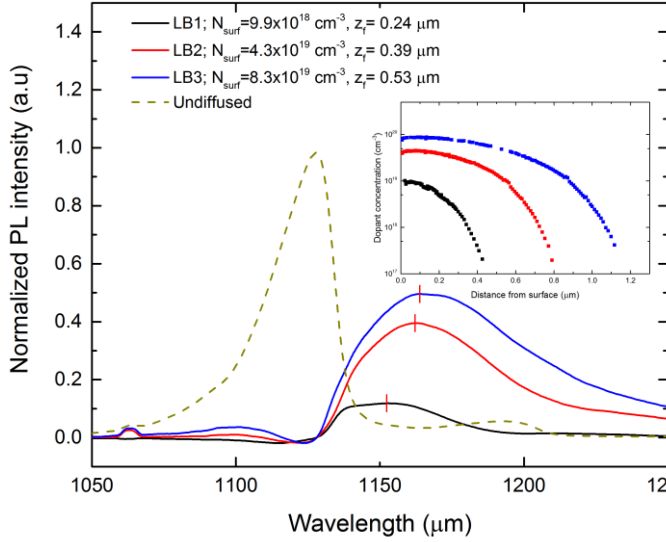

Figure 5-5 Normalized and subtracted PL spectra of locally diffused samples, labelled as LB1-3 with N_{surf} and z_f , with a 532 nm excitation laser at 79 K. The corresponding profiles are shown in the inset.

	LB1	**LB2**	**LB3**
$\lambda_{\text{doping peak}}$	1156	1162	1165
PLS estimated N_{surf} (cm^{-3})	1.4×10^{19}	4.8×10^{19}	8.9×10^{19}
ECV measured N_{surf} (cm^{-3})	9.9×10^{18}	4.3×10^{19}	8.8×10^{19}
PLS estimated z_f (μm)	0.14	0.37	0.47
ECV measured z_f (μm)	0.24	0.39	0.53
PLS estimated R_{sh} (Ω/sq)	426.3	62.5	26.6
4pp measured R_{sh} (Ω/sq)	353.4	60.5	24.2

Table 5-1 Comparison of ECV measured and μ-PLS estimated values

Based on the measured profiles, we would expect three different wavelengths and PL intensities of the doping peaks from the PL spectra, as confirmed in Figure 5-5. The wavelengths of the doping peaks for LB1 ~ 3 samples are about 1156, 1162 and 1165 nm, respectively. Based on equation (5.5), the corresponding N_{surf} are approximately 1.4×10^{19}, 4.8×10^{19} and 8.9×10^{19} cm^{-3} and show close agreement to the measured values. In addition, the normalized PL intensities of the doping peak for each sample are about 0.12, 0.4 and 0.5, respectively. Using equation (5.6) after

considering the impact of incomplete ionization of the dopants on the raw PL intensity of the doping peak, values of z_f are estimated to be about 0.14, 0.37 and 0.47 μm. Thus, from PLS measurements alone, we can reconstruct the doping profiles of these diffused samples, based on our calculated values for N_{surf} and z_f . The value of z_p is assumed to be zero. Substituting all parameters in equation (5.7), the reconstructed doping profiles are plotted in Figure 5-6, with the corresponding calculated sheet resistances. Although the reconstructed curves do not perfectly match the measured ECV curves, particularly for the very lightly doped sample, the agreement is nevertheless reasonable.

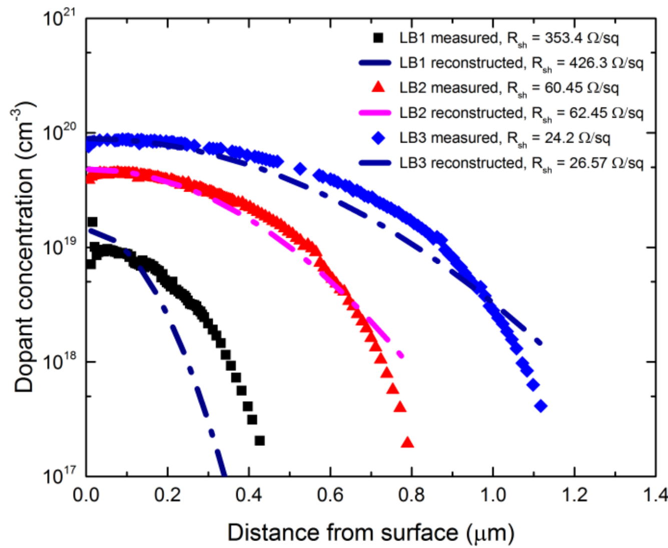

Figure 5-6 The measured and reconstructed doping profiles, used for locally diffused samples (LB1 – 3), with corresponding sheet resistances.

5.4.2 Mapping of N_{surf} and z_f

We conducted 2-D mappings of N_{surf} (Figure 5-7) and z_f (Figure 5-8) with 2 μm spatial resolution over locally diffused regions through lithographically-defined 30, 40 and 50 μm diameter circular openings on dielectric masks, by measuring and analysing PL spectra at each point. Comparing the images row by row in each figure allows us to observe the effect of different profiles for LB1 ~ 3, while the effect of the mask size can be seen by comparing column by column.

Once again it is possible to clearly observe three values of N_{surf} for each profile (Figure 5-7), at about 1.2×10^{19}, 4.8×10^{19} and 9×10^{19} cm^{-3}, respectively. In

addition, these samples show good uniformity over the diffusion area, regardless of the size of the dielectric mask openings and also exhibit distinct and sharp edges. This is to be expected for a diffusion that occurs into a region which has itself been created by a well-defined mask edge and serves to demonstrate the powerful capability of accurate 2-D surface dopant density mapping via this μ-PLS method. Interestingly, the dopant density is markedly lower over a distance of a few microns from one edge (particularly evident for the more heavily doped samples), and it is attributed to gas-flow dynamics associated with the deposition of the boron-rich glass during the tube furnace diffusion process.

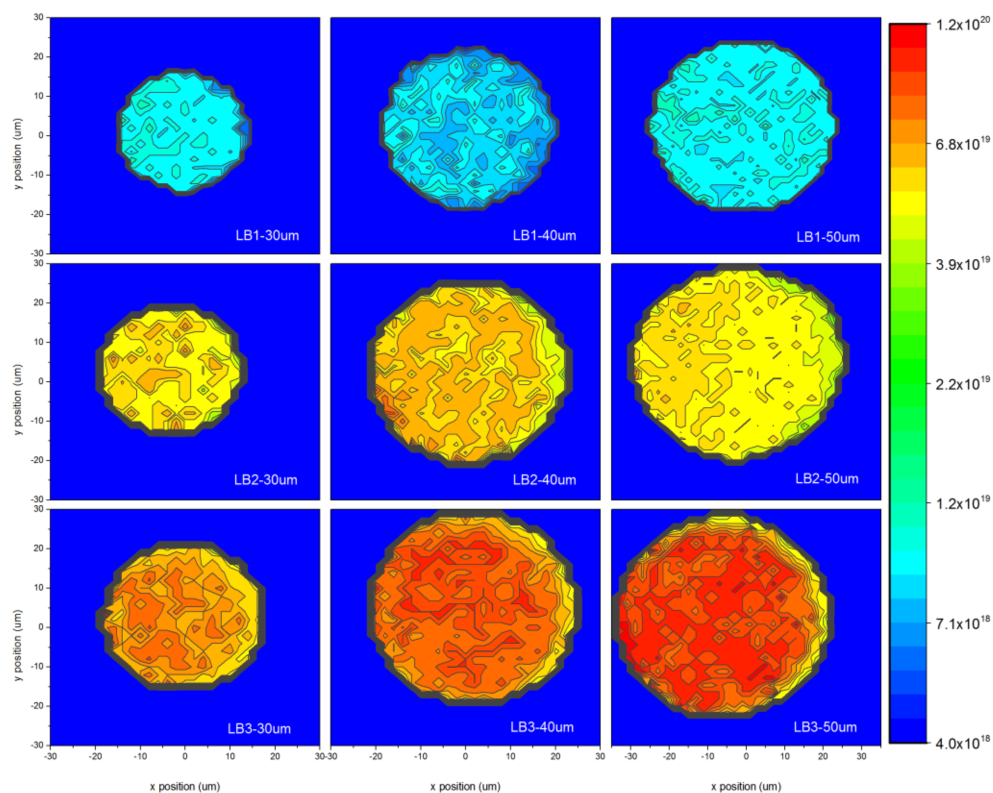

Figure 5-7 2-D scanned maps of N_{surf}, for locally diffused samples through 30, 40 and 50 μm dielectric mask openings.

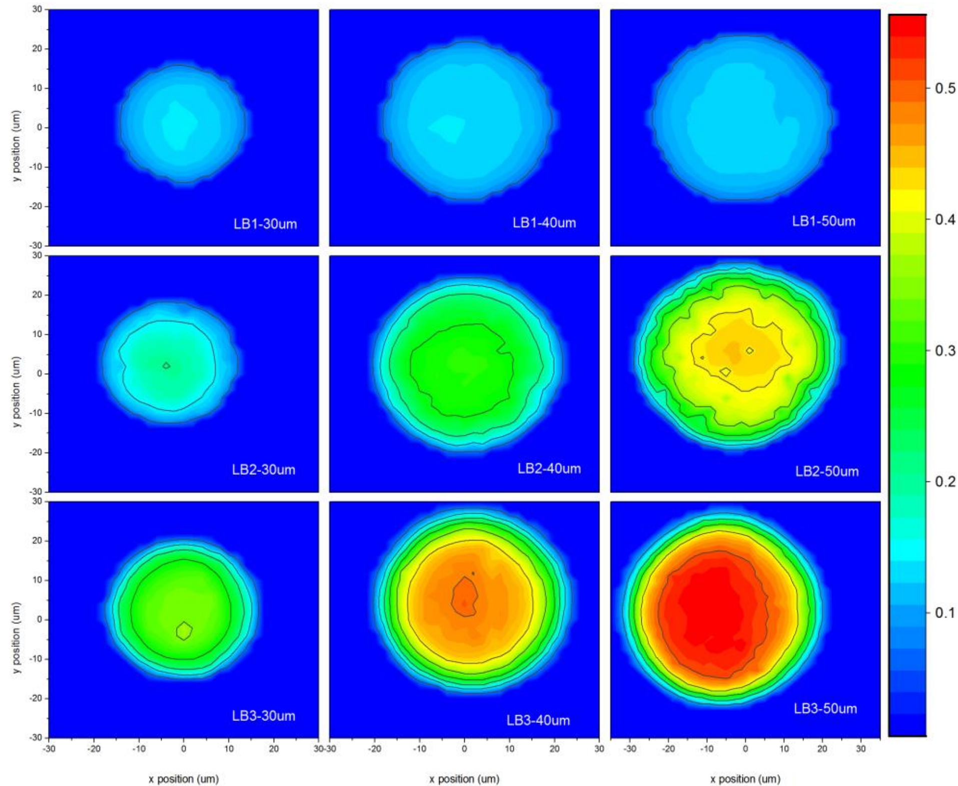

Figure 5-8 2-D scanned maps of z_f, for locally diffused samples through 30, 40 and 50 µm dielectric mask openings.

In contrast to our observation of uniform surface dopant density, the maps of the calculated depth factor in Figure 5-8 show a notable pattern. When comparing light, moderate and heavy diffusions, the mapped depth factor generally increases as expected from the ECV profile measurements, and at the centre of the larger (50 µm diameter) features does give a reliable measure of diffusion depth. However, an unexpected and considerable variation in the implied depth factor across the region of the masked diffusions is observed. A decreasing depth factor value is evident near the edges of the diffused areas. This could, in principle, be due to the dopant diffusion process itself, which produces some lateral and diagonal movement of dopants into regions around the perimeter of the masked region. However, the extent of the lateral variation observed, extending some 10 µm from the edge of the features, is inconsistent with impurity diffusion processes. Hence this observation is most likely a measurement artefact, in particular from lateral carrier diffusion, which results in a larger than anticipated 'detection volume' from which luminescence is detected. This results in a carrier smearing effect, where the intensity of the detected

PL spectra can be influenced by the undiffused region surrounding the heavily doped features. Although the measurement conditions, particularly the high excitation power, have been chosen to restrict the carrier diffusion length and confine the detection volume as much as possible, the precise dimensions of the detection volume are difficult to estimate, due to our limited knowledge of Auger recombination rates and carrier mobilities at these low temperatures. Nevertheless, this observation suggests that carrier smearing currently places a limit on the accuracy of this approach in determining the doping depth for small features. However, our approach for mapping the surface dopant density is not limited in the same manner, since it depends only on the position of the doping peak, rather than its PL intensity.

To further investigate the effect of carrier smearing on diffusion depth profiling, we measured and analysed PL spectra using different excitation intensities from 5.8 to 25 mW (equivalent to 74 to 320 kW/cm^2). This range of excitation intensities results in different injection levels and therefore different Auger recombination-limited detection volumes. This should in turn result in a difference in the carrier smearing effect and hence a difference in the implied diffusion depth profile near the edge of heavily diffused features. Figure 5-9 (a) plots the normalized PL intensity of the doping peak of a horizontal section across 2-D maps of the LB3-40 μm sample, for the three different excitation intensities. Lower excitation intensity increases the relative doping peak PL intensity due to different dependence of the p-n product on excitation intensity for the heavily diffused and lightly doped substrate layers: the undiffused layers respond to Δn quadratically, while the diffused layers respond to Δn linearly. However, the lateral carrier diffusion length does not appear to change significantly under this variation of Δn. As can be seen in Figure 5-9 (b), all three normalized horizontal lines are similar and do not show any significant differences between measurements in the vicinity of the edge of the heavily diffused feature. This is possibly due to very short carrier lifetime conditions in the diffused layer (unpassivated surface and low temperature) regardless of carrier injection levels, or simply that this range of injection levels does not incur much change in carrier lifetime. Despite the fact that this result does not clearly show the impact of lateral carrier diffusion on our analysis technique, this effect still seems most likely to be the cause of the observed reduction in calculated depth factor near the edges of heavily

diffused features. It is therefore concluded that the analysis method developed in this work can be reliably used to determine the depth factor of boron diffused surfaces but has limited accuracy around the edges of locally doped features.

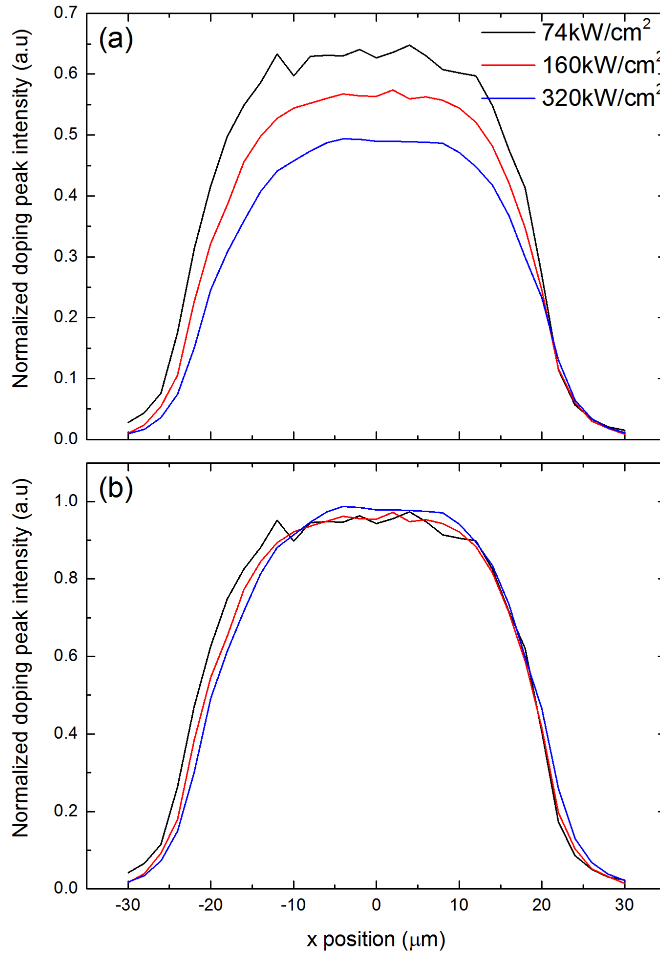

Figure 5-9 (a) Horizontal section of 2-D map of LB3-40μm sample's doping peak PL intensity, measured with different excitation intensity (74, 160, 320 kW/cm^2), and (b) normalized to 1 for the comparison.

5.5 CHAPTER SUMMARY

This chapter has investigated the potential use of low temperature μ-PLS measurements to determine the inhomogeneous Gaussian function type doping profiles, in terms of N_{surf} and z_f, for heavily boron-diffused silicon wafers. Measured PL spectra were normalized to the underlying Si band-band radiative peak, and the PL spectrum of an undiffused control wafer was subtracted to decouple the doping peak.

It was found that the wavelength of the doping peak and N_{surf} have a simple linear relationship on a semi-log plot and a calibration curve was established which can be applied to estimate N_{surf} in the range 5×10^{18} to 1×10^{20} cm^{-3} from the wavelength of the doping peak alone. Another calibration curve was established for determining z_f, after considering the impact of incomplete dopant ionization. Although the normalized PL intensity of the doping peak showed a monolithically increasing relationship with z_f, some samples, in particular those having N_{surf} less than 10^{19} cm^{-3}, showed a larger deviation from the increasing relationship. Since low temperature intensifies further incomplete ionization of dopant density in a range between 10^{18} and 10^{19} cm^{-3}, effective p-n product and hence the doping peak PL intensity was further reduced at lower temperatures. After correcting the reduction of the doping peak PL intensity by a simple division of the fraction of ionization on the raw PL intensity of the doping peak, a better linear relationship between z_f and the doping peak PL intensity could be established.

It was then demonstrated, using these two calibration curves, that it is possible to reconstruct a boron diffusion profile based on the estimated N_{surf} and z_f, determined via PLS spectral analysis only. It is, however, noted that an accurate parameterization of the excess carrier density during PLS measurement would allow us to quantify z_f with greater precision.

2-D mappings of N_{surf} and z_f were also demonstrated by applying this method at each point with 2 µm resolution on locally diffused samples with small feature sizes (30, 40, 50 µm diameter). A uniform and sharply defined N_{surf} is observed regardless of diffusion feature size, but the estimated z_f varies significantly according to the feature size, being observed to reduce as the perimeter of a feature is approached. This imprecision of depth factor near feature edges is attributed to considerable lateral carrier diffusion, which results in carrier smearing and an unreliable calculation of diffusion depth within a distance of around 10 ~ 15 µm from feature edges.

In the next chapter, the method presented in this chapter is applied to laser-doped silicon.

Chapter 6. Characterization of laser-doped Si formed by different temporal pulse profiles

6.1 INTRODUCTION

In Chapter 4 and in the literature, it was shown that the process of using a laser, specifically when associated with dopant atoms, induces defects and dislocations in laser-processed silicon. Consequently, the main objective when improving laser processes is to suppress laser-induced damage, while maintaining heavy doping for a purpose of formation of ohmic contacts with metal. To achieve this objective, it is necessary to understand the impact and interactions of laser parameters during laser processes in silicon. Although many studies have reported on the impact of laser parameters, mainly focusing on laser pulse energy, the temporal pulse parameters, such as pulse duration and temporal pulse profile shape, have not been studied thoroughly.

As described in 2.3.3, the laser doping process is basically laser-induced liquid phase diffusion. Focused laser pulse irradiation melts silicon substrate, and any dopant elements presented at the interface of the melt will diffuse rapidly into silicon. After termination of the laser pulse, the melted silicon recrystallizes epitaxially with the substitutional dopants. The high-speed non-equilibrium crystal regrowth enables more dopants to be trapped substitutionally in the lattice so they can readily exceed equilibrium solid solubility limits, but this high regrowth speed works negatively on crystallographic quality. It was reported that the degree of crystallographic damage is likely to increase with the velocity of the recrystallization [163, 164]. Thompson *et al.* [165] reported that an experimental value for the critical amorphization velocity in c-Si has been measured as 15 m/s. Other experimental evidence was given that the grain size of laser annealed amorphous silicon (a-Si) increases as the recrystallization velocity decreases [166]. Another source of defects is the high stress gradient owing to the high temperature gradient (10^8 ˚C/cm) and high temperature characteristics of laser processing [167].

In order to control the recrystallization velocity, three major methods were suggested [168]: 1) substrate heating, 2) variation of the pulse duration, and 3) alteration of the thermal conductivity of the base region. The third approach, manipulating thermal conductivity of base region, is not ideal for most cases since it is not always possible to choose/change the base material/composition. Substrate heating is the most easily accessible approach, and its effectiveness was proven experimentally by Young *et al* [163]. Varying the pulse duration is also an easily accessible approach, and has been proven theoretically to be effective for reducing the recrystallization velocity. For the same amount of pulse energy, the recrystallization velocity decreases with increasing pulse duration [168]. These three methods basically control the thermal gradients in the material and the recrystallization velocity is determined primarily by the thermal gradients at the melt-solid interface [80, 168]. Therefore, controlling pulse duration is also effective to alleviate the high stress gradient owing to the high temperature gradient. However, this relationship is valid only when the pulse energies for different pulse durations are controlled below the threshold of material ablation. Above the threshold, the material ablation is occurred and becomes a more significant factor in determining crystallographic damages [156, 168]. Melting depth, and hence the doping profile of the laser-doped region, is also determined according to pulse duration and shape. Therefore, it is worthwhile investigating the impact of temporal parameters on the laser-doped region experimentally.

This chapter first investigates the impact of temporal parameters, pulse duration and temporal profile shape on the doping profile of laser-doped silicon in terms of N_{surf} and doping depth. The method presented in Chapter 5 is then applied to determine whether it is still effective for estimating the doping profile of laser-doped silicon. In addition, 2-D mapping of the N_{surf} and z_f of locally/fully laser-doped silicon is performed, as demonstrated in the previous chapter. The impact of temporal parameters on recombination properties is also investigated. It is found that the μ-PLS measurement could potentially be used for the quantification of recombination properties.

6.2 IMPACT OF LASER TEMPORAL PARAMETERS ON THE DOPING PROFILES OF LASER-DOPED SILICON

6.2.1 Experimental details

Low resistivity (~ 5 Ω·cm) n-type FZ crystalline silicon substrates with a thickness of about 400 μm were used for this study. As optical characterization tools were used, the sample substrate should have a planar surface. All the sample surfaces were already chemically etched from the manufacturer but were etched again in 25 % TMAH solution at 80 ˚C for 5 minutes, to ensure no surface damage and planar surfaces before any processing took place. Prior to depositing the dopant precursor, all substrates were RCA cleaned to remove any precipitates. B155 Poly boron SOD from *Filmtronics* was then deposited using a benchtop spinner at 2000 RPM for 50 seconds. The dopant source layer was subsequently baked at 90 ˚C for 20 minutes to evaporate solvents.

The employed laser system in this chapter was a frequency doubled 532 nm fibre laser (*PyroFlex 25*) which enables tuning of the pulse duration (1 to 600 ns) and the temporal pulse profile in 1 ns resolution. The diameter of the on-spot laser beam was measured to be about 16 μm and showed a Gaussian distributed spatial beam profile. The pulse repeat frequency was fixed at 50 kHz for all processes. In order to measure the sheet resistances R_{sh} and doping profiles, the large area of laser doping (10 mm × 10 mm box structures) was created by spacing circular laser beams with 4 μm or 8 μm in both x- and y-axes. After laser irradiation, the remaining SOD on the surface was removed via another RCA cleaning step. The doping profiles were measured using the ECV technique.

The temporal pulse profiles examined were measured via photodiode and converted to instantaneous power as shown in Figure 6-2 (a) and (c). Four different temporal profile shapes were employed to express distinctive scenarios of instantaneous power change while the pulse energy and duration were kept identically at 24 μJ and 600 ns, respectively. An isosceles triangular (ISO) waveform represents simple rise and drop, similar to the typical Gaussian type applicable to most laser systems. An inclining (INC) waveform means abrupt termination of the pulse after a linear increase to peak power, whereas a declining (DEC) waveform exemplifies a surge of peak power at the beginning of the pulse then monolithic decrease. The consistent power over the pulse duration is described as a square (SQR)

waveform. When applying different pulse durations, the pulse energy which is able to induce a reasonable level of doping (at least ~ 100 Ω/sq) is chosen for the corresponding pulse duration, while taking the ISO waveform as the default shape.

6.2.2 Results and discussion

Determination of pulse energy for different pulse duration via R_{sh} measurement

Figure 6-1 summarizes the measured R_{sh} of the large area of laser doping, processed with various laser parameters. First of all, heavier doping was observed as beams were spaced closer together. Since the spatial beam profile is Gaussian type with a diameter of 16 µm, beams should be placed closely enough, less than 8 µm, for the uniform processing of the large area. The closer location of the beams also means more laser energy is irradiated for the unit area which increases the melting time and depth with more dopant atoms, and therefore decreases R_{sh}.

The laser doping inducing pulse energy for different pulse durations can be found in Figure 6-1 (a). Basically, for all pulse durations, at a given pulse spacing, R_{sh} decreases with pulse energy increase due to the increased melting time and depth. However, R_{sh} increases above a certain threshold, since too high a pulse energy evaporates or ablates the substrate rather than extending the melting cycle of laser doping. The window of the laser doping inducing pulse energy is wider for longer pulse durations as observed in Ref. [156]. This indicates that the longer pulse is less vulnerable to variation in pulse energy. However, the longer pulse requires a higher pulse energy for a similar level of R_{sh}, when compared to the shorter pulse. For example, in a case of 4 µm spacing, the pulse energies for a doped layer of about 90 Ω/sq are 7, 11, 16 and 20 µJ for 100, 200, 400 and 600 ns pulse durations, respectively.

The impact of the temporal profile shape on R_{sh} is shown in Figure 6-1 (b). Although all waveforms show decreasing R_{sh} with increasing the pulse energy, a smaller change is observed for the SQR waveform. The SQR waveform shows a relatively higher R_{sh}, particularly at higher pulse energy (24 µJ), than the other three triangular waveforms.

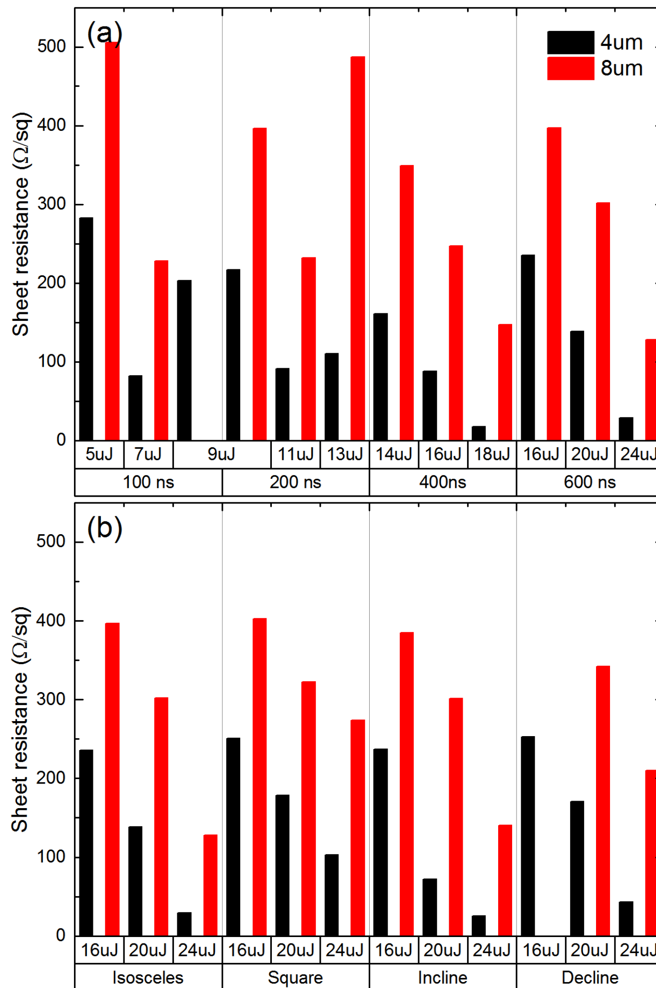

Figure 6-1. The sheet resistances of the large area of laser doping, processed with (a) different pulse durations (100, 200, 400 and 600 ns) and (b) different temporal pulse profiles (ISO, SQR, INC and DEC)

Doping profiles measurement

Figure 6-2 (b) plots doping profiles of the large area of laser doping, processed with 4 µm spacing and different temporal profile shapes. Corresponding R_{sh} are provided for comparison. The same pulse energy of 24 µJ was given to all temporal profiles. Nevertheless, the resultant doping profiles and R_{sh} are quite different according to the shape of the temporal profiles. Overall, all doping profiles in Figure 6-2 (b) have relatively deep depth > 1.5 µm regardless of the shape because of the long pulse duration of 600 ns. It is notable that both the ISO and the INC waveforms give almost identical doping profiles and hence a similar R_{sh}, whereas the SQR waveform gives a significantly higher R_{sh} and lower N_{surf}. This is attributed to the peak power of the temporal pulse profile, showing the same peak power of around 80

W for the ISO and the INC waveforms, but only 40 W for the SQR waveform. Although the highest peak power of around 130 W is observed in the INC waveform, the corresponding N_{surf} is slightly lower than the N_{surf} of the ISO and the INC waveform. It is speculated that such a high peak power is likely to incur slight ablation in the sub-surface of the doped layers, thus leading to a decreased N_{surf}.

Doping profiles created by different pulse durations with 4 μm spacing are plotted in Figure 6-2 (d). Since the pulse energy is adjusted according to the pulse duration, based on the previous R_{sh} measurement, it is hard to clearly distinguish the impact of peak power and pulse duration. In general, if a longer pulse with a lower peak power is applied, a deeper depth with a lighter N_{surf} is created in the doping profile. In other words, a shallower depth with a heavier N_{surf} is produced when the temporal profile has a shorter duration with a higher peak power. This means that the N_{surf} and the depth of doping profile of a laser-doped region, maintaining a target R_{sh}, can be tailored by manipulating the pulse temporal profile.

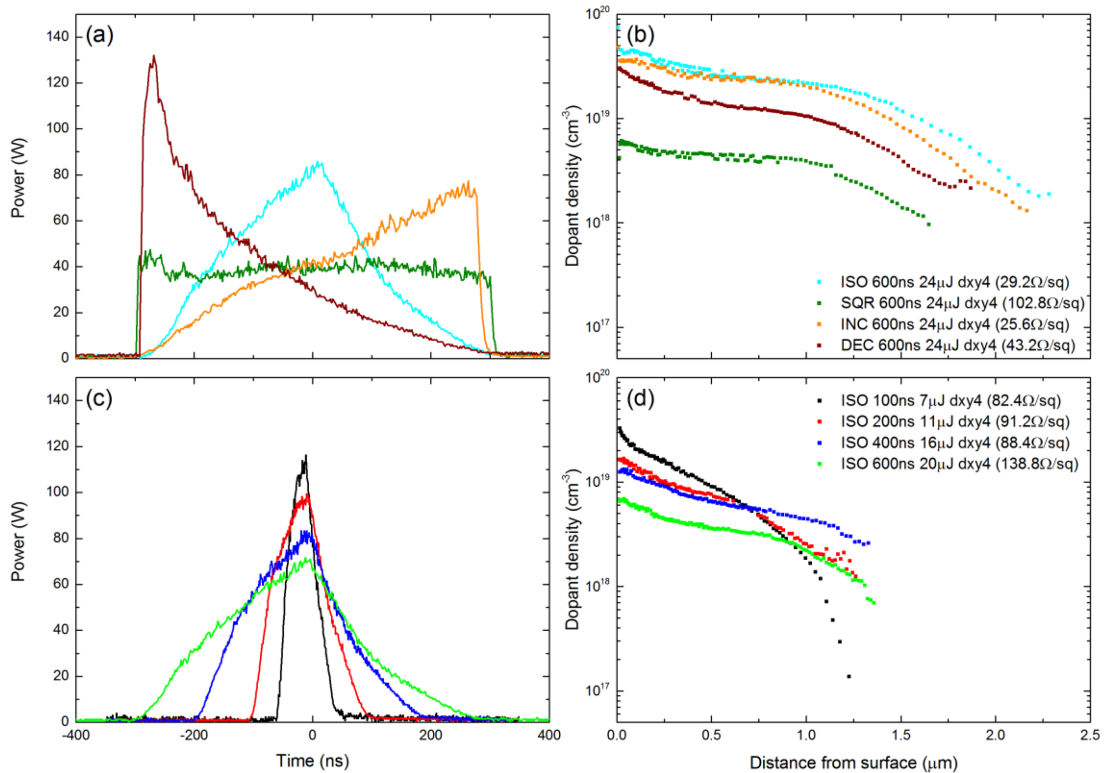

Figure 6-2 (a,c) Temporal pulse profiles and (b,d) corresponding doping profiles measured via ECV profiling when applying (a,b) different shapes (ISO, SQR, INC and DEC), or applying (c,d) different pulse durations from 100 to 600 ns. Measured sheet resistances are provided for the comparison.

6.3 RECONSTRUCTING DOPING PROFILES OF LASER-DOPED SILICON

A brief examination in the PL spectra of laser-doped samples gave the impression that the wavelength and PL intensity of doping peak of laser-doped silicon also follow the same trend – linear relationship between the wavelength/PL intensity of the doping peak and N_{surf}/z_f – as was observed from the thermally diffused samples. Hence, the two calibration curves (equations (5.3) and (5.4)) established in Chapter 5 were initially attempted to estimate the N_{surf} and z_f of the laser-doped samples. However, the reconstructed doping profiles were not accurate, showing great discrepancy compared to the measured ECV curves. This indicates that the demonstrated relationship between the PL components and doping profile defining key parameters is valid qualitatively for any doped samples, but has a different numerical relationship depending on the process and circumstances (see also 6.6). Therefore, new calibration curves for laser-doped silicon are established using the large area of laser doping samples used for R_{sh} and ECV measurements in the previous section.

A total of 15 different doping profiles were used, with N_{surf} ranging from 2.97 $\times$ 10^{18} cm^{-3} to 4.36 $\times$ 10^{19} cm^{-3}, and with a range of different doping depths between 0.6 μm and 2.5 μm. The same μ-PLS system and measurements set-ups in Chapter 5 were applied for all measurements exception of excitation power. The power is slightly increased to 12 mW for clear spectra measurements, in particular for heavily laser-damaged samples.

6.3.1 Estimating N_{surf} and z_f of laser-doped silicon

For laser-doped silicon samples, the relationship between the wavelength of the doping peak and N_{surf} is plotted in Figure 6-4 (a), and is described by

$$\lambda_{doping\ peak} = (5.39 \pm 0.96)\ \ln(N_{surf}) + (916.43\ \pm 41.75) \quad (6.1)$$

Error bars indicate one standard deviation of measured wavelengths across the large area of laser doping. A linear relationship between the wavelength and N_{surf} was observed but is not very solid compared to that of the thermally diffused samples as shown in Figure 5-2 (d). This is possibly due to the irregular condition of the surface after laser processing. The optics of the laser system does not homogenize a beam

spatially, and thus form a typical Gaussian spatial beam. As a result, the region processed with an isolated laser beam can have spatially different surface transformation as well as different levels of doping. Thus, the large area of laser doping was created by overlapping beams by more than 50 % to ensure uniform irradiation over the large area. Nevertheless, the surface of the large area feature contains traces of beams across the region. This indicates that the surface is not only not doped homogeneously, but also influences the luminescence measurement due to unexpected optical scattering or trapping at the irregular surface.

The function type of the doping profile of laser-doped silicon is examined using the same method in 5.3.2. The coefficient of determination R^2 of the Gaussian and ERFC functions was calculated for all 15 laser-doped samples in Figure 6-3. All measured profiles show a better fit to ERFC, therefore z_f was fitted from ERFC for all samples.

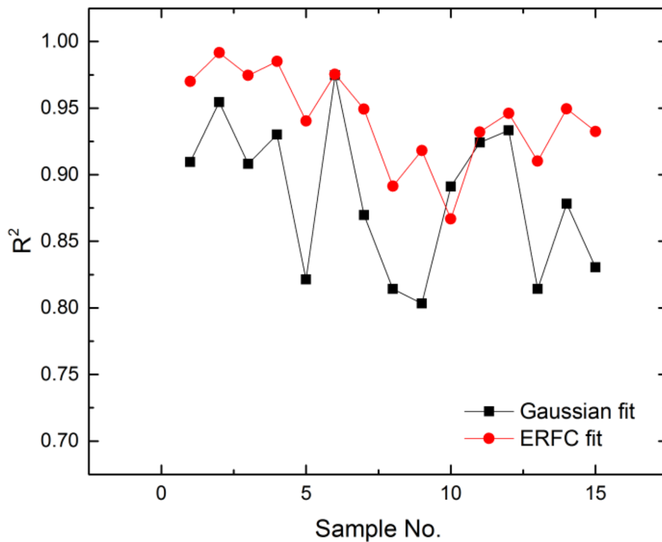

Figure 6-3 The coefficient of determination R^2 of two modelled functions (Gaussian and ERFC) for 15 laser-doped samples. An R^2 of 1 indicates that the modelled functions perfectly fit the measured points.

The second calibration curve for the doping peak PL intensity is plotted as a function of z_f in Figure 6-4 (b) and is formulated in equation (6.2). Here again, a better linear relationship is established after considering the impact of incomplete ionization of dopants on doping peak PL intensity at low temperature.

$$I_{corrected} = (0.599 \pm 0.104)\, Z_f - (0.117 \pm 0.122) \qquad (6.2)$$

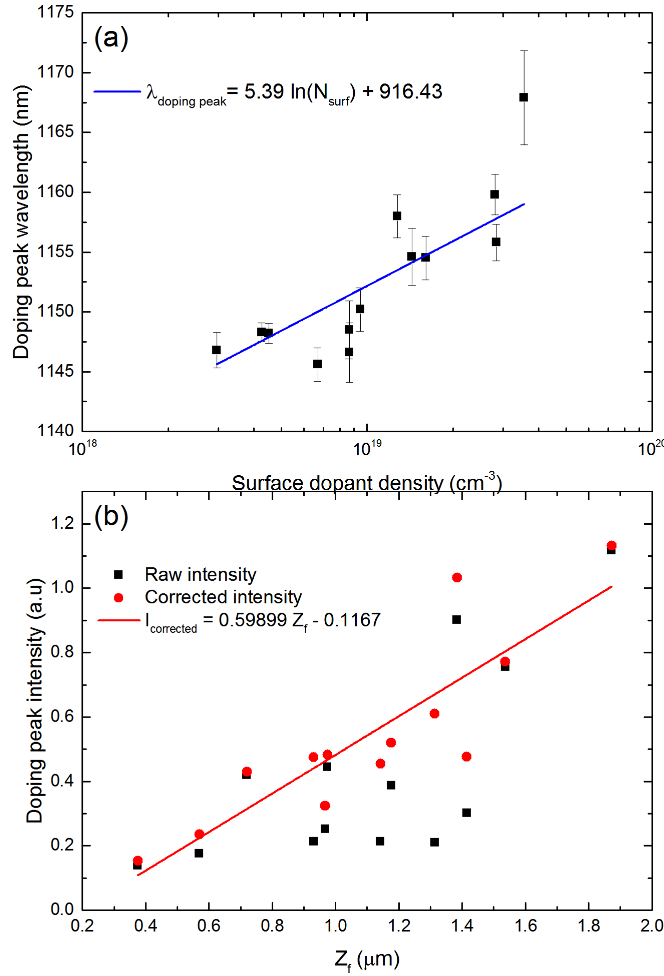

Figure 6-4 (a) Measured wavelengths of the doping peaks as a function of N_{surf} (b) Normalized PL intensity of the doping peak as a function of z_f without correction (black), and including a correction for the effect of incomplete ionization on the PL intensity (red).

Both calibration curves are valid only for laser-doped silicon with an ERFC type doping profile and when the PLS measurement is conducted under conditions similar to those stated in this chapter.

6.3.2 Reconstructed doping profiles of laser-doped silicon

To verify the calibration curves established in the previous section, the doping profile was reconstructed from μ-PLS measurements alone. Using equation (6.1), N_{surf} was estimated from the measured wavelength of the doping peak. After the normalized PL intensity of the doping peak was corrected with the fraction of ionization of this estimated N_{surf}, it was used to calculate z_f based on equation (6.2). Substituting all estimated parameters in equation (5.1) with assumption of $z_p = 0$, the reconstructed doping profiles were plotted as shown in Figure 6-4, in which four

distinctive doping profiles of laser-doped samples are shown with their corresponding sheet resistances.

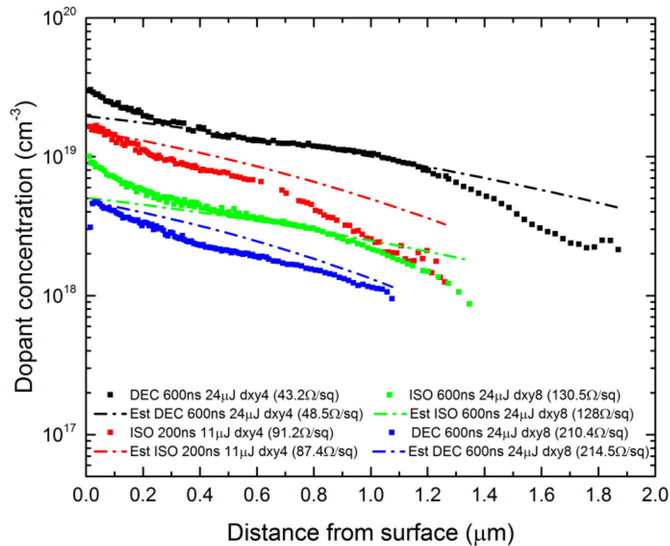

Figure 6-5 Measured and reconstructed doping profiles of four distinctive laser-doped samples, with their corresponding sheet resistance.

The reconstructed curves show some mismatches to the measured ECV curves. Although all measured ECV curves are mathematically close to ERFC in the fitting simulation, the doping profile actually contains partially different gradients. In particular, an accumulation of dopants is observed within about 300 nm near the surface region, which forms a steeper gradient in the profile. This was not observed in excimer laser-doped silicon (see Figure 6-16 (a)). This phenomenon is due to the segregation effect at the solid-liquid interface during the laser-induced melting and solidification process [86, 169, 170]. During epitaxial recrystallization, dopant density C_s in the solid just formed at any moment from the liquid-solid interface is determined by the interface segregation coefficient k_i of the dopant (defined as the ratio of the dopant concentration in the solid C_s to that in the liquid C_l at the liquid-solid interface). Dopant density in the solid is then given as $C_s = k_i C_l$ and an amount of $(1\text{-}k_i)C_l$ is rejected into the nearest liquid layer. This process is continued until the solid-liquid interface reaches near the surface and the excessive dopants remaining in the liquid are considered to have accumulated to the surface [86]. Such surface accumulation therefore only occurs when k_i is less than unity, as schematically represented in Figure 6-6.

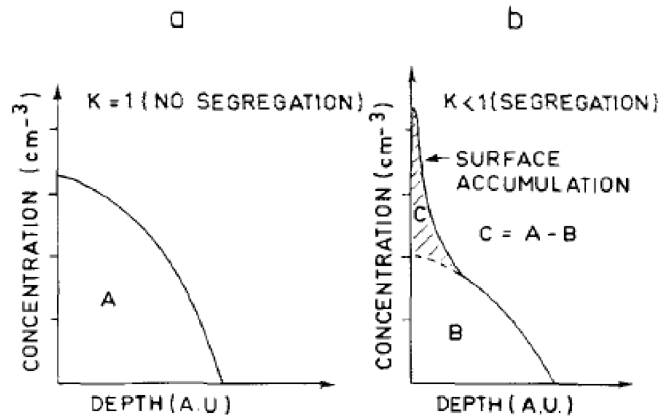

Figure 6-6 Schematic illustration of the surface accumulation of dopants due to the segregation effects for (a) $k_i = 1$ and (b) $k_i < 1$ after laser doping. The figure is taken from Ref. [170].

Values of k_i depend not only on dopant elements, but also on the recrystallization velocity [86, 169, 171]. When the recrystallization velocity is so slow that a quasi-equilibrium condition is maintained, the value of k_i becomes close to the value of the equilibrium segregation coefficient k_0. On the other hand, when the recrystallization velocity is significantly high (> 2.5 m/s), applicable in a typical laser doping process using a few tens nanosecond pulses, this value becomes much higher than the equilibrium segregation coefficient k_0. Table 6-1 lists the equilibrium value k_0 and its high value k_i for some dopant elements under typical nanosecond-pulsed laser doping. For boron in silicon, the value of k_i under fast regrowth velocity is very near unity and hence leads to no boron accumulation at the surface. However, its equilibrium value k_0 is known to be 0.8, which decreases further with increasing boron concentration in the silicon melt [172]. As a result, observation of the surface accumulation in the measured doping profiles (Figure 6-2 and Figure 6-5) indicates that there was relatively slow recrystallization.

Dopant element	Equilibrium segregation coefficient k_0	Interface segregation coefficient k_i
B	0.8	0.9 – 1.0
P	0.35	0.9 – 1.0
As	0.3	0.9 – 1.0
Sb	0.023	0.8 – 1.0
Ga	0.008	0.15 – 0.3
In	0.0004	0.1 – 0.2
Bi	0.0007	0.25 – 0.42

Table 6-1 Values of k_0 and k_i for some dopant elements in silicon [169].

Surface accumulation results in a less accurate estimation of N_{surf} and z_f in addition to the impact of bad sample surface morphology. However, despite the non-ideal estimation of parameters, the discrepancy between the reconstructed profiles and the measured ECV profiles is not big in terms of sheet resistance. The sheet resistances of the reconstructed profiles were calculated and compared to the 4pp measured sheet resistances as shown in Figure 6-7. Notably, they show reasonably good agreement.

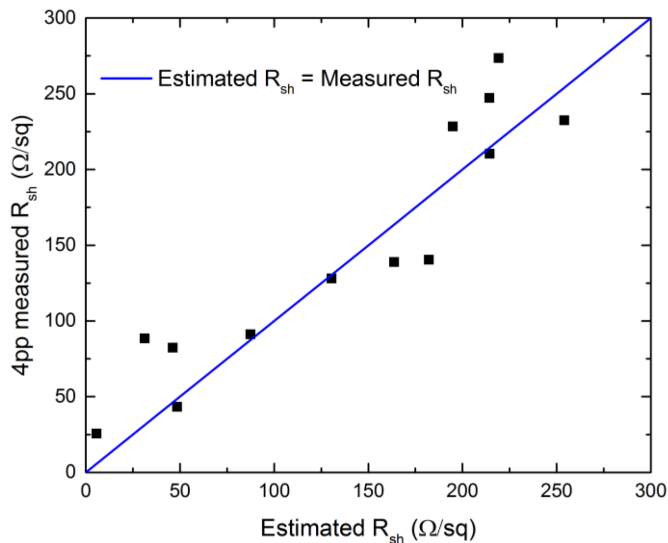

Figure 6-7 Comparison between the 4pp measured R_{sh} and the μ-PLS estimated R_{sh}.

6.4 2-D MAPPING OF N_{SURF} AND Z_F FOR THE FULL AREA AND LOCALLY LASER-DOPED SILICON

Figure 6-8 shows maps of N_{surf} and z_f, for the large area laser-doped samples with the corresponding R_{sh}, measured via a 4pp and calculated using estimated N_{surf} and z_f via the µ-PLS analysis method. Firstly, the results confirmed the anticipated laterally inhomogeneous doping of the large area laser-doped sample from the fluctuating N_{surf} and z_f over the processed region. Secondly, the impact of pulse spacing on the large area process (pulse overlapping) was observed when comparing between Figure 6-8 (a,c) and Figure 6-8 (b,d), even though two different temporal profiles were applied. In Figure 6-8 (d), the intervals of the depth factors correspond to the placements of the pulses. Relatively deep depth factors are repeated approximately every 8 µm on both axes, as single pulses were placed over a large area with this spacing. However, 4 µm spacing (Figure 6-8 (d)) shows a relatively similar level of depth factors without a clear pattern of pulse location over the region.

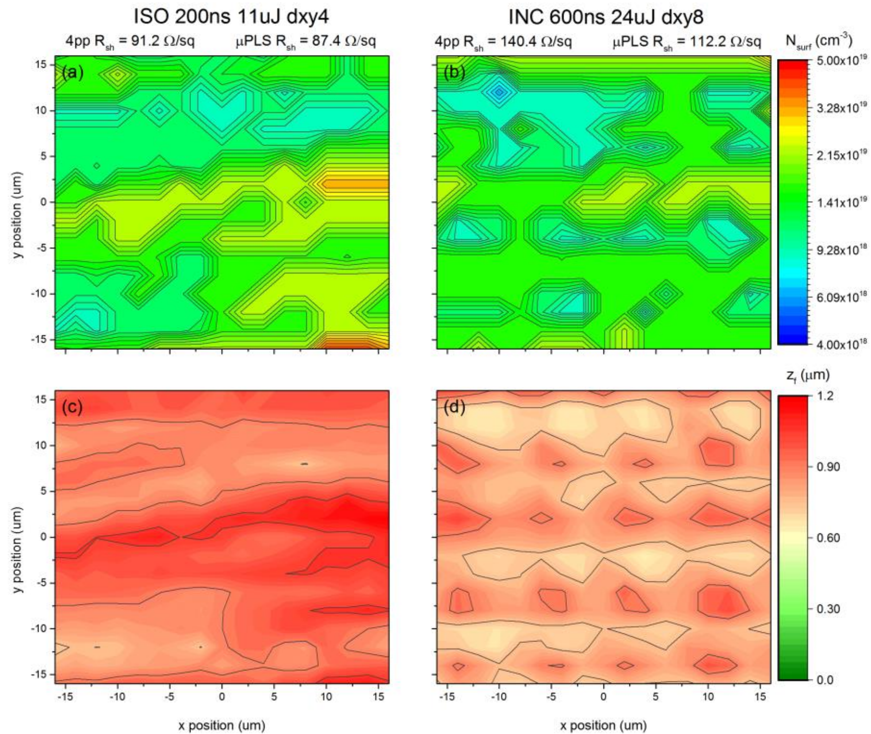

Figure 6-8 2-D scanned maps of N_{surf} and z_f, for the large area laser-doped samples, processed with (a,c) 200 ns ISO waveform and 4 µm beam spacing, with (b,d) 600 ns SQR waveform and 8 µm spacing.

However, such patterns are not observable in the maps of N_{surf} with both 4 and 8 μm spacing and in which it is hard to discern any other clear pattern. This is possibly due to the different responses of N_{surf} and z_f to a single beam process. Figure 6-9 (c) and (d) shows that a deep z_f corresponds to the centre of a beam. Heavy N_{surf}, meanwhile, does not accord with the centre of a beam, as shown in Figure 6-9 (a) and (b). Interestingly, lighter surface doping occurs at the centre of a beam while the deep doping depth is maintained.

The impact of the temporal profile described in 6.2 is well illustrated in the maps of locally laser-doped features. In Figure 6-9 (a) and (c), it is observed that the temporal profile with a shorter duration and a higher peak power (i.e. the 100 ns ISO waveform, 120 W) creates a heavier N_{surf} with a shallower z_f. On the other hand, a lighter N_{surf} with a deeper z_f is created when applying a temporal profile with a longer duration and lower peak power.

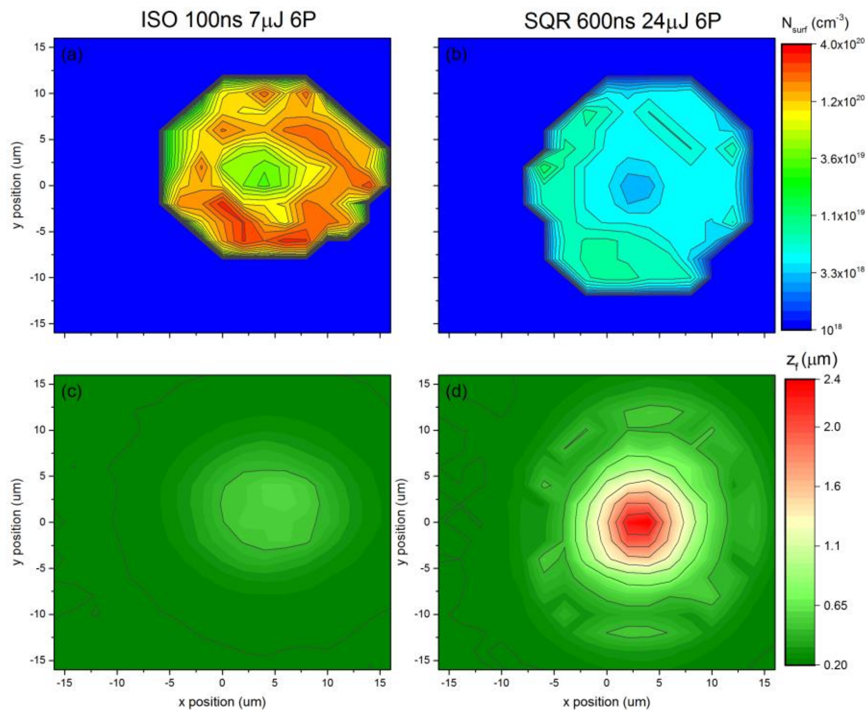

Figure 6-9 2-D scanned maps of N_{surf} and z_f, for locally laser-doped samples, processed with (a,c) 100 ns ISO waveform and 6 repeat pulses, with (b,d) 600 ns SQR waveform and 6 repeat pulses.

All of the N_{surf} and z_f mapping results of locally laser-doped features are summarized in Figure 6-10. In order to be able to summarize these in one plot,

averaged values within the doped region are used. Error bars mean one standard deviation of varying value within the doped region. Corresponding R_{sh} is also calculated using the average values of N_{surf} and z_f to show the doping level of each laser parameter combination comprehensively. In general, the impact of temporal profiles on the doping profiles described in 6.2 is well presented in this figure. Additionally, it is possible to observe the impact of repeat pulses, which induces a deeper doping depth. However, this increase in doping depth is only observed up to 3 pulses. After that, the depth seems to be saturated.

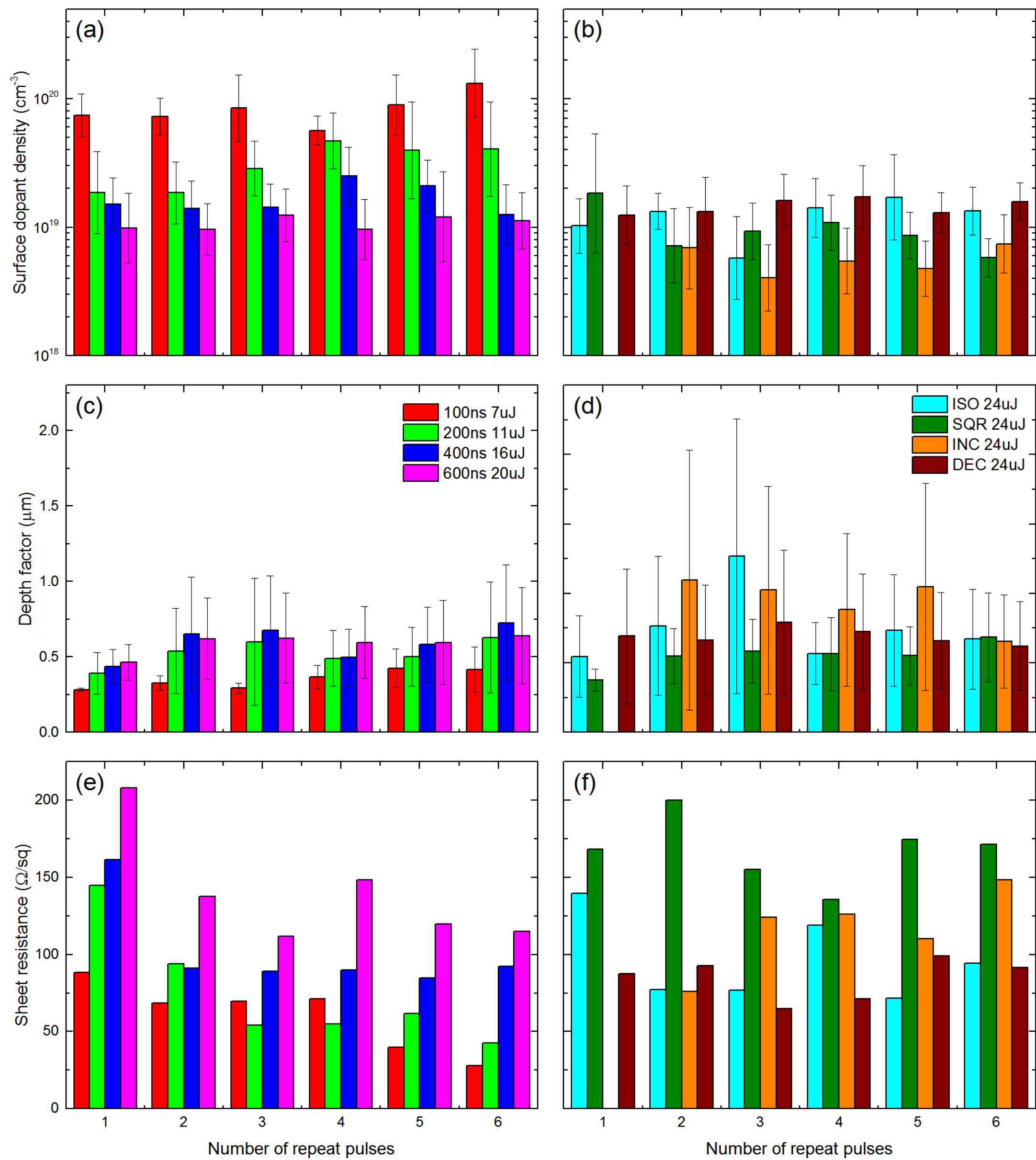

Figure 6-10 Estimated N_{surf}, z_f and R_{sh} as a function of repeat pulse numbers, for locally laser-doped features processed with different pulse durations (a,c,e) and different pulse shapes (b,d,f). Average value (bar graph) and one standard deviation (error bar) across the doped region are used for this plot. The sheet resistance is calculated using average values of N_{surf} and z_f

6.5 RECOMBINATION PROPERTIES OF LASER-DOPED SILICON

In Chapter 4, by comparing the distinctive defect-related PL spectra at specific locations within the micron-scale laser-processed region, it was found that the main recombination source of the laser-processed region is at the interface of the melt-unmelted region. However, this analysis enables only a relative comparison of the recombination properties among the investigated specimens, so this remains a qualitative characterization that could not be used to evaluate an absolute level of recombination properties. In this section, this limitation is improved by correlating the quantified recombination parameter J_0 with the normalized defect-related PL spectra, which demonstrates the potential of the μ-PLS method for the quantification of recombination properties.

6.5.1 Sample preparation

In addition to the large area laser-doped structure, we created 10×10 mm^2 squares of circular laser beam arrays with an array pitch of 60 μm for the μ-PLS analysis, and for extracting the recombination parameter $J_{0,laser}$ of the locally laser-doped features. The same temporal profiles and pulse energies (Figure 6-2) were applied with a number of repeat pulses from 1 to 6. The surface of the localized feature was then passivated by depositing a 20 nm Al_2O_3 layer on both sides of wafers via thermal atomic layer deposition (ALD). A Beneq TFS-200 ALD reactor was used with a trimethylaluminium (TMA) precursor and water for the oxidant. The deposition temperature was kept at 200 ˚C. The passivation effect of the as-deposited Al_2O_3 layer was activated by annealing at 425 ˚C for 30 mins in forming gas. Al_2O_3 was chosen to minimize the post-annealing effect of the laser damage and dopant redistribution, which is observed in a high-temperature oxidation process after the laser doping process [44], as the Al_2O_3 film is made at relatively low temperatures (also see 6.6). In addition, the optical properties of Al_2O_3 deposited silicon are very close to that of bare silicon, so it is not necessary to consider its optical impact on PL emission.

6.5.2 Quantified recombination parameter $J_{0,laser}$ of laser-doped silicon

The PL image-based analytic approach is employed to quantify the recombination properties of locally laser-doped features (see 2.4.2). All the uncalibrated PL images of samples were converted to J_0-images as shown in Figure

6-11. We then determined the recombination parameter $J_{0,laser}$ of the locally doped regions for each laser parameter within a 6 × 6 mm^2 sized region inside the laser-doped boxes, to minimize the influence of carrier smear at the edges.

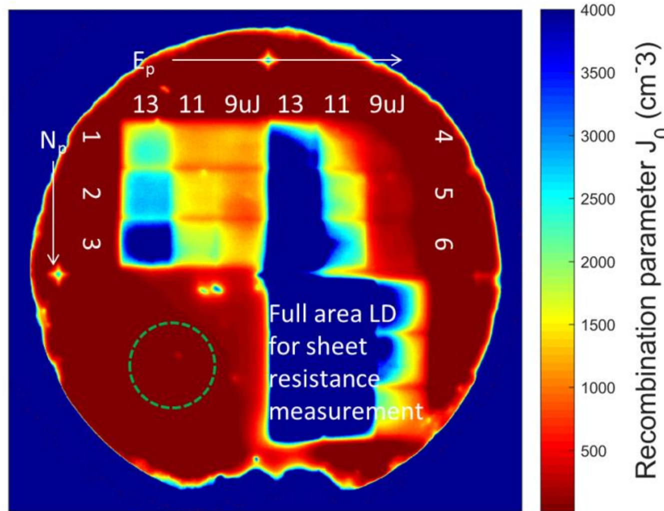

Figure 6-11 Extracted $J_{0,laser}$ image and the arrangement of the large area and locally laser-doped structures with various laser parameters, applying 200 ns ISO waveforms with 3 different pulse energies (9, 11 and 13 μJ) and repeat pulses from 1 to 6. The placement of the inductive coil for PCD measurement is indicated by the dashed circle.

Figure 6-12 summarizes all values of recombination parameter $J_{0,laser}$ of the localized features processed with different temporal profiles as a function of a number of repeat pulses. It was possible to confirm that the temporal pulse profile not only affected the doping profile, but also the recombination properties.

Firstly, $J_{0,laser}$ values in the range between 500 and 3000 fA/cm^2 were achieved by applying various combinations of temporal parameters. The lower value, $J_{0,laser} < 1000$ fA/cm^2 was observed to increase pulse duration. When comparing the shortest and longest ISO waveforms, the overall values of $J_{0,laser}$ were lower for the longest ISO waveform, in spite of heavier doping (heavier N_{surf} and deeper z_f). This indicates experimentally that the long pulse is a very effective way to reduce the recrystallization velocity and hence lower the recombination properties of laser-processed silicon.

Secondly, temporal pulse shape is also quite an influential factor in determining recombination properties. In Figure 6-12 (a), given the same pulse

energy and duration for all shapes, the INC and the DEC waveforms give a higher $J_{0,laser}$ than the other two waveforms. This is likely to be due to the abrupt change of instantaneous power. Although both INC and DEC waveforms show dramatic transitions of power from zero to peak and vice versa, the INC waveform would be more detrimental in terms of thermal profile. For the INC waveform, the temperature gradient, particularly after the termination of the pulse, would be steeper since there is an instantaneous halt in power, more so than for the other waveforms which have a gradual decrease in power. Therefore, this could increase the recrystallization velocity and cause more crystallographic damage. In the case of the DEC waveform, an explosive surge of power from zero to peak in addition to a higher peak value than that of the other waveforms, is likely to induce vaporization of the substrate rather than melting in the sub-surface. However, the subsequent gradual decrease in power over a long period would reduce the thermal gradient and hence decrease the recrystallization velocity, which possibly compensates for the damage induced by the early peak power. Although the SQR waveform also has an abrupt change in power, the degree of power change is not very large, and the power is kept constant over a long period. Therefore, a smoother thermal gradient and relatively slow recrystallization velocity are expected.

Interestingly, it was observed that $J_{0,laser}$ decreases significantly after 4 pulses for all parameter combinations. It is widely believed and has been shown, that multiple pulses incur more laser damage [149]. However, Xu *et al* [156] showed the opposite result – damage recovery after multiple pulses – particularly with long pulse duration. Some other authors also have reported that the damaged surface recovers by irradiating it with additional laser pulses [173-175]. However, it is not clear why it recovered specifically after 4 pulses in our samples.

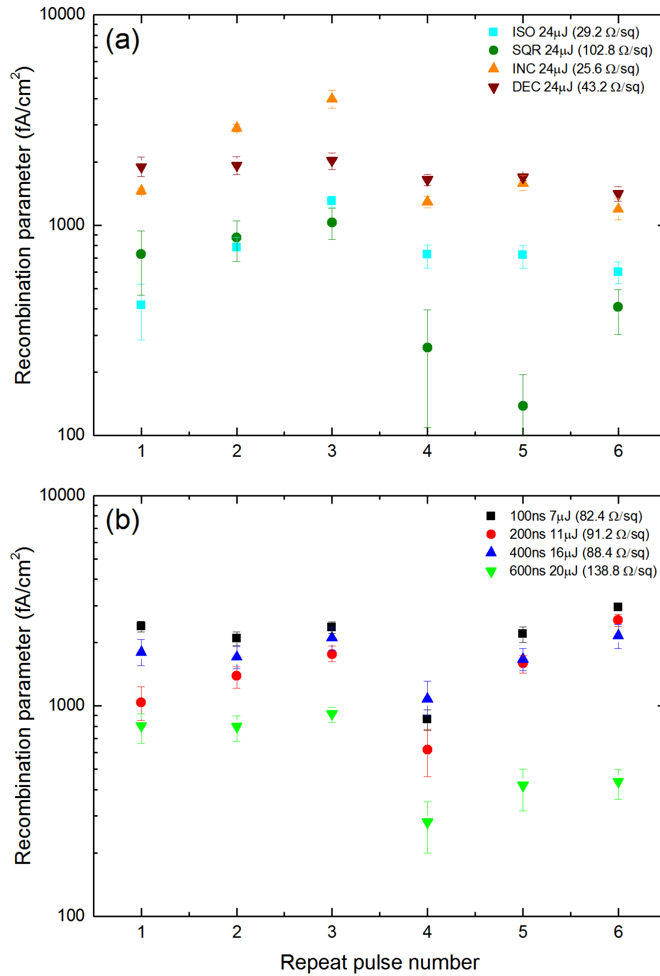

Figure 6-12 Recombination parameter $J_{0,laser}$ as a function of the number of repeat pulses, for locally laser-doped samples, processed with (a) different shapes of temporal profiles, and with (b) different pulse durations.

6.5.3 Qualitative μ-PLS measurement of the recombination properties of laser-doped silicon

As described in 3.5 and Chapter 4, well-known D-lines and PL band over the 1200 nm range represent radiative recombination from dislocations/defects in silicon. Therefore, PL components over the 1200 nm range could be used for evaluating recombination properties. However, to enable fast spectra measurements over hundreds of points and normalization to the Si BB radiative peak, only PL spectra of a limited wavelength range (1100 ~ 1300 nm) were analysed in this chapter. In this wavelength range, only PL spectra in 1200 ~ 1300 nm can be used for recombination analysis but still include PL emissions from intrinsic dislocations, D3 (1290 nm) and D4 (1230 nm). Since it is hard to decouple the D4 line from the doping peak phonon

replica (see Figure 3-7), PL band between 1260 and 1300 nm is defined as a 'defect band' in this analysis.

When mapping the doping peak wavelengths and PL intensities of locally laser-doped features, the defect band was also measured and mapped over the region, as shown in Figure 6-13. It was observed that the distribution of the defect band corresponds to the beam intensity profile as in the z_f characteristic. This result accords with the general fact that higher laser intensity induces more damage. The damage recovery effect after multiple pulses (reduction of $J_{0,laser}$ after 4 pulses in Figure 6-12), is also presented in the defect band map (Figure 6-13 (e) and (f)).

Figure 6-14 displays the distribution of the defect band within the doped region for all the localized features investigated. It is notable that the trend of the defect band to change according to the pulse profile is very similar to that of the quantified parameter $J_{0,laser}$ (Figure 6-12 and Figure 6-14). The defect band tends to decrease as the pulse duration increases. Very high defect band signals are observed when processed with the INC or DEC waveform. The reduction of the defect band after 4 pulses is also shown.

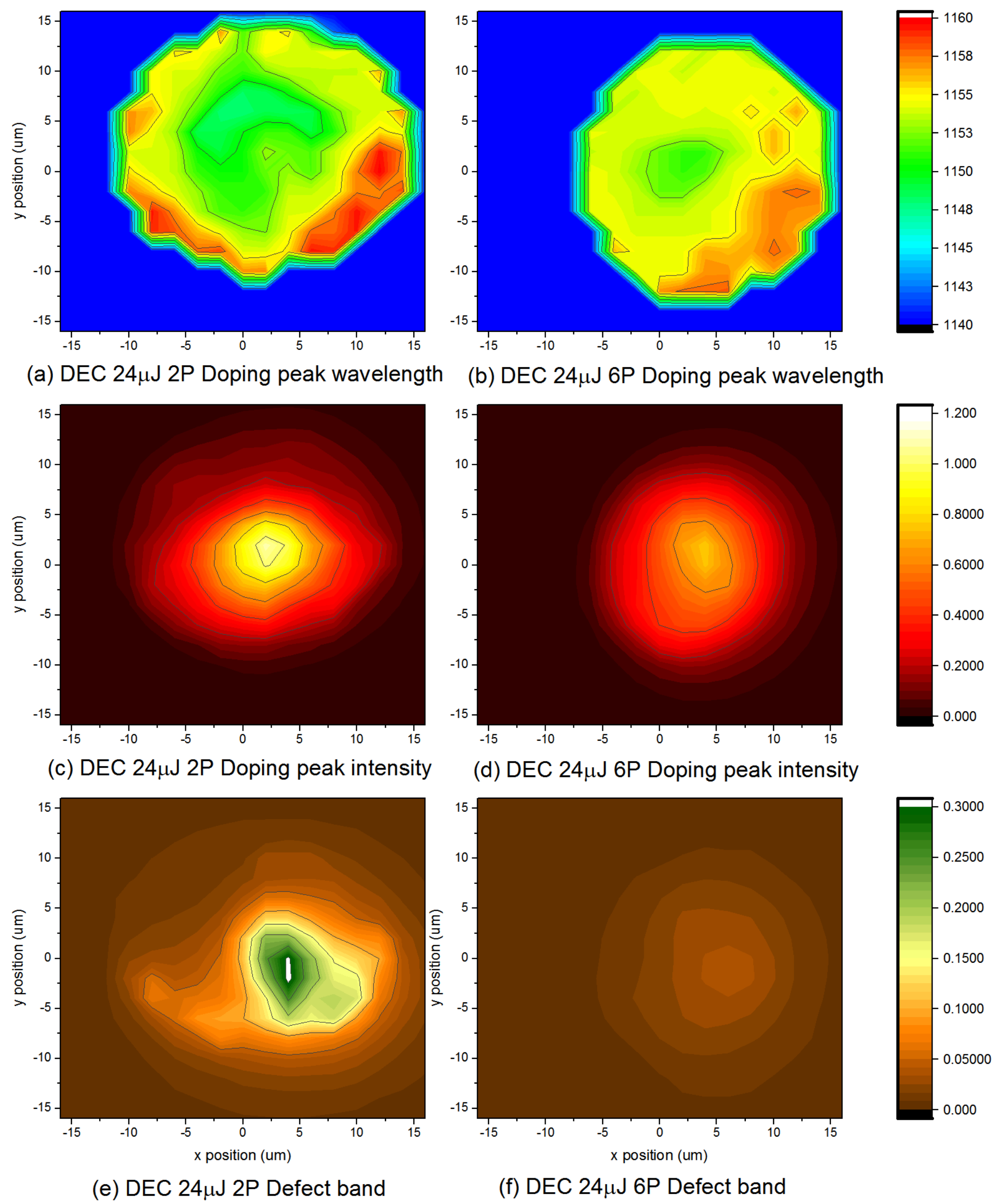

Figure 6-13 2-D scanned maps of wavelengths, normalized PL intensities of the doping peak and the defect band, for locally laser-doped features, processed with the DEC waveform, 24 μJ, 2 or 6 repeat pulses.

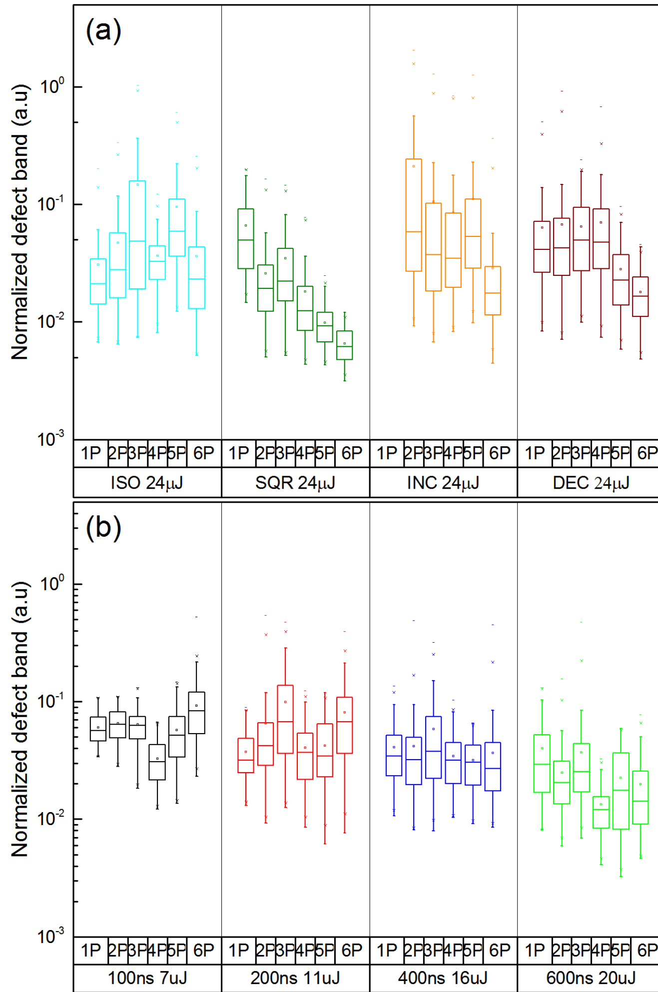

Figure 6-14 Normalized defect bands of all locally laser-doped features investigated in this chapter, processed with (a) different pulse shape and (b) different pulse duration. Box plots display the distribution of data measured within the doped region. The central rectangle spans the first quartile to the third quartile, and its mid-line means median. Other symbols are as follows: - : Min/Max, × : 99 %, □ : Mean.

6.5.4 Correlation between J_0 and defect-related PL spectra

Based on the findings in the previous section, the quantified recombination parameter was correlated with the defect band as shown in Figure 6-15, and the average value of the defect band was plotted as a function of $J_{0,laser}$. Although they do not have a perfect linear relationship, the defect band increases monolithically with $J_{0,laser}$ in a range between 100 fA/cm^2 and 5000 fA/cm^2. This indicates that the recombination properties could be quantified using defect-related PL signals alone. However, there are couple of things which must be considered.

Firstly, the defect band or defect-related PL spectra is only able to represent radiative recombination which has occurred via dislocations or defects. This means

that other non-radiative recombination cannot be assessed. Secondly, analysis based on PL intensity is likely to include more uncertainty. As noted in 6.3.1, a laser-doped sample has an irregular surface morphology, which possibly causes unexpected optical scattering or trapping during the PL measurement. This would be worse for a sample which is processed with high laser fluence/more repeat pulses. Lastly, PL spectra analysis for recombination properties and even for doping level is not effective when it is heavily damaged. This is described in more detail in the next section.

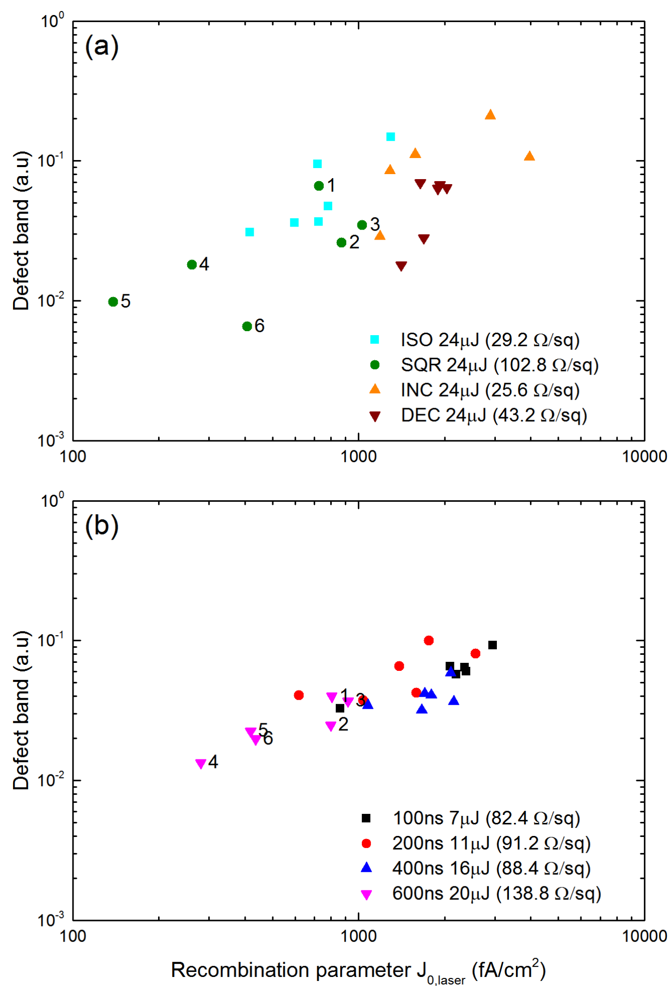

Figure 6-15 The averaged defect band as a function of $J_{0,laer}$, when processed with (a) different pulse shape or (b) different pulse duration. Number of repeat pulses is labelled only for the temporal profiles inducing the lowest $J_{0,laser}$.

6.6 IMPACT OF HIGH DEFECT-RELATED PL SPECTRA

In the previous section, it was mentioned that heavily damaged samples are not applicable to PL spectra analysis. This section describes the reasons based on experimental results.

In this thesis, a new approach is proposed to estimate the doping profiles of thermally or laser-doped silicon samples, utilizing the unique characteristics of the PL spectra of inhomogeneously doped silicon along the depth. When looking at the PL spectra of those samples (Figure 3-7 and Figure 5-2), there are always two very clear peaks, the Si BB radiative and doping peak, in conjunction with very low defect-related PL spectra over the 1200 nm wavelength range. The characteristics of the doping peak are closely related to the degree of BGN and doping depth, so those can be used to quantify dopant profiles. However, as demonstrated in Chapter 4, it is hard to utilize such characteristics when a significantly high defect-related PL band is exhibited. Such a high defect-related PL signal sometimes screens the doping peak making it hard to decouple. Moreover, even if it is possible to decouple the doping peak from the measured PL spectra, the doping peak PL intensity does not reflect the anticipated doping depth. For example, it is well known that multiple pulses create deeper doping depth, so the doping peak PL intensity is expected to increase with the number of repeat pulses. However, this expectation is rarely observed and even the opposite trend is shown when a high defect-related PL band exists.

To further investigate the impact of high defect-related PL band, two sets of samples were prepared. Large area 10×10 mm^2 laser-doped regions were made on TMAH-etched high resistivity n-type substrates using the same SOD and excimer laser set-ups as in Chapter 4. After the laser doping process, residual SOD films on the sample surface were removed via RCA cleaning. A dry thermal oxidation at 1000 ˚C followed by annealing in N_2 was applied to one of the two sets. A grown oxide film was then removed in HF solution for ECV and μ-PLS measurements.

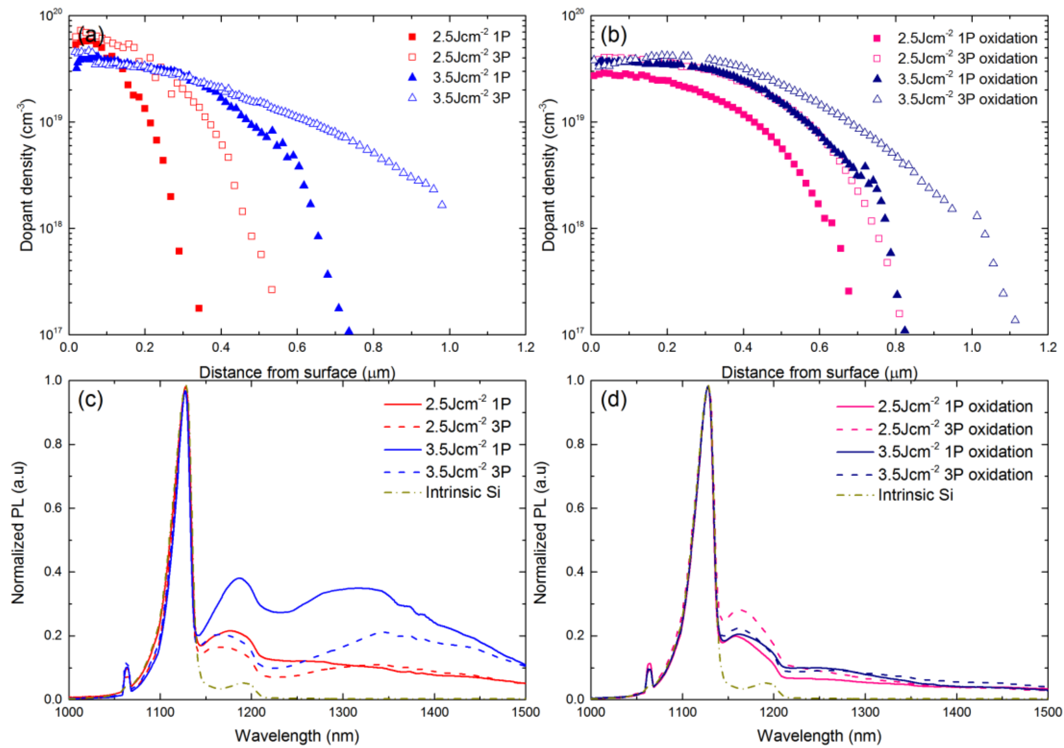

Figure 6-16 Doping profiles of excimer laser-doped silicon samples, processed with 2.5/3.5 J/cm^2 and 1/3 repeat pulses (a) without and (b) with subsequent oxidation process. Corresponding PL spectra are depicted in (c) and (d), respectively.

Figure 6-16 (a) plots the doping profiles of excimer laser-doped samples without a high-temperature oxidation process. Corresponding PL spectra show distinguishable doping peaks as well as high defect-related PL spectra, as depicted in Figure 6-16 (c). As the laser pulse fluence and repeat pulse increase, the depth of the doping profile increases while the surface dopant density decreases, as has been reported by many authors [38, 39, 104]. However, it is not reflected in doping peak PL intensity and wavelength. Normalized PL intensities of the doping peaks in the figure do not correspond to measured doping depth. The wavelength of the doping peak also does not accord with surface dopant density. For instance, for the sample processed with 3.5 J/cm^2 and a single pulse, ECV measurements show the lowest N_{surf} and second deepest z_f, whereas the PL spectra measurements show the highest doping peak PL intensity and wavelength, among all the measured samples.

The high-temperature process has re-distributed dopant atoms, as shown in Figure 6-16 (b). Existing dopants are diffused further into the substrate, forming a slightly lower N_{surf} and deeper depth than before the high-temperature process, the so-called ‘drive-in’ effect. The function type of the doping profiles becomes close to

Gaussian type. Remarkable changes are also observed in the measured PL spectra. A significant reduction in defect-related PL spectra is observed for all samples, which means thermal annealing is effective in reducing laser-induced damages. Furthermore, the discrepancy between the ECV results and PL spectra results is mitigated considerably, although it is still not perfect. It seems that relatively a high defect band, compared to thermally diffused samples and long-pulse laser-doped samples, still negatively affects the characteristics of the doping peak. If there are a significant number of defects/dislocations, all generated excessive carriers do not recombine via band-band radiative recombination. Many of them are likely to recombine through deep-levels (dislocation and defect levels) within the band-gap, and are then represented as PL spectra at a longer wavelength > 1200 nm (smaller than the band-gap energy). Furthermore, more non-radiative recombination processes, which cannot be represented in the PL spectra, will increase. As a result, the doped region containing many defects/dislocations shows an underestimated PL intensity of the doping peak. Therefore, the level of defect-related PL spectra is very crucial in determining the accuracy of the doping peak analysis. A low defect-related PL signal is required for accurate estimation of dopant density.

6.7 CHAPTER SUMMARY

This chapter has investigated the impact of temporal pulse profiles on the doping profiles and recombination properties of laser-doped silicon samples. It has also demonstrated, that inhomogeneous ERFC-type doping profiles can be estimated using the μ-PLS analysis method developed previously in Chapter 5 for heavily laser-doped p-type silicon.

Depending on the temporal pulse profiles, different doping profiles are created, which means that doping profiles can be tailored in more detail by manipulating the temporal profile. For example, a higher peak power with shorter pulse duration induces the doped region to have a higher N_{surf} with a shallower z_{f}. Relatively low $J_{0,laser}$ < 1000 fA/cm^2 was achieved using a longer pulse, verifying experimentally that pulse duration increase is a very effective way to reduce the recrystallization velocity, and hence minimize laser-induced damages. In addition, dopant accumulation near the sub-surface owing to the segregation effect is further evidence

of slow recrystallization velocity in the long pulse laser doping process. Furthermore, the temporal profile shape and change of instantaneous power over time influences the recombination properties of the laser-doped region, even though the same pulse energy/duration is given. It is recommended that abrupt power transitions within a few nanoseconds should be avoided to form fewer recombination active regions. In addition, the lower value of $J_{0,laser}$ after 4 repeat pulses indicates the potential for laser damage annealing using multiple long pulse irradiation.

The method for estimating doping profiles presented in Chapter 5 is also effective for laser-doped silicon but requires new calibration curves to be established based on a set of laser-doped silicon samples. Compared to the thermally diffused samples, the reconstructed doping profile of laser-doped silicon is less precise. A non-homogenized laser beam and its overlapping cause irregular surface morphology and laterally inhomogeneous doping, which reduces the accuracy of calibration curves and PL measurements. Dopant surface accumulation also negatively affects the accuracy of the calibration curves and makes it hard to clearly determine the function type of the doping profile. Nevertheless, the reconstructed profile shows reasonable agreement with the ECV measured curves in terms of sheet resistance.

A number of 2-D mappings of N_{surf} and z_f were also performed for the large area and locally laser-doped features. The laterally inhomogeneous doping and specific patterns owing to regular beam spacing are clearly demonstrated from maps of the full area laser-doped feature. In addition, different map patterns between N_{surf} and z_f are found by observing maps of the locally laser-doped features. The spatial beam profile corresponds to the distribution of z_f, but not N_{surf}.

The defect-related PL component (in this chapter PL spectra in a range of 1260 ~ 1300 nm were defined as a ‘defect band’), is correlated with the quantified recombination parameter $J_{0,laser}$, showing that the defect band increases monolithically with $J_{0,laser}$. It demonstrates that the μ-PLS analysis method could be used to quantify not only dopant density, but also recombination properties. However, accurate quantification requires low defect-related PL spectra.

Chapter 7. Advanced laser processing using a stack of a-Si:H(i) and a-Si:B

7.1 INTRODUCTION

The laser doping process typically includes the deposition of the dopant precursor, followed by its removal after laser irradiation. For a complete cell structure, further extra steps (in addition to the typical laser doping process) are required for the formation of contacts between locally heavily doped regions and metals, including the deposition of passivating dielectric films and its openings. Another approach, which does not have these extra steps, is laser-fired contact, created by a laser through a dielectric film and an aluminium (Al) layer which forms locally Al alloyed p-type silicon [176]. This technique requires precise control of the laser power to avoid metal expulsion and ablation due to the lower evaporation temperature of aluminium than silicon [177]. The most advanced approach is PassDop technology [41], which provides an excellent passivation layer as well as the dopant precursor for the laser doping. This approach is attractive since the dopant precursor is constitutionally part of the solar cell structure and is not required to be removed subsequent to laser doping, therefore the cell fabrication steps can be minimized.

This chapter investigates the effectiveness of layer stacks of intrinsic amorphous silicon (a-Si:H(i)) and boron- (for p-type) rich amorphous silicon (a-Si:B) for producing multi-purpose films capable of providing an excellent passivation and dopant source for effective localized laser doping. Thin films of a-Si:H(i) are already well-known for providing outstanding surface passivation [178, 179], having been successfully applied in many of the highest efficiency silicon solar cells produced to date [33]. An additional layer of a-Si:B acts as the dopant precursor for laser doping, introducing only silicon and boron atoms into the locally melted region during the laser process without any additional/detrimental impurities.

It has been demonstrated previously that sputtered a-Si:H films are capable of excellent surface passivation [180] and doped film [181], and likewise that boron-doped a-Si can be deposited by PECVD [182]. However, for reasons of equipment

availability and reliability, this chapter focuses on intrinsic a-Si films produced by PECVD and boron-doped a-Si films produced by sputtering. Ultimately, a single machine co-optimised for both passivation and dopant precursor depositions will be the most attractive from an industrial processing point of view.

7.2 SAMPLE PREPARATION

High resistivity (~ 100 Ω·cm) p-type FZ crystalline silicon substrates with a thickness of approximately 200 µm were used for this study. All samples were first etched in 25 % TMAH solution at 80 ˚C for 5 minutes to remove surface damage, and RCA cleaned and dipped in a 1 % HF solution prior to the deposition of a-Si films.

An intrinsic amorphous silicon passivation layer (a-Si:H(i)) was deposited on both sides of the substrates via a dual mode Roth and Rau AK 400 PECVD system. The silane (SiH_4) and helium (He) were supplied at 20 and 500 sccm flow rates respectively, the excitation power was 10 W and the deposition temperature was kept at 400 ˚C. To investigate the effect of changing the thickness of a-Si:H(i), different thickness (5, 10 and 20 nm) were deposited by varying the deposition time.

The dopant precursor layer (a-Si:B) was deposited on the single side of PECVD a-Si:H(i) deposited substrates by co-sputtering pure silicon and boron targets using an ATC-2400-V AJA sputter system. Argon (Ar) was used as the plasma source, and the sputter chamber pressure was kept at 4 mTorr. The thickness of a-Si:B was kept at 50 nm, but different percentages of B in a-Si:B were employed to study the effect of the concentration of dopant atoms in a-Si on passivation and laser doping. The deposition power for the silicon target was kept consistent, whereas the deposition power for the boron target and the co-sputtering time were adjusted to provide 10 vol% and 30 vol% of B in a 50 nm a-Si:B layer.

After the deposition of the films, the τ_{eff} was measured with a Sinton WCT120 PCD instrument [183].

A KrF 248 nm excimer laser, with a homogenous-rectangular beam and 25 ns FWHM pulse duration, was then employed to locally heat and melt the stack of a-Si:H(i)/a-Si:B coated substrate, thus introducing dopants into the melt prior to

recrystallization. Single laser pulses were applied, with a range of fluences from 1 to 4 J/cm^2. To characterize the level of the laser doping, small areas of 6 × 2 mm^2 were laser-processed by overlapping 502 × 502 μm^2 beam size laser pulses. The resultant sheet resistance of the doped region was determined by a 4pp measurement using the appropriate calibration factors for the rectangular doped areas created. In addition, qualitative characterization on the laser-doped regions was conducted via the μ-PLS analysis. We also briefly evaluated the recombination properties of the locally laser-processed regions via the uncalibrated PL images.

7.3 SURFACE PASSIVATION OF THE AMORPHOUS SILICON STACK

The passivation effect of the stack of a-Si:H(i) and a-Si:B on top is observed by measuring τ_{eff}, determined at an excess minority carrier density of 1×10^{15} cm^{-3}, prior to laser processing as shown in Figure 7-1. Before depositing the a-Si:B layer (i.e. after a-Si:H(i) only), a maximum lifetime of around 10 ms was observed for the 20 nm a-Si:H(i) coated samples in as-deposited condition. However, immediately prior to depositing the a-Si:B films, we found that the lifetime of all samples, which had been stored at room temperature for five days, approximately halved, indicating considerable degradation of the surface passivation. Effective lifetime was however found to be completely restored after low temperature annealing as reported in Ref. [184], and so this same annealing condition was applied to films subsequent to a-Si:B deposition.

The single side deposition of an a-Si:B layer causes significant degradation of the passivation quality for all intrinsic layer thicknesses, although this was much more severe in the case of the thinner a-Si:H(i) and higher concentration of B in a-Si:B. For the 20 nm a-Si:H(i) case, the lifetime still declines due to the a-Si:B layer, but a reasonable lifetime of around 4.5 ms is maintained regardless of the boron concentration. The corresponding recombination parameter J_0 is approximately 2.5 fA/cm^2 and was derived by fitting the injection dependent τ_{eff} measurement of the sample to full 3-D device simulations using Quokka [127] as shown in Figure 7-2.

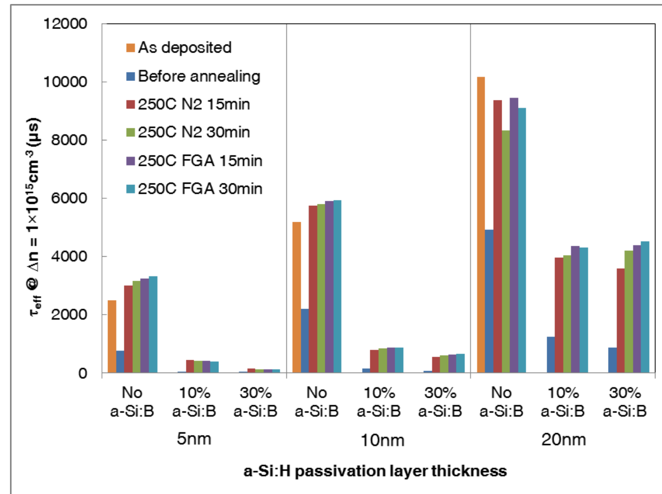

Figure 7-1 Measured τ_{eff} of a-Si:H(i)/a-Si:B coated samples after a-Si:H(i) deposition only, subsequent to 5 days ageing and doped layer deposition, and subsequent to various low temperature annealing conditions. All τ_{eff} values were extracted at the excess carrier density of $1\times10^{15}cm^{-3}$.

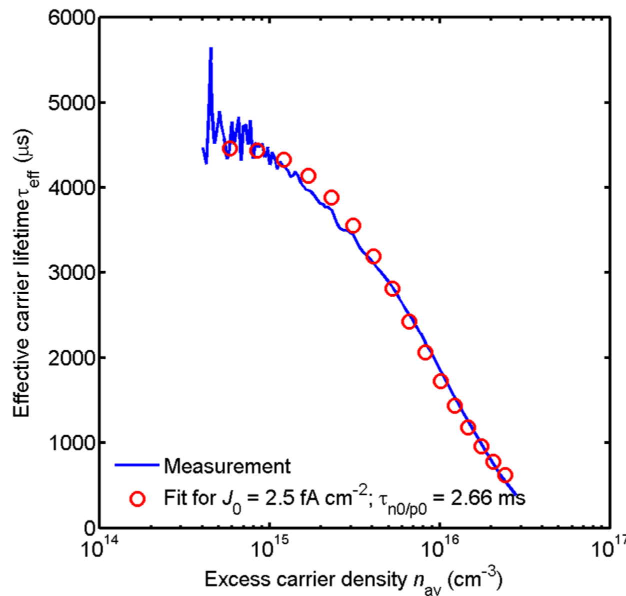

Figure 7-2 The injection dependent τ_{eff} curve for a 20 nm a-Si:H(i) / 30 vol%B a-Si:B coated sample showing J_0 of 2.5 fA/cm^2, derived from Quokka simulation.

Doped a-Si layers have been previously reported to be able to act as a capping layer for the passivating a-Si:H(i) layer [184]. However, a-Si:B capping layers used in this experiment showed the opposite effect, since the film is not optimised for passivation purposes. The current results conclude that a passivating amorphous layer of around 20 nm thickness is a minimum requirement in order to avoid passivation degradation owing to an a-Si:B top layer that has not been optimised for

passivation. Further optimisation of film deposition conditions may result in thinner intrinsic silicon films being found to be resistant to degradation after the application of doped layers.

7.4 LASER-INDUCED DOPING AND DAMAGE THROUGH VARIOUS COMPOSITIONS OF THE A-SI STACK

7.4.1 The sheet resistance measurement

The sheet resistance of laser-processed regions under a variety of stack compositions are demonstrated in Figure 7-3. It is worth noting that a wide range of doping levels are observed for the range of laser pulse fluences 1 to 4 J/cm^2 and the dopant fraction in the dopant precursor layer, with a sheet resistance of around 270 Ω/sq maximum and around 25 Ω/sq minimum. For a range of 5 to 20 nm thickness of a-Si:H(i), the resulting sheet resistances are impacted by the thickness only at low fluence (1 J/cm^2). Above 2 J/cm^2, the sheet resistances are determined from the boron concentration in the a-Si:B layer regardless of the thickness of a-Si:H(i). Obviously, a higher concentration of dopants enables heavier doping. Increasing fluence shows generally lower sheet resistance, but above a fluence of 3 J/cm^2 the value of sheet resistances reaches an apparent minimum, around 60 Ω/sq (10 vol% B film) or 25 Ω/sq (30 vol% B film).

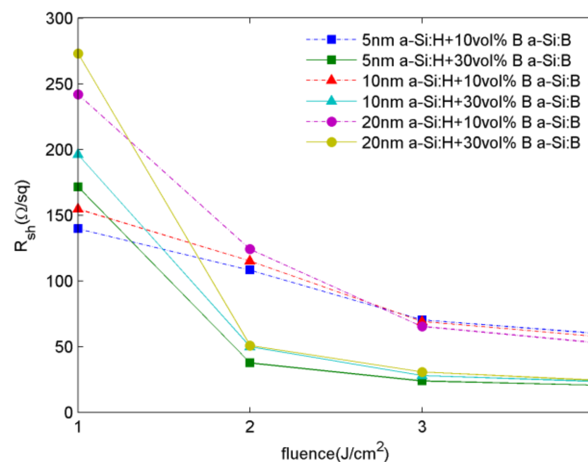

Figure 7-3 Measured sheet resistance as a function of fluence for regions laser-doped from a-Si:H(i)/a-Si:B films. The thickness of the a-Si:H(i) layer was varied from 5 nm to 20 nm. On top of the a-Si:H(i) layer, a 50 nm a-Si:B was deposited with 10 vol% or 30 vol% B.

7.4.2 μ-PLS measurement

Figure 7-4 plots the normalized PL spectra of a variety of laser-doped samples through 20 nm a-Si:H(i)/ a-Si:B, as measured at the centre of the laser-processed region. The presence of a-Si:H(i) is also confirmed from the PL spectra in a range of 900 ~ 1300 nm [185], measured on the passivated surface. Damage and defects caused by laser doping are represented in the PL spectra in the wavelength range of 1200 ~ 1500 nm, and heavy doping via the doping peak. Interestingly, the increase in the fluence shows relatively lower defect-related PL spectra, opposite to the trend shown in Chapter 4. This may be owing to the laser annealing effect on amorphous silicon layers, where laser pulses at low fluence (~ 1 J/cm^2) transform the amorphous silicon layers into polycrystalline layers containing a relatively high number of crystal discontinuities and defects, with little or no melting and recrystallization of the underlying substrate [186]. In contrast, the higher fluences result in deeper melt zones, and possibly also some direct ablation of the amorphous film, which is subsequently recrystallized from the defect-less crystalline substrate. Hence, the resultant luminescent signal of the laser-annealed amorphous silicon layer, and its relationship to laser pulse fluence, is apparent in the longer wavelength 'damage spectrum' region shown in Figure 7-4 [151]. In addition, even though the heavy doping is confirmed from sheet resistance measurements, the evidence for it does not stand out via μ-PLS measurements. This is because of the high defect-related PL spectra in the longer wavelength range > 1200 nm (see 6.6). This prevents an accurate quantification of the dopant density/doping depth.

Comparing the measured PL spectra to the spectra on the TMAH-etched substrate shown in Chapter 4, it appears that their defect-related spectra are quite similar. This is consistent with our findings that the short pulse laser process on rough surfaces induces more laser damage.

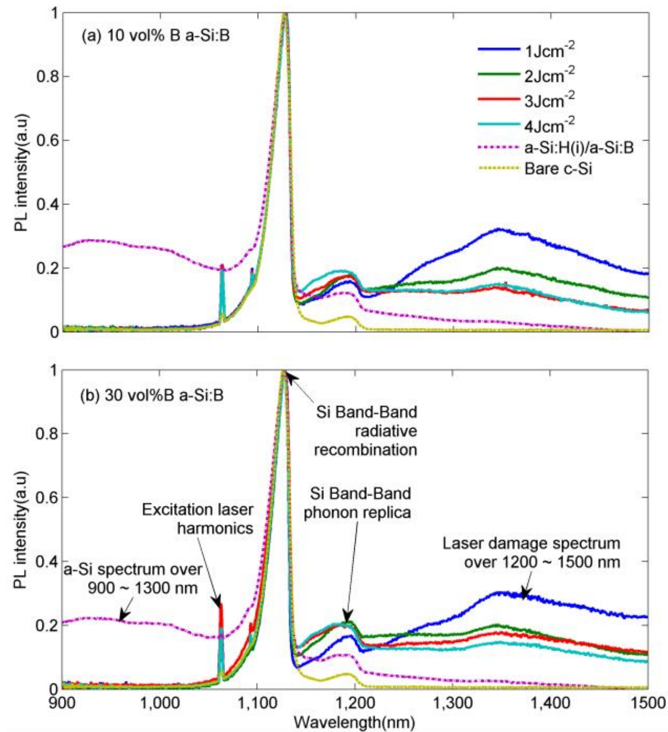

Figure 7-4 Normalized PL spectra on laser-doped samples through (a) 20 nm a-Si:H/ 50 nm 10 vol% B a-Si:B or (b) 20nm a-Si:H/ 50nm 30 vol%B a-Si:B with a fluence range of 1 ~ 4 J/cm^2 at the centre region. Excitation is achieved with a 532 nm laser, and the substrate temperature is 79 K. The spectrum of an unprocessed crystalline Si and a 20nm a-Si:H/a-Si:B coated silicon sample is plotted for comparison.

7.4.3 Uncalibrated PL image measurement

In this section, a simple evaluation of the local recombination properties of laser-doped regions is performed. Figure 7-5 shows the uncalibrated PL images of the laser-doped samples through a stack of 20 nm a-Si:H(i) and 50 nm a-Si:B, with different fractions of doped regions. This is achieved by creating a regular rectangular array of 40 × 40 μm^2 laser-doped ‘spots’ at different pitches. The image was taken after forming gas annealing at 250˚C for 15 minutes, since a significant improvement in effective lifetime has been observed after such an annealing process, as shown in Figure 7-1. Table 7-1 summarizes the average PL counts for each of the fractionally laser-doped arrays, with an estimated decrease in open-circuit voltage ΔV_{oc} that could be expected in the application of photovoltaic devices. The estimation of ΔV_{oc} is conducted based on equation (7.1) derived by Glatthar *et al.* [187]:

$$\Delta V_{oc} = V_T \ln\left(\frac{I_{laser}}{I_{pass}}\right) \quad (7.1)$$

where, V_T is thermal voltage, around 26 mV at room temperature, I_{pass} is PL counts in the passivated area, and I_{laser} is PL counts in the laser-doped region. Assuming that all other factors are optimized, and that device efficiency was theoretically limited by surface recombination alone, then a V_{oc} drop of about 36 mV could be expected in the case of the 0.5 % locally doped area. Given that J_0 of 2.5 fA/cm^2, as shown in Figure 7-2, is generally capable of yielding cells with very high V_{oc}, with a-Si passivated silicon solar cells having been reported with open-circuit voltages of around 750 mV [188, 189], the results obtained in this work for locally laser-doped structures are consistent with fabrication of cells having V_{oc} of 700 mV or over, despite the relatively high recombination activity being observed at the locally laser-doped regions.

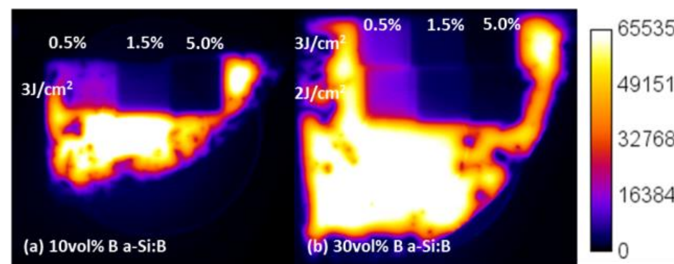

Figure 7-5 Uncalibrated PL images of laser-doped samples through (a) 20 nm a-Si:H/ 10 vol% B a-Si:B or (b) 20 nm a-Si:H/ 30 vol%B a-Si:B after forming gas annealing at 250˚C for 15 minutes. Different fractions of the laser-doped regions are employed, 0.5%, 1.5 % and 5 %.

	Doped fraction	**3 J/cm^2**	**ΔV_{oc} (mV)**	**2 J/cm^2**	**ΔV_{oc} (mV)**
(a)	0 %	65531	0	N/A	
	0.5 %	15944	-36.7		
	1.5 %	6028	-62.0		
	5 %	1697	-94.9		
(b)	0 %	65525	0	65525	0
	0.5 %	9350	-50.6	14996	-38.3
	1.5 %	2290	-87.2	3640	-75.1
	5 %	819	-113.9	1440	-99.2

Table 7-1 The average of PL counts and estimated *Voc* decrease in laser-doped regions shown in Figure 7-5

7.5 CHAPTER SUMMARY

In this chapter, it was demonstrated that a stack of a-Si:H(i) and a-Si:B is able to provide both good surface passivation and a sufficient amount of dopant for the laser doping process. The best result found was for a 20 nm a-Si:H(i) with 30 vol% B a-Si:B, showing τ_{eff} (Δn = 1 × 10^{15} cm^{-3}) of 4.5 ms (corresponding J_0 of 2.5 fA/cm^2) in passivated regions, and a minimum R_{sh} of 25 Ω/sq in the laser-doped regions on high resistivity p-type FZ c-Si substrates.

A good passivation effect is attributed to the a-Si:H(i) layer and requires at least around a 20 nm thickness of it to avoid passivation degradation owing to an a-Si:B top layer that has not been optimised for passivation. The fraction of dopant atoms in the dopant precursor of the a-Si:B layer determines the maximum level of doping. Using μ-PLS, the presence of a-Si layers on the passivated region is confirmed by observing PL spectra in a range of 900 ~ 1300 nm. However, it is not possible to utilize the μ-PLS method to quantify dopant density and recombination properties since a significantly high broad defect-related PL band is observed for all process parameters. Local recombination analysis shows the potential for achieving solar cells with high V_{oc}, with results for the 0.5 % localized doping fraction being consistent with voltages above 700 mV.

Chapter 8. Conclusion

8.1 KEY FINDINGS AND CONTRIBUTIONS

This thesis has presented a novel method for the characterization of localized features utilizing low temperature μ-PLS technique. The method developed overcomes many of the limitations associated with conventional characterization techniques. It allows for a very effective and rapid characterization process for analysing localized features formed by either traditional thermal or emerging laser process techniques. In particular, the advantages and capabilities of this method will contribute to the more practical study of laser parameters in laser-silicon interaction and thus enable the optimization of laser processing for cost-effective fabrication of high-efficiency silicon solar cells. In this concluding chapter, the capabilities of the proposed method are briefly summarised and notes the method's contribution to research on newly discovered or re-identified factors that impact on laser processing.

The primary advantage of the μ-PLS method is that it is able to do spatial characterization in micron-scale without the necessity of having a specific test structure. Utilizing high resolution and the well-established dislocation/defect analysis of μ-PLS measurements at low temperature (~ liquid nitrogen temperature 80 K), the impact of various laser parameters on the formation of dislocations and the doped layer were investigated according to a position within the laser-processed region, in particular at specific locations such as at the boundary/edge of processed and unprocessed regions (see Chapter 4). Key findings of Chapter 4 include:

- The formation of laser-induced dislocation was confirmed by observing the well-known D3/D4 lines, but its density was expected to be low owing to the narrow and low intensity of those two lines.
- There was no evidence of the incorporation of secondary defects and impurities (no D1/D2 lines) during the laser melting cycle.
- Given the same laser parameters, laser processing incorporating dopants creates more defects than laser processing without dopant inclusion. A laser only processed region showed specific low PL peaks (D3/D4 lines)

whereas a laser-doped region showed the broad defect-related PL spectrum in the range 1200 ~ 1500 nm.

- The defect-related PL spectrum increases with pulse fluence/repeat pulses.
- A major source of crystallographic degradation in laser doping occurs at the boundary between the melted and unmelted region. Significantly higher defect-related PL spectra were observed at the pulse edge region and pulse overlapped region.
- Substrate surface preparation can be an important factor impacting on the quality of the laser-doped silicon. A lower defect signal is generally observed for a smoother surface sample.

Another capability of the μ-PLS method is quantification of the dopant density of localized features. The band structure of silicon can be clearly identified via low temperature PL spectrum measurement. It includes not only detection of the dislocation/defect-related deep-levels within the band-gap, but also band-gap shrinkage due to heavy doping. If the absorption depth of the excitation laser is deep enough, the inhomogeneously doped silicon layer emits two distinguishable PL peaks, corresponding to the intrinsic silicon layer and doped layer, respectively. Thus, we decoupled the doping-related PL peak, defined as the 'doping peak' in this thesis, from the measured PL spectra, and observed its characteristics depending on the doping level. This was demonstrated using a set of thermally diffused silicon samples having various Gaussian type doping profiles, as discussed in Chapter 5. The wavelength and PL intensity of the doping peak were correlated to the doping profile-defining key parameters, N_{surf} and z_f, to develop a new method of estimating the Gaussian type doping profile based on the measured PL spectra alone. Key findings of Chapter 5 include:

- There is a linear relationship between the wavelength of the doping peak and N_{surf} on a semi-log plot. The surface dopant density N_{surf} in the range 5×10^{18} to 1×10^{20} cm^{-3} can be estimated from the wavelength of the doping peak in the range from 1150 to 1170 nm.
- Incomplete dopant ionization, enhanced due to low temperature incurs a reduction in the PL intensity of the doping peak, for N_{surf} in the range between 10^{18} and 10^{19} cm^{-3}.

- The corrected PL intensity of the doping peak, after consideration of the fraction of incomplete ionization, exhibits a good linear relationship with z_f, which enables the estimation of z_f values from the doping peak PL intensity.
- Successful estimation of the doping profile was demonstrated by reconstructing it using estimated N_{surf} and z_f from the doping peak analysis.
- The spatial distribution of the N_{surf} and z_f of localized features was characterized by conducting 2-D mappings, showing that N_{surf} is uniformly distributed and is sharply defined, regardless of the feature size, whereas z_f is affected by the feature size and becomes ambiguous as it approaches the feature edge.

Chapter 6 demonstrated that the μ-PLS-based dopant density quantification method is also effective for locally laser-doped features, but showed a different numerical relationship between the doping peak wavelength/PL intensity and N_{surf}/z_f, compared to that of the thermally diffused samples in Chapter 5. Moreover, laterally inhomogeneous doping and a distorted surface morphology due to the overlapping of the non-homogenized laser beams, result in a less accurate estimation. Additionally, the impact of temporal pulse parameters, such as pulse duration and temporal pulse profile shape, on laser doping was investigated in terms of the doping profile and recombination properties. The key findings in Chapter 6 include:

- Laser pulse peak power and pulse duration determines N_{surf} and z_f of the doping profile. Higher pulse peak power associated with shorter pulse duration results in the doped region having a higher N_{surf} with a shallower z_f. On the other hand, lower pulse peak laser power associated with longer pulse duration results in lower N_{surf} with deeper z_f.
- Long pulse laser processing generally results in the formation of fewer recombination active regions. Relatively low values of $J_{0,laser}$ < 1000 fA/cm^2 were achieved with increasing pulse duration, verifying experimentally that pulse duration increase is a very effective way to reduce the recrystallization velocity. Dopant surface accumulation in the doping profile of the long pulse laser-doped samples also support that the long pulse laser leaded slow recrystallization.

- Avoiding abrupt power transitions reduces the formation of recombination active regions. At the same pulse energy and duration, the recombination parameter value $J_{0,laser}$ increases when the pulse profile has an extreme power transition within a few nanoseconds (i.e. zero to peak and vice versa).
- Recombination properties are able to be quantified via μ-PLS analysis. The normalized PL spectrum in the range of 1160 ~ 1200 nm, defined as the 'defect band,' increase with the quantified recombination parameter $J_{0,laser}$ in the range between 500 fA/cm^2 and 5000 fA/cm^2.
- The accurate quantification of doping profiles and recombination properties via the μ-PLS method is not applicable to a heavily damaged sample. Any samples having significantly high defect-related PL spectrum, over 1200 ~ 1500 nm, show big discrepancies between the estimated N_{surf}/z_f from the doping peak analysis and the ECV measured N_{surf}/z_f. In addition, monotonously broad and high defect-related PL spectra are observed regardless of $J_{0,laser}$ when $J_{0,laser} > 5000$ fA/cm^2.

In the last chapter of this thesis, the application of a stack of a-Si:H(i)/a-Si:B as the dopant precursor for advanced laser doping was attempted. This demonstrated that the a-Si stack is able to effectively provide both excellent passivation effects and a pure dopant source, without additional/detrimental impurities.

In conclusion, this thesis has presented a high-resolution spatial characterization method, eminently suitable for laser processing, which is capable of quantifying the doping profile and recombination properties of localized features using low temperature μ-PLS. The method developed in this thesis could be utilised to investigate the major sources of degradation in laser doping and the impact of laser temporal parameters.

8.2 SUGGESTIONS FOR FUTURE WORK

This section summarizes the possibilities for further work to identify problems and/or limitations in improving and expanding the capability of this μ-PLS method. Suggested studies for laser processing are also listed.

- A comprehensive study should be undertaken on the PL spectra of n-type doped silicon. Compared to boron p-type doped silicon, n-type doped silicon shows a very ambiguous luminescent response to the BGN effect. For the same level of heavy doping (> 10^{19} cm^{-3}), boron doped silicon shows very clear responses, like peak shifting and broadening, whereas phosphorus doped silicon shows only marginal change. Therefore, in this thesis the method was limited to boron doped p-type silicon.
- The dopant profiling in this method is limited to either the Gaussian function type or the ERFC type doping profiles. Since this method assumes that the function type is known or at least clearly esimated, the accuracy of the estimation decreases when the function type is unknown or ambiguous. Further work is needed to develop an advanced approach which enables real profiling regardless of the function type of the doping profile.
- Beam homogenization of the green laser system is required for more accurate quantification of the doping profile and recombination properties of laser-doped silicon in Chapter 6. Even if the beam is homogenized, laser processes still induce surface transformation due to the melting and solidification process, as shown in Chapter 4. However, it was not possible to homogenize a beam for the green laser system here due to equipment limitations.
- It would be productive to have further investigation into the laser annealing effect. Reduction in the recombination parameters J_0 after multiple irradiations of long pulses was observed in this thesis, indicating the potential for laser-induced damage recovery via additional laser pulses. While such a phenomenon has both been observed and contradicted in the existing literature, in each case the studies were somewhat limited in scope.

List of publications

[1] H. T. Nguyen, **Y. Han**, M. Ernst, A. Fell, E. Franklin, and D. Macdonald, “Dislocations in laser-doped silicon detected by micro-photoluminescence spectroscopy," *Applied Physics Letters,* vol. 107, no. 2, p. 022101, 2015.

[2] H. T. Nguyen, D. Yan, F. Wang, P. Zheng, **Y. Han**, and D. Macdonald, "Micro-photoluminescence spectroscopy on heavily-doped layers of silicon solar cells," *physica status solidi (RRL) – Rapid Research Letters,* vol. 9, no. 4, pp. 230-235, 2015.

[3] **Y.-J. Han**, E. Franklin, A. Fell, M. Ernst, H. T. Nguyen, and D. Macdonald, "Low-temperature micro-photoluminescence spectroscopy on laser-doped silicon with different surface conditions," *Applied Physics A,* vol. 122, no. 4, pp. 1-10, 2016.

[4] **Y.-J. Han**, E. Franklin, X. Zhang, A. Thomson, and Y. Wan, "Rear passivation and point contacts formation by laser process through stacks of a-Si:H(i) and a-Si:B for high efficiency silicon solar cell," presented at the 32nd European Photovoltaic Solar Energy Conference and Exhibition, Munich, 2016.

[5] **Y.-J Han**, E. Franklin, D. Macdonald, H. T. Nguyen, and D. Yan, "Determination of Dopant Density Profiles of Heavily Boron-Doped Silicon From Low Temperature Microphotoluminescence Spectroscopy," *IEEE Journal of Photovoltaics*, vol. 7, no. 6, pp. 1693-1700, 2017.

[6] T. Rahman, H. T. Nguyen, A. Tarazona, J. Shi, **Y. Han**, E. Franklin, D. Macdonald, and S. A. Boden, "Characterization of Epitaxial Heavily Doped Silicon Regions Formed by Hot-Wire Chemical Vapor Deposition Using Micro-Raman and Microphotoluminescence Spectroscopy," *IEEE Journal of Photovoltaics,* vol. 8, no. 3, pp. 813-819, 2018.

Bibliography

[1] IEA, *World Energy Outlook 2017*. Paris, France: IEA Publications, 2017.

[2] IEA, "Monthly electricity statistics", 2018, [Online]. Available: http://www.iea.org/statistics/monthlystatistics/monthlyelectricitystatistics/. [Acessed: 12, Mar 2018]

[3] BP, "BP Statistical Review of World Energy," London, 2017.

[4] T. Bruckner, I. A. Bashmakov, Y. Mulugetta, H. Chum, A. de la Vega Navarro, J. Edmonds, A. Faaij, B. Fungtammasan, A. Garg, E. hertwich, D. Honnery, D. Infield, M. Kainuma, S. Khennas, S. Kim, H. B. Nimir, K. Riahi, N. Strachan, R. Wiser, and X. Zhang, *Energy System in : Climate Change 2014: Mitigation of Climate Change. Contribution of Working Group III to the Fifth Assessment Report of the Intergovermental Panel on Climate Change*. Cambreidge, United Kingdom and NewYork, NY, USA: Cambridge University Press, 2014.

[5] IEA, *Energy Technology Perspectives 2012: Pathways to a Clean Energy System*. Paris, France: IEA Publications, 2012.

[6] IRENA, "Renewable capacity statistics 2018," International Renewable Energy Agency, Abu Dhabi,2018.

[7] IRENA, "Renewable Power Generation Costs in 2017," International Renewable Energy Agency, Abu Dhabi, 2018.

[8] G. Parkinson, "Stunning new low for solar PV as even IEA hails "age of solar"", 2017, [Online]. Available: https://reneweconomy.com.au/stunning-new-low-for-solar-pv-as-even-iea-hails-age-of-solar-43509/. [Acessed: 15 Jun]

[9] M. A. Green, Y. Hishikawa, E. D. Dunlop, D. H. Levi, J. Hohl-Ebinger, and A. W. Y. Ho-Baillie, "Solar cell efficiency tables (version 51)," *Progress in Photovoltaics: Research and Applications,* vol. 26, no. 1, pp. 3-12, 2018.

[10] M. A. Green and A. Ho-Baillie, "Perovskite Solar Cells: The Birth of a New Era in Photovoltaics," *ACS Energy Letters,* vol. 2, no. 4, pp. 822-830, 2017.

[11] R. M. Geisthardt, M. Topič, and J. R. Sites, "Status and Potential of CdTe Solar-Cell Efficiency," *IEEE Journal of Photovoltaics,* vol. 5, no. 4, pp. 1217-1221, 2015.

[12] J. M. Burst, J. N. Duenow, D. S. Albin, E. Colegrove, M. O. Reese, J. A. Aguiar, C. S. Jiang, M. K. Patel, M. M. Al-Jassim, D. Kuciauskas, S. Swain, T. Ablekim, K. G. Lynn, and W. K. Metzger, "CdTe solar cells with open-circuit voltage breaking the 1 V barrier," *Nature Energy,* vol. 1, p. 16015, 2016.

[13] F. ISE, "Photovoltaics Report", 2018, [Online]. Available: https://www.ise.fraunhofer.de/content/dam/ise/de/documents/publications/studies/Photovoltaics-Report.pdf. [Acessed: 12 Mar 2018]

[14] A. Polman, M. Knight, E. C. Garnett, B. Ehrler, and W. C. Sinke, "Photovoltaic materials: Present efficiencies and future challenges," *Science,* vol. 352, no. 6283, 2016.

[15] U. Pillai, "Drivers of cost reduction in solar photovoltaics," *Energy Economics,* vol. 50, pp. 286-293, 2015.

[16] M. A. Green, "The Passivated Emitter and Rear Cell (PERC): From conception to mass production," *Solar Energy Materials and Solar Cells,* vol. 143, pp. 190-197, 2015.

[17] ITRPV, "International Technology Roadmap for Photovoltaic Results 2017," 2018.

[18] A. Wang, J. Zhao, and M. A. Green, "24% efficient silicon solar cells," *Applied Physics Letters,* vol. 57, no. 6, pp. 602-604, 1990.

[19] R. M. Swanson, "Point-Contact Solar-Cells - Modeling and Experiment," (in English), *Sol. Cells.,* vol. 17, no. 1, pp. 85-118, 1986.

[20] E. Franklin, K. Fong, K. McIntosh, A. Fell, A. Blakers, T. Kho, D. Walter, D. Wang, N. Zin, M. Stocks, E.-C. Wang, N. Grant, Y. Wan, Y. Yang, X. Zhang, Z. Feng, and P. J. Verlinden, "Design, fabrication and characterisation of a 24.4% efficient interdigitated back contact solar cell," *Progress in Photovoltaics: Research and Applications,* vol. 24, no. 4, pp. 411-427, 2016.

[21] M. Ernst, E. Franklin, A. Fell, K. Fong, D. Walter, E.-C. Wang, T. Kho, and A. Blakers, "Fabrication of a 22.8% Efficient Back Contact Solar Cell With

Localized Laser-Doping," *physica status solidi (a),* vol. 214, no. 11, p. 1700318, 2017.

[22] M. Dahlinger, K. Carstens, E. Hoffmann, R. Zapf-Gottwick, and J. H. Werner, "23.2% laser processed back contact solar cell: fabrication, characterization and modeling," *Progress in Photovoltaics: Research and Applications,* vol. 25, no. 2, pp. 192-200, 2017.

[23] B. Hallam, A. Urueña, R. Russell, M. Aleman, M. Abbott, C. Dang, S. Wenham, L. Tous, and J. Poortmans, "Efficiency enhancement of i-PERC solar cells by implementation of a laser doped selective emitter," *Solar Energy Materials and Solar Cells,* vol. 134, no. Supplement C, pp. 89-98, 2015.

[24] M. Ernst, D. Walter, A. Fell, B. Lim, and K. Weber, "Efficiency Potential of P-Type Al_2O_3/SiN_x Passivated PERC Solar Cells With Locally Laser-Doped Rear Contacts," *IEEE Journal of Photovoltaics,* vol. 6, no. 3, pp. 624-631, 2016.

[25] M. A. Green, "Enhancement of Schottky solar cell efficiency above its semiempirical limit," *Applied Physics Letters,* vol. 27, no. 5, pp. 287-288, 1975.

[26] M. A. Green, A. W. Blakers, J. Shi, E. M. Keller, and S. R. Wenham, "19.1% efficient silicon solar cell," *Applied Physics Letters,* vol. 44, no. 12, pp. 1163-1164, 1984.

[27] A. W. Blakers, A. Wang, A. M. Milne, J. Zhao, and M. A. Green, "22.8% efficient silicon solar cell," *Applied Physics Letters,* vol. 55, no. 13, pp. 1363-1365, 1989.

[28] J. Zhao, A. Wang, and M. A. Green, "24·5% Efficiency silicon PERT cells on MCZ substrates and 24·7% efficiency PERL cells on FZ substrates," *Progress in Photovoltaics: Research and Applications,* vol. 7, no. 6, pp. 471-474, 1999.

[29] M. A. Green, "The path to 25% silicon solar cell efficiency: History of silicon cell evolution," *Progress in Photovoltaics: Research and Applications,* vol. 17, no. 3, pp. 183-189, 2009.

[30] R. J. Schwartz and M. D. Lammert, "Silicon solar cells for high concentration applications," in *International Electron Devices Meeting*, 1975, vol. 21, pp. 350-352.

[31] R. A. Sinton, K. Young, J. Y. Gan, and R. M. Swanson, "27.5-percent silicon concentrator solar cells," *IEEE Electron Device Letters,* vol. 7, no. 10, pp. 567-569, 1986.

[32] M. D. Lammert and R. J. Schwartz, "The interdigitated back contact solar cell: A silicon solar cell for use in concentrated sunlight," *IEEE Transactions on Electron Devices,* vol. 24, no. 4, pp. 337-342, 1977.

[33] K. Yoshikawa, H. Kawasaki, W. Yoshida, T. Irie, K. Konishi, K. Nakano, T. Uto, D. Adachi, M. Kanematsu, H. Uzu, and K. Yamamoto, "Silicon heterojunction solar cell with interdigitated back contacts for a photoconversion efficiency over 26%," *Nature Energy,* vol. 2, p. 17032, 2017.

[34] D. D. Smith, G. Reich, M. Baldrias, M. Reich, N. Boitnott, and G. Bunea, "Silicon solar cells with total area efficiency above 25 %," in *43rd IEEE Photovoltaic Specialists Conference* Portland, 2016, pp. 3351-3355.

[35] P. Engelhart, S. Hermann, T. Neubert, H. Plagwitz, R. Grischke, R. Meyer, U. Klug, A. Schoonderbeek, U. Stute, and R. Brendel, "Laser ablation of SiO2 for locally contacted Si solar cells with ultra-short pulses," *Progress in Photovoltaics: Research and Applications,* vol. 15, no. 6, pp. 521-527, 2007.

[36] K. Mangersnes, S. E. Foss, and A. Thøgersen, "Damage free laser ablation of SiO2 for local contact opening on silicon solar cells using an a-Si:H buffer layer," *Journal of Applied Physics,* vol. 107, no. 4, p. 043518, 2010.

[37] D. Walter, A. Fell, E. Franklin, D. Wang, K. Fong, T. Kho, K. J. Weber, and A. W. Blakers, "Damage-free ultraviolet nanosecond laser ablation for high efficiency back contact solar cell fabrication," *Solar Energy Materials and Solar Cells,* vol. 136, pp. 1-10, 2015.

[38] A. Toshimitsu, N. Takahiro, and M. Satoru, "Two-Step Doping Using Excimer Laser in Boron Doping of Silicon," *Japanese Journal of Applied Physics,* vol. 31, no. 12S, p. 4437, 1992.

[39] V. C. Lo, Y. W. Wong, H. C. Cho, Y. Q. Chen, S. M. Ho, P. W. Chan, and K. Y. Tong, "Excimer laser assisted spin-on doping of boron into silicon," *Semicond. Sci. Tech.,* vol. 11, no. 9, p. 1285, 1996.

[40] B. Hallam, S. Wenham, C. M. Chong, A. Sugianto, M. Ly, M. Edwards, D. Jordan, and P. Fath, "Record large area P-type CZ production cell efficiency of 19.3% based on LDSE technology," *IEEE Journal of Photovoltaics,* vol. 1, no. 1, pp. 43-48, 2011.

[41] D. Suwito, U. Jager, J. Benick, S. Janz, M. Hermle, and S. W. Glunz, "Industrially Feasible Rear Passivation and Contacting Scheme for High-Efficiency n-Type Solar Cells Yielding a V_{oc} of 700 mV," *IEEE Transactions on Electron Devices,* vol. 57, no. 8, pp. 2032-2036, 2010.

[42] B. Steinhauser, M. Kamp, A. A. Brand, U. Jäger, J. Bartsch, J. Benick, and M. Hermle, "High-Efficiency n-Type Silicon Solar Cells: Advances in PassDop Technology and NiCu Plating on Boron Emitter," *IEEE Journal of Photovoltaics,* vol. 6, no. 2, pp. 419-425, 2016.

[43] A. Fell, S. Surve, E. Franklin, and K. J. Weber, "Characterization of Laser-Doped Localized p-n Junctions for High Efficiency Silicon Solar Cells," *IEEE Transactions on Electron Devices,* vol. 61, no. 6, pp. 1943-1949, 2014.

[44] M. Ernst, A. Fell, E. Franklin, and K. J. Weber, "Characterization of Recombination Properties and Contact Resistivity of Laser-Processed Localized Contacts From Doped Silicon Nanoparticle Ink and Spin-On Dopants," *IEEE Journal of Photovoltaics,* vol. 7, no. 2, pp. 471-478, 2017.

[45] D. K. Schroder and D. L. Meier, "Solar cell contact resistance - A review," *IEEE Transactions on Electron Devices,* vol. 31, no. 5, pp. 637-647, 1984.

[46] P. Gundel, F. D. Heinz, M. C. Schubert, J. A. Giesecke, and W. Warta, "Quantitative carrier lifetime measurement with micron resolution," *Journal of Applied Physics,* vol. 108, no. 3, p. 033705, 2010.

[47] F. D. Heinz, P. Gundel, W. Warta, and M. C. Schubert, "Doping Density in Silicon and Solar Cells Analyzed With Micrometer Resolution," *IEEE Journal of Photovoltaics,* vol. 3, no. 1, pp. 341-347, 2013.

[48] A. Roigé, J. Alvarez, A. Jaffré, T. Desrues, D. Muñoz, I. Martín, R. Alcubilla, and J.-P. Kleider, "Effects of photon reabsorption phenomena in confocal micro-photoluminescence measurements in crystalline silicon," *Journal of Applied Physics,* vol. 121, no. 6, p. 063101, 2017.

[49] M. Tajima, "Spectroscopy and Topography of Deep-Level Luminescence in Photovoltaic Silicon," *IEEE Journal of Photovoltaics,* vol. 4, no. 6, pp. 1452-1458, 2014.

[50] P. Gundel, M. C. Schubert, W. Kwapil, J. Schön, M. Reiche, H. Savin, M. Yli-Koski, J. A. Sans, G. Martinez-Criado, W. Seifert, W. Warta, and E. R. Weber, "Micro-photoluminescence spectroscopy on metal precipitates in

silicon," *physica status solidi (RRL) – Rapid Research Letters,* vol. 3, no. 7-8, pp. 230-232, 2009.

[51] M. Tajima, Y. Iwata, F. Okayama, H. Toyota, H. Onodera, and T. Sekiguchi, "Deep-level photoluminescence due to dislocations and oxygen precipitates in multicrystalline Si," *Journal of Applied Physics,* vol. 111, no. 11, p. 113523, 2012.

[52] A. Fell, D. Walter, S. Kluska, E. Franklin, and K. Weber, "Determination of Injection Dependent Recombination Properties of Locally Processed Surface Regions," *Energy Procedia,* vol. 38, pp. 22-31, 2013.

[53] H. Booth, "Laser Processing in Industrial Solar Module Manufacturing," *Journal of Laser Micro/Nanoengineering,* vol. 5, no. 3, 2010.

[54] Dricus, "Half cut solar cells: new standard in product differentiation?", 2016, [Online]. Available: http://sinovoltaics.com/solar-cells/half-cut-solar-cells-the-new-standard/. [Acessed: 30 Jun]

[55] A. Metz, D. Adler, S. Bagus, H. Blanke, M. Bothar, E. Brouwer, S. Dauwe, K. Dressler, R. Droessler, T. Droste, M. Fiedler, Y. Gassenbauer, T. Grahl, N. Hermert, W. Kuzminski, A. Lachowicz, T. Lauinger, N. Lenck, M. Manole, M. Martini, R. Messmer, C. Meyer, J. Moschner, K. Ramspeck, P. Roth, R. Schönfelder, B. Schum, J. Sticksel, K. Vaas, M. Volk, and K. Wangemann, "Industrial high performance crystalline silicon solar cells and modules based on rear surface passivation technology," *Solar Energy Materials and Solar Cells,* vol. 120, pp. 417-425, 2014.

[56] A. Hauser, G. Hahn, M. Spiegel, H. Feist, O. Breitenstein, J. P. Rakotoniaina, P. Fath, and E. Bucher, "Comparison of different techniques for edge isolation," in *17th European Photovoltaic Solar Energy Conference and Exhibition*, Munich, 2001.

[57] C. M. Chong, S. R. Wenham, and M. A. Green, "High-efficiency, laser grooved, buried contact silicon solar cells," *Applied Physics Letters,* vol. 52, no. 5, pp. 407-409, 1988.

[58] O. Schultz-Wittmann, S. Glunz, W. Warta, R. Preu, A. Grohe, M. Köber, G. P Willeke, R. Russel, J. Fernandez, C. Morilla, R. Bueno, and I. Vincuería, "High-efficiency solar cells wth laser-grooved buried contact front and laser-fired rear for industrial production," in *21st European Photovoltaic Solar Energy Conference and Exhibition*, Dresden, 2006.

[59] M. A. Green, "Self-consistent optical parameters of intrinsic silicon at 300 K including temperature coefficients," *Solar Energy Materials and Solar Cells,* vol. 92, no. 11, pp. 1305-1310, 2008.

[60] G. E. J. Jr. and D. H. Lowndes, "Measurements of the optical properties of liquid silicon and germanium using nanosecond time-resolved ellipsometry," *Applied Physics Letters,* vol. 51, no. 5, pp. 352-354, 1987.

[61] S. K. F. Monika, "Optical properties of liquid silicon: the integral equation approach," *Journal of Physics: Condensed Matter,* vol. 12, no. 19, p. 4341, 2000.

[62] H. R. Shanks, P. D. Maycock, P. H. Sidles, and G. C. Danielson, "Thermal Conductivity of Silicon from 300 to 1400 K," *Physical Review,* vol. 130, no. 5, pp. 1743-1748, 1963.

[63] Y. Katsuhiro, A. Toshio, and T. Shin-ichiro, "Thermal Diffusivity of Crystalline and Liquid Silicon and an Anomaly at Melting," *Japanese Journal of Applied Physics,* vol. 30, no. 10R, p. 2423, 1991.

[64] H. T. Nguyen, S. C. Baker-Finch, and D. Macdonald, "Temperature dependence of the radiative recombination coefficient in crystalline silicon from spectral photoluminescence," *Applied Physics Letters,* vol. 104, no. 11, p. 112105, 2014.

[65] J. Dziewior and W. Schmid, "Auger coefficients for highly doped and highly excited silicon," *Applied Physics Letters,* vol. 31, no. 5, pp. 346-348, 1977.

[66] A. Richter, S. W. Glunz, F. Werner, J. Schmidt, and A. Cuevas, "Improved quantitative description of Auger recombination in crystalline silicon," *Physical Review B,* vol. 86, no. 16, p. 165202, 2012.

[67] J. d. Alamo, S. Swirhun, and R. M. Swanson, "Simultaneous measurement of hole lifetime, hole mobility and bandgap narrowing in heavily doped n-type silicon," in *International Electron Devices Meeting*, 1985, vol. 31, pp. 290-293.

[68] J. del Alamo, S. Swirhun, and R. M. Swanson, "Measuring and modeling minority carrier transport in heavily doped silicon," *Solid-State Electronics,* vol. 28, no. 1, pp. 47-54, 1985.

[69] M. A. Green, "Intrinsic concentration, effective densities of states, and effective mass in silicon," *Journal of Applied Physics,* vol. 67, no. 6, pp. 2944-2954, 1990.

[70] D. Yan and A. Cuevas, "Empirical determination of the energy band gap narrowing in highly doped n+ silicon," *Journal of Applied Physics,* vol. 114, no. 4, p. 044508, 2013.

[71] D. Yan and A. Cuevas, "Empirical determination of the energy band gap narrowing in p+ silicon heavily doped with boron," *Journal of Applied Physics,* vol. 116, no. 19, p. 194505, 2014.

[72] A. Schenk, "Finite-temperature full random-phase approximation model of band gap narrowing for silicon device simulation," *Journal of Applied Physics,* vol. 84, no. 7, pp. 3684-3695, 1998.

[73] P. P. Altermatt, A. Schenk, and G. Heiser, "A simulation model for the density of states and for incomplete ionization in crystalline silicon. I. Establishing the model in Si:P," *Journal of Applied Physics,* vol. 100, no. 11, p. 113714, 2006.

[74] P. P. Altermatt, A. Schenk, B. Schmithüsen, and G. Heiser, "A simulation model for the density of states and for incomplete ionization in crystalline silicon. II. Investigation of Si:As and Si:B and usage in device simulation," *Journal of Applied Physics,* vol. 100, no. 11, p. 113715, 2006.

[75] J. E. Lang, F. L. Madarasz, and P. M. Hemenger, "Temperature dependent density of states effective mass in nonparabolic p-type silicon," *Journal of Applied Physics,* vol. 54, no. 6, pp. 3612-3612, 1983.

[76] J. M. Fairfield and G. H. Schwuttke, "Silicon diodes made by laser irradiation," *Solid-State Electron,* vol. 11, no. 12, pp. 1175-1176, 1968.

[77] T. F. Deutsch, J. C. C. Fan, G. W. Turner, R. L. Chapman, D. J. Ehrlich, and R. M. O. Jr., "Efficient Si solar cells by laser photochemical doping," *Applied Physics Letters,* vol. 38, no. 3, pp. 144-146, 1981.

[78] E. Fogarassy, R. Stuck, J. J. Grob, and P. Siffert, "Silicon solar cells realized by laser induced diffusion of vacuum-deposited dopants," *Journal of Applied Physics,* vol. 52, no. 2, pp. 1076-1082, 1981.

[79] S. J. Eisele, T. C. Röder, J. R. Köhler, and J. H. Werner, "18.9% efficient full area laser doped silicon solar cell," *Applied Physics Letters,* vol. 95, no. 13, p. 133501, 2009.

[80] R. F. Wood and G. E. Giles, "Macroscopic theory of pulsed-laser annealing. I. Thermal transport and melting," *Physical Review B,* vol. 23, no. 6, pp. 2923-2942, 1981.

[81] J. R. Meyer, F. J. Bartoli, and M. R. Kruer, "Optical heating in semiconductors," *Physical Review B,* vol. 21, no. 4, pp. 1559-1568, 1980.

[82] J. R. Meyer, M. R. Kruer, and F. J. Bartoli, "Optical heating in semiconductors: Laser damage in Ge, Si, InSb, and GaAs," *Journal of Applied Physics,* vol. 51, no. 10, pp. 5513-5522, 1980.

[83] X. Wang, Z. H. Shen, J. Lu, and X. W. Ni, "Laser-induced damage threshold of silicon in millisecond, nanosecond, and picosecond regimes," *Journal of Applied Physics,* vol. 108, no. 3, p. 033103, 2010.

[84] D. K. Schroder, R. N. Thomas, and J. C. Swartz, "Free carrier absorption in silicon," *IEEE Transactions on Electron Devices,* vol. 25, no. 2, pp. 254-261, 1978.

[85] K. Hiroshi, "Diffusion Coefficients of Impurities in Silicon Melt," *Japanese Journal of Applied Physics,* vol. 2, no. 4, p. 212, 1963.

[86] C. W. White, S. R. Wilson, B. R. Appleton, F. W. Young, and J. Narayan, "Supersaturated substitutional alloys in silicon formed by ion implantation and laser annealing," in *Laser and Electron Beam Processing of Materials*, C. W. White and P. S. Peercy, Eds.: Academic Press, 1980, pp. 111-116.

[87] E. Fogarassy, R. Stuck, J.J, A. Grob, and P. Siffert, "Solubility limit of dopants in laser-treated silicon," in *Laser and Electron Beam Processing of Materials*, C. W. White and P. S. Peercy, Eds.: Academic Press, 1980, pp. 117-123.

[88] G. B. Turner, D. Tarrant, G. Pollock, R. Pressley, and R. Press, "Solar cells made by laser-induced diffusion directly from phosphine gas," *Applied Physics Letters,* vol. 39, no. 12, pp. 967-969, 1981.

[89] R. Stuck, E. Fogarassy, J. C. Muller, M. Hodeau, A. Wattiaux, and P. Siffert, "Laser-induced diffusion by irradiation of silicon dipped into an organic solution of the dopant," *Applied Physics Letters,* vol. 38, no. 9, pp. 715-717, 1981.

[90] D. Kray, A. Fell, S. Hopman, K. Mayer, G. P. Willeke, and S. W. Glunz, "Laser Chemical Processing (LCP)—A versatile tool for microstructuring applications," *Applied Physics A,* vol. 93, no. 1, p. 99, 2008.

[91] F. Colville, "Laser-assisted selective emitters and the role of laser doping," *Photovoltaics International,* vol. 5, no. 6, pp. 1-7, 2009.

[92] S. Toshiyuki and U. Setsuo, "Analysis of Dopant Diffusion in Molten Silicon Induced by a Pulsed Excimer Laser," *Japanese Journal of Applied Physics,* vol. 26, no. 7A, p. L1208, 1987.

[93] M. Ametowobla, "Characterization of a Laser Doping Process for Crystalline Silicon Solar Cells," Universit• at Stuttgart, 2010.

[94] M. Dahlinger, B. Bazer-Bachi, T. C. Röder, J. R. Köhler, R. Zapf-Gottwick, and J. H. Werner, "22.0% Efficient Laser Doped back Contact Solar Cells," *Energy Procedia,* vol. 38, pp. 250-253, 2013.

[95] L. Xu, K. Weber, S. P. Phang, A. Fell, F. Brink, D. Yan, X. Yang, E. Franklin, and H. Chen, "Secondary Electron Microscopy Dopant Contrast Image (SEMDCI) for Laser Doping," *IEEE Journal of Photovoltaics,* vol. 3, no. 2, pp. 762-768, 2013.

[96] I. Martín, P. Ortega, M. Colina, A. Orpella, G. López, and R. Alcubilla, "Laser processing of Al2O3/a-SiCx:H stacks: a feasible solution for the rear surface of high-efficiency p-type c-Si solar cells," *Progress in Photovoltaics: Research and Applications,* vol. 21, no. 5, pp. 1171-1175, 2013.

[97] B. Paviet-Salomon, S. Gall, R. Monna, S. Manuel, A. Slaoui, L. Vandroux, R. Hida, and S. Dechenaux, "Laser doping using phosphorus-doped silicon nitrides," *Energy Procedia,* vol. 8, pp. 700-705, 2011.

[98] F. M. Smits, "Measurement of sheet resistivities with the four-point probe," *The Bell System Technical Journal,* vol. 37, no. 3, pp. 711-718, 1958.

[99] D. B. M. Klaassen, "A unified mobility model for device simulation—I. Model equations and concentration dependence," *Solid-State Electronics,* vol. 35, no. 7, pp. 953-959, 1992.

[100] D. B. M. Klaassen, "A unified mobility model for device simulation—II. Temperature dependence of carrier mobility and lifetime," *Solid-State Electronics,* vol. 35, no. 7, pp. 961-967, 1992.

[101] T. Ambridge and M. M. Faktor, "An automatic carrier concentration profile plotter using an electrochemical technique," *Journal of Applied Electrochemistry,* vol. 5, no. 4, pp. 319-328, 1975.

[102] T. Ambridge, C. R. Elliott, and M. M. Faktor, "The electrochemical characterization of n-type gallium arsenide," *Journal of Applied Electrochemistry,* vol. 3, no. 1, pp. 1-15, 1973.

[103] J. S. Fletcher and J. C. Vickerman, "Secondary Ion Mass Spectrometry: Characterizing Complex Samples in Two and Three Dimensions," *Analytical Chemistry,* vol. 85, no. 2, pp. 610-639, 2013.

[104] O. Akiyoshi, H. Kenji, H. Koyo, N. Yoshiyuki, T. Yu, K. Athapol, and F. Takashi, "Laser-Doping Technique Using Ultraviolet Laser for Shallow Doping in Crystalline Silicon Solar Cell Fabrication," *Japanese Journal of Applied Physics,* vol. 48, no. 7R, p. 071201, 2009.

[105] T. Röder, P. Grabitz, S. Eisele, C. Wagner, J. R. Köhler, and J. H. Werner, "0.4% absolute efficiency gain of industrial solar cells by laser doped selective emitter," in *34th IEEE Photovoltaic Specialists Conference* Philadelphia, 2009, pp. 000871-000873.

[106] S. Kato, T. Nagahori, and S. Matsumoto, "ArF excimer laser doping of boron into silicon," *Journal of Applied Physics,* vol. 62, no. 9, pp. 3656-3659, 1987.

[107] Z. Hameiri, L. Mai, T. Puzzer, and S. R. Wenham, "Influence of laser power on the properties of laser doped solar cells," *Solar Energy Materials and Solar Cells,* vol. 95, no. 4, pp. 1085-1094, 2011.

[108] Z. Hameiri, T. Puzzer, L. Mai, A. B. Sproul, and S. R. Wenham, "Laser induced defects in laser doped solar cells," *Progress in Photovoltaics: Research and Applications,* vol. 19, no. 4, pp. 391-405, 2011.

[109] C.-Y. Jen, G. Tulsyan, and C. Richter, "Demonstration of high-resolution doping profile mapping using terahertz time domain spectroscopy with electrochemical anodization," in *SPIE OPTO*, San Francisco, 2015, vol. 9362, pp. 93620R1-93620R8.

[110] C. Y. Jen and C. Richter, "Doping Profile Recognition Applied to Silicon Photovoltaic Cells Using Terahertz Time-Domain Spectroscopy," *IEEE Transactions on Terahertz Science and Technology,* vol. 4, no. 5, pp. 560-567, 2014.

[111] T. H. P. Chang and W. C. Nixon, "Electron beam induced potential contrast on unbiased planar transistors," *Solid-State Electronics,* vol. 10, no. 7, pp. 701-704, 1967.

[112] D. D. Perovic, M. R. Castell, A. Howie, C. Lavoie, T. Tiedje, and J. S. W. Cole, "Field-emission SEM imaging of compositional and doping layer semiconductor superlattices," *Ultramicroscopy,* vol. 58, no. 1, pp. 104-113, 1995.

[113] J. I. Goldstein, D. E. Newbury, J. R. Michael, N. W. M. Ritchie, J. H. J. Scott, and D. C. Joy, *Scanning Electron Microscopy and X-Ray Microanalysis*. Springer New York, 2017.

[114] S. Y. Lim, S. P. Phang, T. Trupke, A. Cuevas, and D. Macdonald, "Dopant concentration imaging in crystalline silicon wafers by band-to-band photoluminescence," *Journal of Applied Physics,* vol. 110, no. 11, p. 113712, 2011.

[115] S. Y. Lim, M. Forster, X. Zhang, J. Holtkamp, M. C. Schubert, A. Cuevas, and D. Macdonald, "Applications of Photoluminescence Imaging to Dopant and Carrier Concentration Measurements of Silicon Wafers," *IEEE Journal of Photovoltaics,* vol. 3, no. 2, pp. 649-655, 2013.

[116] D. Kane and R. Swanson, "Measurement of the emitter saturation current by a contactless photoconductivity decay method," in *18th IEEE Photovoltaic Specialists Conference*, Las Vegas, 1985, pp. 578-583.

[117] A. Cuevas, "The effect of emitter recombination on the effective lifetime of silicon wafers," *Solar Energy Materials and Solar Cells,* vol. 57, no. 3, pp. 277-290, 1999.

[118] A. Thomson, N. Grant, K. F. Chern, and T. Kho, "Improved Diffused-region Recombination-current Pre-factor Analysis," *Energy Procedia,* vol. 55, pp. 141-148, 2014.

[119] S. Martinuzzi and M. Stemmer, "Mapping of defects and their recombination strenght by a light-beam-induced current in silicon wafers," *Materials Science and Engineering: B,* vol. 24, no. 1, pp. 152-158, 1994.

[120] J. Carstensen, G. Popkirov, J. Bahr, and H. Föll, "CELLO: an advanced LBIC measurement technique for solar cell local characterization," *Solar Energy Materials and Solar Cells,* vol. 76, no. 4, pp. 599-611, 2003.

[121] M. Breitwieser, F. D. Heinz, A. Büchler, M. Kasemann, J. Schön, W. Warta, and M. C. Schubert, "Analysis of solar cell cross sections with micro-light beam induced current (µLBIC)," *Solar Energy Materials and Solar Cells,* vol. 131, pp. 124-128, 2014.

[122] O. Breitenstein, "Nondestructive local analysis of current–voltage characteristics of solar cells by lock-in thermography," *Solar Energy Materials and Solar Cells,* vol. 95, no. 10, pp. 2933-2936, 2011.

[123] K. Ramspeck, K. Bothe, D. Hinken, B. Fischer, J. Schmidt, and R. Brendel, "Recombination current and series resistance imaging of solar cells by combined luminescence and lock-in thermography," *Applied Physics Letters,* vol. 90, no. 15, p. 153502, 2007.

[124] T. Trupke, R. A. Bardos, M. C. Schubert, and W. Warta, "Photoluminescence imaging of silicon wafers," *Applied Physics Letters,* vol. 89, no. 4, p. 044107, 2006.

[125] G. Markus, H. Jonas, K. Martin, G. Johannes, W. Wilhelm, and R. Stefan, "Spatially resolved determination of dark saturation current and series resistance of silicon solar cells," *physica status solidi (RRL) – Rapid Research Letters,* vol. 4, no. 1-2, pp. 13-15, 2010.

[126] T. Trupke and R. A. Bardos, "Photoluminescence: a surprisingly sensitive lifetime technique," in *31st IEEE Photovoltaic Specialists Conference*, Lake Buena, 2005, pp. 903-906.

[127] A. Fell, "A Free and Fast Three-Dimensional/Two-Dimensional Solar Cell Simulator Featuring Conductive Boundary and Quasi-Neutrality Approximations," *IEEE Transactions on Electron Devices,* vol. 60, no. 2, pp. 733-738, 2013.

[128] K. R. McIntosh and S. C. Baker-Finch, "OPAL 2: Rapid optical simulation of silicon solar cells," in *38th IEEE Photovoltaic Specialists Conference*, Austin, 2012, pp. 000265-000271.

[129] J. Wagner, "Photoluminescence and excitation spectroscopy in heavily doped n- and p-type silicon," *Physical Review B,* vol. 29, no. 4, pp. 2002-2009, 1984.

[130] J. Wagner, "Band-gap narrowing in heavily doped silicon at 20 and 300 K studied by photoluminescence," *Physical Review B,* vol. 32, no. 2, pp. 1323-1325, 1985.

[131] M. Suezawa, Y. Sasaki, and K. Sumino, "Dependence of Photoluminescence on Temperature in Dislocated Silicon Crystals," *physica status solidi (a),* vol. 79, no. 1, pp. 173-181, 1983.

[132] R. Sauer, J. Weber, J. Stolz, E. R. Weber, K. H. Küsters, and H. Alexander, "Dislocation-related photoluminescence in silicon," (in English), *Appl. Phys. A-Mater,* vol. 36, no. 1, pp. 1-13, 1985.

[133] P. J. Dean, J. R. Haynes, and W. F. Flood, "New Radiative Recombination Processes Involving Neutral Donors and Acceptors in Silicon and Germanium," *Physical Review,* vol. 161, no. 3, pp. 711-729, 1967.

[134] H. T. Nguyen, F. E. Rougieux, B. Mitchell, and D. Macdonald, "Temperature dependence of the band-band absorption coefficient in crystalline silicon from photoluminescence," *Journal of Applied Physics,* vol. 115, no. 4, p. 043710, 2014.

[135] M. Tajima, "Determination of boron and phosphorus concentration in silicon by photoluminescence analysis," *Applied Physics Letters,* vol. 32, no. 11, pp. 719-721, 1978.

[136] P. M. Colley and E. C. Lightowlers, "Calibration of the photoluminescence technique for measuring B, P and Al concentrations in Si in the range 10 12 to 10 15 cm -3 using Fourier transform spectroscopy," *Semiconductor Science and Technology,* vol. 2, no. 3, p. 157, 1987.

[137] T. Iwai, M. Tajima, and A. Ogura, "Quantitative analysis of impurities in solar-grade Si by photoluminescence spectroscopy around 20 K," *physica status solidi (c),* vol. 8, no. 3, pp. 792-795, 2011.

[138] A. Liu, H. T. Nguyen, and D. Macdonald, "Quantifying boron and phosphorous dopant concentrations in silicon from photoluminescence spectroscopy at 79 K," *physica status solidi (a),* vol. 213, no. 11, pp. 3029-3032, 2016.

[139] L. Der Sun and J. G. Fossum, "Energy-band distortion in highly doped silicon," *IEEE Transactions on Electron Devices,* vol. 30, no. 6, pp. 626-634, 1983.

[140] K. F. Berggren and B. E. Sernelius, "Band-gap narrowing in heavily doped many-valley semiconductors," *Physical Review B,* vol. 24, no. 4, pp. 1971-1986, 1981.

[141] J. R. Lowney, "Impurity bands and band tailing in moderately doped silicon," *Journal of Applied Physics,* vol. 59, no. 6, pp. 2048-2053, 1986.

[142] K. Morigaki and F. Yonezawa, "Metal-Nonmetal Transition in Doped Semiconductors," *Progress of Theoretical Physics Supplement,* vol. 57, pp. 146-155, 1975.

[143] H. T. Nguyen and D. Macdonald, "On the composition of luminescence spectra from heavily doped p-type silicon under low and high excitation," *Journal of Luminescence,* vol. 181, pp. 223-229, 2017.

[144] N. A. Drozdov, A. A. Patrin, and V. D. Tkachev, "Recombination radiation on dislocations in silicon," *Jetp Lett,* vol. 23, no. 11, 1976.

[145] V. Higgs, E. C. Lightowlers, and S. Tajbakhsh, "Cathodoluminescence imaging and spectroscopy of dislocations in Si and $Si_{1-x}Ge_x$ alloys," *Applied Physics Letters,* vol. 61, no. 9, pp. 1087-1089, 1992.

[146] H. T. Nguyen, F. E. Rougieux, W. Fan, T. Hoe, and D. Macdonald, "Micrometer-Scale Deep-Level Spectral Photoluminescence From Dislocations in Multicrystalline Silicon," *IEEE Journal of Photovoltaics,* vol. 5, no. 3, pp. 799-804, 2015.

[147] R. H. Uebbing, P. Wagner, H. Baumgart, and H. J. Queisser, "Luminescence in slipped and dislocation-free laser-annealed silicon," *Applied Physics Letters,* vol. 37, no. 12, pp. 1078-1079, 1980.

[148] K. Ohmer, W. Ye, Ko, x, J. R. hler, H. P. Strunk, and J. H. Werner, "Defect Formation in Silicon During Laser Doping," *IEEE Journal of Photovoltaics,* vol. 1, no. 2, pp. 183-186, 2011.

[149] M. Ametowobla, G. Bilger, J. R. Köhler, and J. H. Werner, "Laser induced lifetime degradation in p-type crystalline silicon," *Journal of Applied Physics,* vol. 111, no. 11, p. 114515, 2012.

[150] M. Abbott, P. Cousins, F. Chen, and J. Cotter, "Laser-induced defects in crystalline silicon solar cells," in *31st IEEE Photovoltaic Specialists Conference*, Lake Buena Vista, 2005, pp. 1241-1244.

[151] R. A. Street, N. M. Johnson, and J. F. Gibbons, "Defect luminescence in cw laser-annealed silicon," *Journal of Applied Physics,* vol. 50, no. 12, pp. 8201-8203, 1979.

[152] J. M. Moison and M. Bensoussan, "Surface defects induced by pulsed-laser processing of semiconductors and their low-temperature annealing," *Applications of Surface Science,* vol. 20, no. 1, pp. 84-88, 1984.

[153] M. D. Abbott, J. E. Cotter, F. W. Chen, T. Trupke, R. A. Bardos, and K. C. Fisher, "Application of photoluminescence characterization to the development and manufacturing of high-efficiency silicon solar cells," *Journal of Applied Physics,* vol. 100, no. 11, p. 114514, 2006.

[154] X. Yang, D. Macdonald, A. Fell, A. Shalav, L. Xu, D. Walter, T. Ratcliff, E. Franklin, K. Weber, and R. Elliman, "Imaging of the relative saturation current density and sheet resistance of laser doped regions via photoluminescence," *Journal of Applied Physics,* vol. 114, no. 5, p. 053107, 2013.

[155] K. H. Yang, "An Etch for Delineation of Defects in Silicon," *Journal of The Electrochemical Society,* vol. 131, no. 5, pp. 1140-1145, 1984.

[156] L. Xu, K. Weber, A. Fell, X. Yang, E. Franklin, and A. Thomson, "The Influence of Thermal Effects and Dielectric Films on the Electronic Quality of p+ Doped Silicon Processed by Nanosecond Laser," *IEEE Journal of Photovoltaics,* vol. 4, no. 5, pp. 1220-1227, 2014.

[157] G. Masetti, M. Severi, and S. Solmi, "Modeling of carrier mobility against carrier concentration in arsenic-, phosphorus-, and boron-doped silicon," *IEEE Transactions on Electron Devices,* vol. 30, no. 7, pp. 764-769, 1983.

[158] I. Yonenaga, T. Taishi, X. Huang, and K. Hoshikawa, "Dynamic characteristics of dislocations in highly boron-doped silicon," *Journal of Applied Physics,* vol. 89, no. 10, pp. 5788-5790, 2001.

[159] M. Akatsuka and K. Sueoka, "Pinning effect of punched-out dislocations in carbon-, nitrogen- or boron-doped silicon wafers," (in English), *Japanese Journal of Applied Physics,* vol. 40, no. 3A, pp. 1240-1241, 2001.

[160] D. A. Clugston and P. A. Basore, "PC1D version 5: 32-bit solar cell modeling on personal computers," in *26th IEEE Photovoltaic Specialists Conference*, Anaheim, 1997, pp. 207-210.

[161] R. C. Jaeger, *Introduction to microelectronic fabrication* (no. Book, Whole). Upper Saddle River NJ: Prentice Hall, 2002.

[162] H. T. Nguyen, F. E. Rougieux, S. C. Baker-Finch, and D. Macdonald, "Impact of Carrier Profile and Rear-Side Reflection on Photoluminescence Spectra in Planar Crystalline Silicon Wafers at Different Temperatures," *IEEE Journal of Photovoltaics,* vol. 5, no. 1, pp. 77-81, 2015.

[163] R. T. Young, R. F. Wood, W. H. Christie, and G. E. J. Jr., "Substrate heating and emitter dopant effects in laser-annealed solar cells," *Applied Physics Letters,* vol. 39, no. 4, pp. 313-315, 1981.

[164] G. G. Bentini, M. Bianconi, L. Correra, R. Fabbri, R. Nipoti, and S. Nicoletti, "Point Defects Induced In Silicon During Excimer Laser Doping In BCl3 and PCl3 Atmosphere," in *Microelectronic Integrated Processing Conferences*, 1990, vol. 1190, p. 10: SPIE.

[165] M. O. Thompson, J. W. Mayer, A. G. Cullis, H. C. Webber, N. G. Chew, J. M. Poate, and D. C. Jacobson, "Silicon Melt, Regrowth, and Amorphization Velocities During Pulsed Laser Irradiation," *Physical Review Letters,* vol. 50, no. 12, pp. 896-899, 1983.

[166] C.-C. Kuo, "Solidification velocity in liquid silicon during excimer laser crystallization," *Applied Physics A,* vol. 95, no. 2, pp. 573-578, 2009.

[167] L. C. Kimerling and J. L. Benton, "Defects in laser-processed semiconductors," in *Laser and Electron Beam Processing of Materials*, C. W. White and P. S. Peercy, Eds.: Academic Press, 1980, pp. 385-396.

[168] R. F. Wood and G. E. Giles, "Control of melt-front velocity during pulsed laser annealing," *Applied Physics Letters,* vol. 38, no. 6, pp. 422-423, 1981.

[169] R. F. Wood, J. R. Kirkpatrick, and G. E. Giles, "Macroscopic theory of pulsed-laser annealing. II. Dopant diffusion and segregation," *Physical Review B,* vol. 23, no. 10, pp. 5555-5569, 1981.

[170] E. Fogarassy, R. Stuck, M. Toulemonde, D. Salles, and P. Siffert, "A model for laser induced diffusion," *Journal of Applied Physics,* vol. 54, no. 9, pp. 5059-5063, 1983.

[171] L. Wang, M. O. Thompson, and P. Clancy, "Non-Equilibrium Molecular Dynamic Simulation of Laser Thermal Processing of Heavily B-doped Si," in *Rapid Thermal and Other Short-time Processing Technologies II: Proceedings of the International Symposium*, D.-L. Kwong, K. G. Reid, M. C. Ozturk, P. J. Timans, and F. Roozenoom, Eds.: Electrochemical Society, 2001, pp. 345-352.

[172] T. Toshinori, H. Xinming, K. Masayoshi, K. Tomio, F. Tatsuo, and H. Keigo, "Heavily Boron-Doped Silicon Single Crystal Growth: Boron Segregation," *Japanese Journal of Applied Physics,* vol. 38, no. 3A, p. L223, 1999.

[173] H. Azuma, A. Takeuchi, T. Ito, H. Fukushima, T. Motohiro, and M. Yamaguchi, "Pulsed KrF excimer laser annealing of silicon solar cell," *Solar Energy Materials and Solar Cells,* vol. 74, no. 1, pp. 289-294, 2002.

[174] A. H. J. Al-Mousawy, "Effect of laser annealing on defected silicon solar cells," *Journal of Physics: Conference Series,* vol. 241, no. 1, p. 012032, 2010.

[175] Z. Sun and M. C. Gupta, "Laser annealing of silicon surface defects for photovoltaic applications," *Surface Science,* vol. 652, pp. 344-349, 2016.

[176] E. Schneiderlochner, A. Grohe, C. Ballif, S. W. Glunz, R. Preu, and G. Willeke, "Investigations on laser-fired contacts for passivated rear solar cells," in *29th IEEE Photovoltaic Specialists Conference*, New Orleans, 2002, pp. 300-303.

[177] A. S. Raghavan, T. A. Palmer, K. C. Kragh-Buetow, A. C. Domask, E. W. Reutzel, S. E. Mohney, and T. DebRoy, "Employing microsecond pulses to form laser-fired contacts in photovoltaic devices," *Progress in Photovoltaics: Research and Applications,* vol. 23, no. 8, pp. 1025-1036, 2015.

[178] J. I. Pankove and M. L. Tarng, "Amorphous silicon as a passivant for crystalline silicon," *Applied Physics Letters,* vol. 34, no. 2, pp. 156-157, 1979.

[179] S. Dauwe, J. Schmidt, and R. Hezel, "Very low surface recombination velocities on p-and n-type silicon wafers passivated with hydrogenated amorphous silicon films," in *29th IEEE Photovoltaic Specialists Conference*, New Orleans, 2002, vol. 29, no. 1, pp. 1246-1249.

[180] X. Zhang, S. Hargreaves, Y. Wan, and A. Cuevas, "Surface passivation of crystalline silicon by sputter deposited hydrogenated amorphous silicon," *physica status solidi (RRL) – Rapid Research Letters,* vol. 8, no. 3, pp. 231-234, 2013.

[181] X. Zhang, A. Cuevas, B. Demaurex, and S. De Wolf, "Sputtered Hydrogenated Amorphous Silicon for Silicon Heterojunction Solar Cell Fabrication," *Energy Procedia,* vol. 55, pp. 865-872, 2014.

[182] S. De Wolf and G. Beaucarne, "Surface passivation properties of boron-doped plasma-enhanced chemical vapor deposited hydrogenated amorphous silicon films on p-type crystalline Si substrates," *Applied Physics Letters,* vol. 88, no. 2, p. 022104, 2006.

[183] R. A. Sinton and A. Cuevas, "Contactless determination of current–voltage characteristics and minority-carrier lifetimes in semiconductors from quasi-steady-state photoconductance data," *Applied Physics Letters,* vol. 69, no. 17, pp. 2510-2512, 1996.

[184] S. Bowden, U. Das, S. Herasimenka, and R. Birkmire, "Stability of amorphous/crystalline silicon heterojunctions," in *33rd IEEE Photovoltaic Specialists Conference*, San Diego, 2008, pp. 1-4.

[185] J. I. Pankove and D. E. Carlson, "Photoluminescence of hydrogenated amorphous silicon," *Applied Physics Letters,* vol. 31, no. 7, pp. 450-451, 1977.

[186] J. Narayan, C. W. White, M. J. Aziz, B. Stritzker, and A. Walthuis, "Pulsed excimer (KrF) laser melting of amorphous and crystalline silicon layers," *Journal of Applied Physics,* vol. 57, no. 2, pp. 564-567, 1985.

[187] M. Glatthaar, J. Haunschild, R. Zeidler, M. Demant, J. Greulich, B. Michl, W. Warta, S. Rein, and R. Preu, "Evaluating luminescence based voltage images of silicon solar cells," *Journal of Applied Physics,* vol. 108, no. 1, p. 014501, 2010.

[188] M. Taguchi, A. Yano, S. Tohoda, K. Matsuyama, Y. Nakamura, T. Nishiwaki, K. Fujita, and E. Maruyama, "24.7% Record Efficiency HIT Solar Cell on Thin Silicon Wafer," *IEEE Journal of Photovoltaics,* vol. 4, no. 1, pp. 96-99, 2014.

[189] K. Masuko, M. Shigematsu, T. Hashiguchi, D. Fujishima, M. Kai, N. Yoshimura, T. Yamaguchi, Y. Ichihashi, T. Mishima, and N. Matsubara, "Achievement of more than 25% conversion efficiency with crystalline silicon heterojunction solar cell," *IEEE Journal of Photovoltaics,* vol. 4, no. 6, pp. 1433-1435, 2014.